A 2D Modeling Study on the Heat Generation within Carbon Dioxide Electrolysis Systems for Different Geometries

by

B.J.H. ter Borg

to obtain the degree of Master of Science
at the Delft University of Technology,
to be defended publicly on Monday November 29, 2021 at 11:00 AM.

Student number:	4439716	
Project duration:	December 7, 2020 – November 29, 2021	
Thesis committee:	Dr. R. Kortlever,	TU Delft, supervisor
	Dr. ir. J.W.R. Peeters,	TU Delft, supervisor
	Prof. dr. ir. J.T. Padding,	TU Delft, chair
	Dr. ir. J.W. Haverkort,	TU Delft, committee member

TU Delft

Preface

With a glance back in time, I could say that a lot has changed in the last couple of months. At the beginning of my master thesis, I had set up some goals: I wanted to find a subject that I would be very excited about to keep me motivated. Not only did I want to put the knowledge that I had gained so far into practise, I also wanted to learn something new. I really enjoyed working on this project every day, and I am proud to say that I succeeded my goals. The field of electrolysis fascinates me and I am still eager to learn even more, as I am certain that it is a key solution for the future.

Special thanks to Ruud and Jurriaan, who guided me through my thesis. Although most meetings were online, it was a pleasure working with them. They have been very patient and helped me to gain knowledge in the electrochemical and thermal energy field. I can also say that because of their help, I have learned how to do a proper research. Additionally, I would like to thank Johan Padding and Willem Haverkort for taking the time to join my thesis committee.

I also want to thank my family, roommates and friends. They have always been there for me: From making me tea, helping with figures and formula, and having to listen for hours to what I had learned. I am very lucky to have them.

B.J.H. ter Borg
Rotterdam, November 2021

Abstract

An energy transition is needed in order to combat climate change. With the rise of intermittent renewable energy, a need for energy storage is also inevitable. Carbon dioxide electrolysis is a potential solution as CO_2 emissions can be recycled and subsequently converted for energy storage. However, the technology is rather new and research has yet to be conducted in this field. An important aspect is the temperature within an electrochemical cell, especially when scaling up. An increase in temperature can benefit the performance of the cell, but it also has downsides. Hot-spot formation with non-uniform reaction kinetics and thermal sensible components can have a great influence on the life-time of the cell.

For that reason, a modeling study on the heat generation within carbon dioxide electrolysis systems is done. Different volumetric gas flow rates of carbon dioxide have been considered for two geometries: the membrane electrode assembly (MEA) and the gas diffusion electrode (GDE). The model considers three separate models: a mass model, electrochemical model and thermal model, and operates at a fixed current. The finite difference method is applied using Python 3.0 to solve the relevant conservation equations. Furthermore, the model includes different material layers, where the materials and dimensions are based on recently done experiments.

The model showed that irreversible losses caused by the activation overpotentials are the biggest contributor to the total heat generation. Reversible heat also contributes to the heat generation, where heat is required in the anode and heat is generated in the cathode. Furthermore, within the cathodic catalyst layer most heat is generated. Joule heating caused by ohmic losses has proven to have negligibly impact on the total heat generation. As a result, the hot-spot is located within the cathodic catalyst layer for both geometries. Due to the additional electrolyte in the GDE, the hot-spot does not reach the membrane, in contrast to the MEA. Besides, different results in the y-direction are observed for the volumetric flow rates. For both geometries, the hot-spot is located at the inlet for 10 ml min^{-1} and in the middle for 100 ml min^{-1}. From the analysis, the GDE is more favorable as less heat is expected and the hot-spot does not reach the membrane. The sensitivity analysis showed that the thermal conductivity is of great importance.

Nomenclature

Abbreviations

AEM	anion exchange membrane
CL	catalyst layer
CO	carbon monoxide
CO_2	carbon dioxide
CO_2RR	Carbon Dioxide Reduction Reaction
DL	diffusion layer
EL	electrolyte layer
GDE	gas diffusion electrode
MEA	membrane electrode assembly
O_2	oxygen
SOEC	solid oxide electrochemical cell

Physics constants

F	Faraday's constant =96485 [$Cmol^{-1}$]
R	universal gas constant =8.314472 [$JK^{-1}mol^{-1}$]

Dimensionless numbers

Gz	Graetz number
Nu	Nusselt number
Pe	Péclet number
Pr	Prandtl number
Re	Reynolds number
Sh	Sherwood number

Parameters - Greek

α	transfer coefficient
δ	thickness [m]
η	overpotential [V]
μ	dynamic viscosity [Pa]
ρ	density [kgm^{-3}]
σ	conductivity [Sm^{-1}]

ε	porosity of the electrode
φ	local potential [V]

Parameters

$\mathbf{J}_i$	molar flux of species *i* relatively to stationary coordinates [mol $m^{-2}s^{-1}$]
A	area [m^2]
a	activity
a_s	volumetric surface area particle [m^{-1}]
c_i	concentration of species *i* [mol m^{-3}]
C_p	specific heat capacity [$Jkg^{-1}K^{-1}$]
D_i	molecular diffusivity of species *i* [m^2s^{-1}]
E^0	standard equilibrium potential [V]
E_{act}	activation overpotential [V]
E_{diff}	diffusion overpotential [V]
E_{eq}	equilibrium potential [V]
E_{ohm}	ohmic overpotential [V]
E_{th}	thermoneutral voltage [V]
G	gibbs free energy [J mol^{-1}]
H	enthalpy [J mol^{-1}]
h	heat transfer coefficient [$Wm^{-2}K^{-1}$]
j	current density [Am^{-3}]
j^0	current exchange density at electrode [Am^{-3}]
k	thermal conductivity [$Wm^{-1}K^{-1}$]
k_m	mass transfer coefficient [ms^{-1}]
n	number of electrons transferred
p	partial pressure [Pa]
Q	heat dissipation [Wm^{-3}]
R_Ω	ohmic resistance [$kgm^2s^{-3}A^{-2}$]
S	entropy [$Jmol^{-1}K^{-1}$]
S_T	Heat source term [Wm^{-3}]
T	temperature [°C, K]
t	time [s]
V	velocity [ms^{-1}]
z_i	charge number

List of Figures

List of Tables

Contents

1 Introduction

1.1. Necessity for Energy Transition

Climate change is one of the most pressing, if not the most pressing, issues of our time. According to the Intergovernmental Panel on Climate Change (IPCC), the consequences of inaction would be catastrophic. There is currently a broad consensus amongst scientists across the world that human activities, such as industrial processes or farming, are immensely accelerating the change in climate. Consequently, over the 20th century the surface temperature of the Earth has increased by 0.8 °C and is even expected to increase by 1.4-5.8 °C in the 21st century. To put this into perspective: an increase of 4 °C will cause sea levels to rise, cities to submerge, harvest yields to decrease and extreme weathers to occur more often, such as forest fires, storms and droughts [47]. Governments around the world agree that these mentioned effects would be detrimental to the livelihoods of mankind and other lifeforms on this planet. Therefore, they have adopted the United Nations Framework Convention on Climate Change (UNFCCC) at the United Nations Conference on Environment and Development held in 1992, which entered into force in 1994. It was also through this framework that in 2016, the so-called Paris Agreement was ratified by 197 parties, an agreement that is set to ensure that global warming does not exceed the norm of 2 °C. In the Paris Agreement, the energy transition is also mentioned, where the goal is set to have at least a share of 32% of renewables by 2030 [27]. In line with the Paris agreement, a number of measures have to be taken by governments across the world to limit global warming to 2 °C, which include offsetting (counteracting emissions) and direct reduction programs by for example increasing industrial efficiency or changing farm practices. Although there are still a number of issues that would occur with a global temperature increase of less than 2 °C, it is unfortunately deemed impossible to avoid an increase below 1.5 °C at this stage.

To tackle the issue of climate change, it is of vital importance that we reduce the emission of Greenhouse Gases (GHGs). There is a wide variety of GHGs with different levels of impact. It could be argued that CO_2 forms the biggest threat to the climatic conditions: Due to a growing use of fossil fuels, deforestation on a massive scale and the industrialization of agriculture, the amount of CO_2 in the atmosphere has increased and is still increasing significantly over the last few decades. All 188 million tons of carbon dioxide emitted due to fossil fuel burning raises the atmospheric carbon dioxide concentration by 1 ppm by volume [70]. Between 1970 and 2010, 78% of the total GHG emissions came from CO_2 emissions caused by fossil fuel combustion and industrial processes. Furthermore, when looking at the cumulative anthropogenic CO_2 emissions between 1750 and 2011, half of the emissions took place in the last 40 years [20]. It is argued that carbon dioxide is responsible for about three quarters of climatic change [7].

What also needs to be addressed is that an energy transition is not only necessary because of climate considerations, but also because of the fact that these fossil fuels that are now used in large quantities are finite and therefore substitute energy sources must be found. With that said, another problem that arises is the growing world population and industry, causing a greater demand for energy. According to the UN, the world population is expected to grow to 9.7 billion people by 2050, compared to 7.8 nowadays [84]. At the same time, the world energy consumption is expected to grow with 50% [45]. The growth in energy demand, taking into account the reduction of emissions, requires sustainable

solutions. To this end, currently a tremendous effort is put into generating energy in a sustainable way. Examples of ways to generate energy more sustainably are wind turbines, solar energy and the use of biomass. These renewable energy sources ensure that we are less or completely independent on fossil fuels. However, to make this possible, a critical view is needed to look how these renewable energy sources are going to be implemented in the power network.

1.2. Necessity for Energy Storage

Although renewable energy can be considered as a solution, it raises some new problems, such as (1) day-night fluctuations, (2) seasonal fluctuations and (3) network congestion [77]. Nowadays, flexibility in the energy grid can be obtained by existing energy generators that have the ability to scale-up very fast when necessary [77]. Therefore, not only sustainable energy generation is required, but energy storage should also be taken into account. By doing so, a flexible energy grid can be accomplished, where the energy excess can be stored and used when there is an energy deficit. There are different ways to store energy, and more than one solution is needed to get a well-functioning grid. Compared to thermal and mechanical energy storage, electrochemical energy storage obtains the highest energy efficiencies [83]. Electrochemical energy storage matches the desire for flexibility and for large-scale energy storage [83]. An application that is now widely investigated for large-scale energy storage is electrolysis. This application can be used for balancing the grid in hours and week time ranges.

Carbon dioxide electrolysis is a potential solution for energy storage. A reduction reaction of carbon dioxide (CO_2) into a useful product takes place: the Carbon Dioxide Reduction Reaction (CO_2RR). In this way, carbon dioxide can be used as a chemical feedstock or to produce liquid fuels, without using fossil fuels and also reducing the greenhouse gas concentration in the atmosphere [69]. The advantage of this technology is that products can be formed that are already in use nowadays, for instance the electrochemical reduction to form methane. Thus, the existing infrastructure can still be used for energy transportation [75]. Another important aspect to keep in mind is energy density. The energy densities of compressed hydrogen and batteries are significantly less compared to hydrocarbon-derived processes [57]. This can also be seen in Figure 1.1 where advanced fuels are mapped by the UK Department of Transport [9]. Currently, there are still no alternatives that enable a completely substitution of fossil fuels on the large scale, extent and widespread utility that is needed [57]. Together with the increasing GHG emissions caused mainly by carbon dioxide, the need for flexible energy and the need for an energy transition, carbon dioxide capture, and energy storage are seen as a necessary option. With this in mind, a possible, and needed solution is the recycling of carbon dioxide, where the CO_2 emissions are converted back in hydrocarbon fuels that have high-energy densities. However, this technology is rather new, and research has yet to be done in this field. When looking at the temperature and the generated heat within an electrochemical cell, not much research has been devoted to this subject for carbon dioxide electrolysis. The temperature within an electrochemical cell can however have a big influence on the cell's performance. An increase in temperature normally benefits the performance of an electrochemical cell; the activation of the reaction, ionic and electronic diffusion and matter transfer benefit from more thermal input, since temperature has a positive effect on the global cell voltage [76]. However, an increase in temperature can also cause downsides. With temperature dependent components in the electrochemical cell, hot spots can occur and this will have an impact on the overall lifetime of the electrochemical cell. Higher temperatures also cause mass transport limitations due to the lower solubility of CO_2 and depending on the pressure, higher temperatures can lead to lower efficiencies as well.

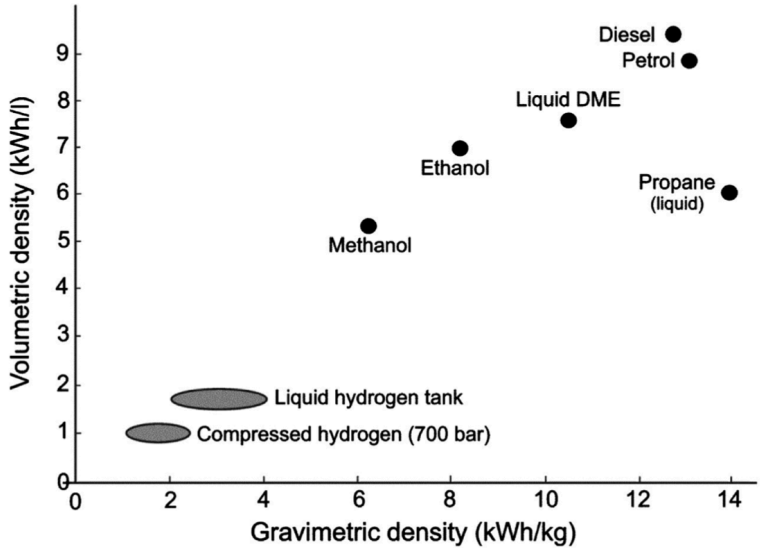

Figure 1.1: Energy densities of current fuels employed in vehicles, Figure 1.1 from France et al. [57]. In the plot, liquid and compressed hydrogen has a low gravimetric density and volumetric density, whereas hydrocarbon-derived processes have high volumetric and gravimetric densities.

1.3. Problem Statement

The electrolysis of carbon dioxide is a very promising solution for recycling carbon dioxide and making the energy transition possible by creating a way to store energy coming from renewables. An optimal carbon dioxide electrolyzer is desired for obtaining high efficiencies, where the heat generation and thus the temperature distribution are of high importance. Changes in temperature will have a significant impact on the electrochemical cell. When the operating temperature increases, the required electrical energy decreases. Also, due to the fact that the kinetics and diffusion coefficients increase exponentially, the internal resistance decreases, and a higher productivity can be achieved with the same voltage [22]. However, the solubility of CO_2 decreases with increasing temperatures and can also lead to a shift in product selectivity [60]. What also needs to be taken into account are local hotspots that may occur within the cell. The performance of temperature sensitive components, like the membrane, can differ with changing temperature. Therefore, it is important to investigate the heat generation and the temperature distribution within a single electrochemical cell, especially when looking at the opportunities to scale up. On that account, obtaining a good understanding of the thermodynamics, kinetics and transport within an electrochemical cell is key.
To get a full idea of these three phenomena, a modeling approach is necessary. For this reason, a literature study has been done to further investigate the research devoted to the modeling of an electrochemical cell.

1.3.1. Knowledge Gap

Carbon dioxide electrolysis is a promising solution that can contribute to the reduction of the GHGs, the needed energy transition and storage. The heat generation in an electrochemical cell is important information for the ability to scale up, where a thermal model can give more insights. The literature found for the modeling of electrochemical cells is mostly focused on hydrogen electrochemical cells and not much modeling research has been devoted to carbon dioxide electrolysis yet. For the modeling of an electrochemical cell, two submodels can be considered: an electrochemical model and a thermal model. Several approaches can be found in the literature for both, with varying levels of complexity. One approach that is often used is to assume a uniform distribution for the current, potential and temperature. Here, the temperature is approximated with the lumped thermal capacity. However, in reality non-uniform heat generation occurs, which can lead to hot spots. Since the components can be thermal sensible, it is desired to know the locations of the heat generation. At the moment, different geometries are considered for the electrolysis of carbon dioxide: the H-cell, membrane electrode assembly (MEA) and the gas diffusion electrode (GDE). When designing an electrolysis stack, knowing for which geometry the heat generation and distribution is most optimal, is valuable information. Also,

knowing which overpotential contributes the most to the heat generation is of great importance.

1.3.2. Research Question

From the knowledge gaps, the following research question with sub questions have been set up:

What is the heat generation within a CO_2 electrolysis system for different geometries?

- What is the local heat generation inside the electrochemical cell and how can it be quantified?
- Which factors contributes the most to heat generation and distribution?
- What is the effect the gas flow rate on the heat generation and distribution?
- What is the effect of electrolyte of the heat distribution in the cell?
- What is the most optimal configuration for CO_2 electrolysis with respect to heat management?

2

Theoretical Background

Closing the carbon cycle, by converting waste carbon dioxide into valuable products, is a possible route to combat climate change. So far, there are multiple ways to obtain valuable products using carbon dioxide. In general, three options can be categorized: (1) water electrolysis together with reverse water gas shift, (2) CO_2-co electrolysis of carbon dioxide and hydrogen and (3) direct conversion of CO_2 by electrolysis [85]. Of these three options, the third option for electrolysis is possible at mild conditions, meaning a temperature below 100°C and a pressure below 10 bar, whereas the first two options are only possible at high temperatures [85]. For carbon dioxide electrolysis, it must be taken into account that carbon dioxide has a very low solubility in water media, and the low solubility would limit the supply and therefore the reaction rate [94].
For the purpose of this thesis, the focus will be on the direct electrolysis of carbon dioxide. To get a good understanding of the electrochemical cell and its electrochemistry, this chapter is devoted to briefly explaining the theoretical background.

2.1. The Electrochemical cell

Electrochemistry concerns the relationship between the electric potential and the chemical change. The transport of charge through a conductor results in a current. Charge can be transported either by the movement of electrons or ions. A general electrochemical cell contains an energy source, an electrolyte and two electrodes: the anode and the cathode. The electrolyte and membrane are ionic conductors and the electrodes are electronic conductors. Thus, electrons move between the electrodes via an electrical wire and ions move between the electrodes via the electrolyte. The electrolyte is often a liquid, but can also be solid such as a membrane. The total reaction is defined by two half reactions. The oxidation reaction takes place on the anode and the reduction reaction on the cathode.

$$\mathrm{aA} + \mathrm{e}^- \longrightarrow \mathrm{bB}(\text{reduction}) \tag{2.1}$$

$$\mathrm{cC} \longrightarrow \mathrm{dD} + \mathrm{e}^-(\text{oxidation}) \tag{2.2}$$

There are two types of electrochemical cells, where a distinction can be made between galvanic cells and electrolytic cells. In a galvanic cell, the reaction occurs spontaneously [8] and the chemical energy is used to obtain electrical energy. The electrolytic cells use electrical energy to store energy by converting it to chemical energy. Since this is a non-spontaneous reaction, an energy source is needed to apply a potential difference between the two electrodes. Both potentiostatic as galvanostatic methods can be applied, keeping the potential fixed or the current fixed during operation, respectively. A schematic representation of the electrochemical cell is presented in Figure 2.1:

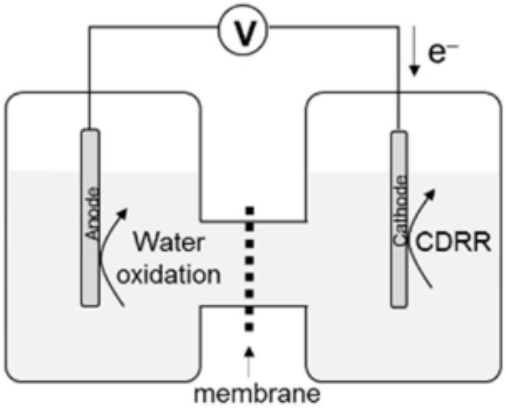

Figure 2.1: A two-compartment electrolyzer containing an anode and a cathode with a proton (or anion) exchange membrane separating the catholyte and anolyte of a similar pH value, Figure 3c from Xie et al. [94].

In this research, the purpose is to convert carbon dioxide into usable fuels, and therefore the focus is on electrolytic cells. According to Kas et al.[46], most studies on CO_2 reduction took place on conventional H-cells. A complete electrolysis stack is made up of different electrochemical cells. The geometry of this can differ per type of electrochemical cell.

2.2. Geometries

As mentioned previously, a various range of products can be achieved with carbon dioxide electrolysis. To obtain the desired product, the choice of geometry of the electrolyzer is very important. Small changes in the reaction environment, such as pressure, temperature, pH level etc., already have a significant impact on the selectivity of the electrochemical cell [19]. For the electrolysis of carbon dioxide, different geometries can be used. According to Chen et al. [19] a distinction of different types can be made based on the required feedstock. Prior research suggests that there are three main types of electrochemical cells that are used for CO_2RR reduction: the H-cell, the membrane electrode assembly (MEA) and the gas diffusion electrode (GDE) (or flow cell). For high temperature electrolysis, the solid oxide electrochemical cell is also a possible configuration. Solid oxide cells will be shortly discussed but will not be taken into account for further research, since the scope of this thesis is on cells that operate at ambient conditions. In the following subchapter, these four types found in the literature are discussed.

2.2.1. H-cell

The H-cell configuration is the simplest electrolyzer configuration that will be considered. This configuration is often chosen for laboratory research, because of the easy operation and low cost [29] of the configuration. The cathode and anode have separate chambers that are connected with each other by an ion exchange membrane. The H-cell is used as a batch reactor and is not suitable to form a cell stack. In many occasions, the H-cell makes use of a reference electrode, thereby operating as a 3-electrode cell. A 3-electrode cell consists out of a working, counter and reference electrode. The reference electrode has a known, stable potential and no current runs through this reference electrode. The use of the reference electrode makes measurements of the potential change at the working electrode possible, which is valuable for studies on half reactions in electrochemical cells. For H-cell electrolyzers, high selectivities can be found in the literature towards some desired products [32]. However, a disadvantage of H-cells is the low and limited upper current densities (<100 mA cm^{-2}), that is caused by the low solubility of CO_2 in the aqueous electrolyte. Another aspect to keep in mind is the large distance between the anode and the cathode, that causes a high ohmic resistance within the electrochemical cell [32]. The third disadvantage is the limited electrode surface area [29].

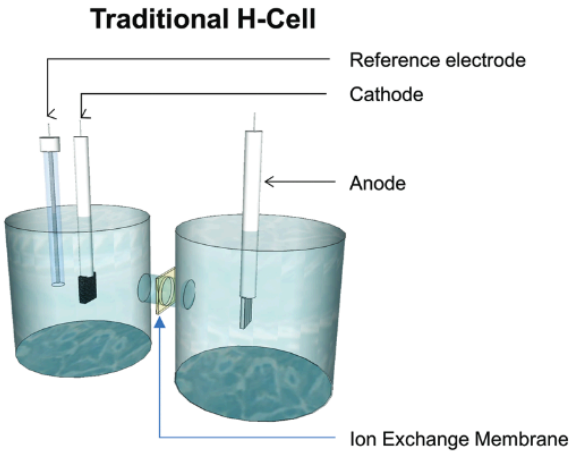

Figure 2.2: A traditional H-cell, Figure 9 from Kibria et al. [49]. The configuration contains three electrodes: the anode, the cathode and a reference electrode. An ion exchange membrane is placed between the two chambers, connecting the anode and the cathode.

2.2.2. Gas Diffusion Electrode

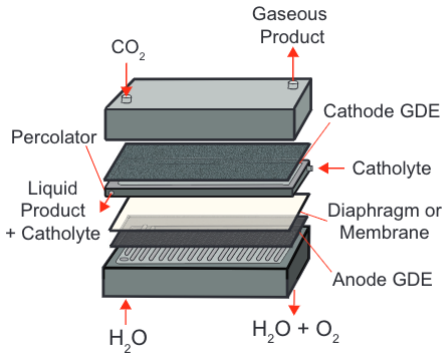

Figure 2.3: Flow cell configuration, Figure 5 from Chen et al. [19]. The flow cell is a three flow channel, and contains two gas diffusion electrodes. The membrane separates the anolyte and the catholyte, ensuring that only charge carrier ions are transferred to the other electrode.

Another typical used configuration is the gas diffusion electrode flow cell electrolyzer. The flow cell electrolyzer has three flow channels: one for the inlet containing carbon dioxide, one for the catholyte, in which the carbon dioxide dissolves and one for the anolyte. The compartment with gaseous carbon dioxide and compartment with liquid catholyte is separated by a gas diffusion electrode. The catalyst is placed on the side where the electrode touches the liquid catholyte. The catholyte and the anolyte are separated by an ion exchange membrane, ensuring that only charge carrier ions are transferred to the other electrode and carbon-products exit the carbon dioxide channel. Since carbon-products cannot contact the other electrode, they cannot be oxidized back into carbon dioxide. The membrane also ensures that the formed O_2 cannot travel back to the cathode. The choice of another ion exchange membrane is optional, such as a cation-exchange membrane (CEM), anion-exchange membrane (AEM) or a bipolar membrane (BPM). This choice depends on which product is desired and the pH level of electrolyte that is used in the electrolyzer. Another option is to use no membrane, to avoid ohmic losses. However, using no membrane is not possible when using a recirculating electrolyte. For research purposes, adding a reference electrode is also possible [32], creating the before mentioned 3-electrode cell. Overall, flow cell electrolyzers can be used for the formation of CO, formate and multicarbon hydrocarbons/oxygenates, since it can achieve high current densities (>1 Acm^{-2}). Downsides of the flow cell electrolyzer is that the flow cell electrolyzer has an impurity deposition on the catalysts side and penetration of liquid into the gas diffusion electrode and flooding [49]. The flow cell electrolyzer also

has an increasing ohmic overpotential due to bubble formation.

2.2.3. Membrane Electrode Assembly

The membrane electrode assembly only has two flow channels, where one is for the inlet of carbon dioxide and the other one is for the anolyte. Different from a flow cell electrolyzer, the anode and cathode are separated by an ion-exchange membrane, where the membrane acts as the electrolyte. This results into a zero-gap configuration, where the electrode, catalyst and membrane are pressed together. A distinction can be made depending on the membrane used: CEM, AEM and BPM. The charge carriers are H^+, OH^- and H^+ together with OH^- respectively. Another difference is that the gaseous carbon dioxide at the inlet has to be humidified or a liquid anolyte has to be used to keep the membrane hydrated. Compared to GDE flow cell electrolyzers, MEA electrolyzers have lower ohmic losses and can be easily pressurized. With the absence of a catholyte, the problem of flooding is also removed, together with electrolyte impurity and the generation of carbonate salts. On the other side, liquid products are still able to clog the gas diffusion electrodes. For MEA electrolyzers, catalysts that tend to have poor CO_2RR selectivity when used in flow cell electrolyzers, can be used to obtain products that are usually not produced, such as: methanol, isopropanol and C5 long chain products[49]. Although MEA electrolyzers seem to be promising, the desired energy density is yet not been achieved [19]

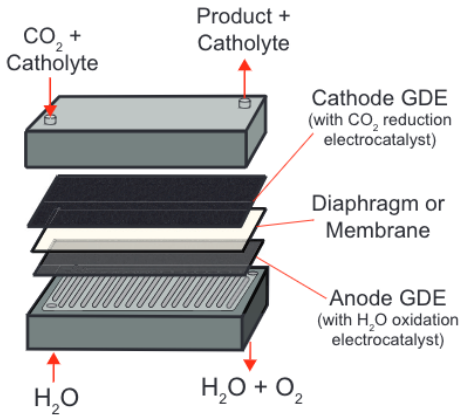

Figure 2.4: MEA configuration, Figure 5 from Chen et al. [19]. The MEA only has two flow channels, where the membrane also functions as the electrolyte. This results into a zero-gap configuration and lowers the ohmic losses.

2.2.4. Solid Oxide Electrolyzers

The solid oxide electrolyzer differs from the two electrolyzers discussed above, since this configuration has a solid cathode, anode and electrolyte. Solid oxide electrolyzers are commonly used for co-electrolysis, where products such as carbon monoxide and methane are made with high current densities from carbon dioxide and hydrogen/water. Solid oxide electrolyzers operate at very high temperatures, above 600°C. This results in lower ohmic resistances in the electrochemical cell [96]. Due to these high temperatures, the SOEC is more difficult to implement in the industry where waste heat is not necessarily available [19].

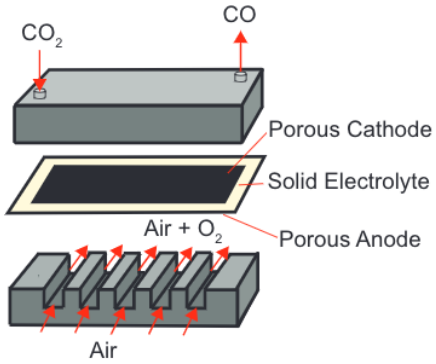

Figure 2.5: SOEC configuration, Figure 5 from Chen et al. [19]. The SOEC configuration has a solid cathode, anode and electrolyte and operates at high temperatures.

2.3. Reduction of Carbon Dioxide

Upon capturing CO_2 from the atmosphere, it can be electrochemically converted into useful fuels or chemicals. A study by Kuhl et al. [52] concluded that the Carbon Dioxide Reduction Reaction (CO_2RR) can produce up to 16 different gas and liquid products, where the product outcome is highly dependent on the selectivity of the used catalyst.

2.3.1. Electrocatalyst

When a catalyst takes part in the electrochemical reaction at the surface of the electrodes or functions as an electrode itself, the catalyst is referred as an electrocatalyst [51]. The electrocatalyst can stimulate the transfer of electrons between electrode and reactants and the electrocatalyst can also facilitate an intermediate chemical transformation [30]. For the choice of catalyst, the catalytic activity and the stability are of great importance. The activity of the catalyst determines to what extent the catalyst contributes to the reaction speed and the stability determines how fast the activity will start to decrease. A catalyst can change the reaction kinetics and therefore, a change in electrocatalyst can result in different product outcomes. Two-electron-transfer products such as carbon monoxide, formate and formic acid are formed with the use of respectively Ag- and Au-based catalysts or Sn-based catalysts with high selectivities. On the other hand, the multiple-electron-transfer products such as methanol, methane, ethanol, ethylene and propanol are only obtained with Cu catalysts with lower selectivities [49]. In Figure 4.8, some products and their half reactions are shown.

Table 1. Electrode potential of common products in aqueous CDRR.

Product	Transferred electron no.	Half reaction	$E^{[a]}$ [V vs. SHE]
$CO_2^{\cdot-}$	1	$CO_2 + e^- \rightarrow CO_2^{\cdot-}$	- 1.90
H_2	2	$2H^+ + 2e^- \rightarrow H_2$	0
CO	2	$CO_2 + 2H^+ + 2e^- \rightarrow CO + H_2O$	- 0.11
HCOOH	2	$CO_2 + 2H^+ + 2e^- \rightarrow HCOOH$	0.02
HCHO	4	$CO_2 + 4H^+ + 4e^- \rightarrow HCHO + H_2O$	- 0.07
C	4	$CO_2 + 4H^+ + 4e^- \rightarrow C + 2H_2O$	0.21
CH_3OH	6	$CO_2 + 6H^+ + 6e^- \rightarrow CH_3OH + H_2O$	0.03
CH_4	8	$CO_2 + 8H^+ + 8e^- \rightarrow CH_4 + 2H_2O$	0.17
C_2H_4	12	$2CO_2 + 12H^+ + 12e^- \rightarrow C_2H_4 + 4H_2O$	0.06
C_2H_5OH	12	$2CO_2 + 12H^+ + 12e^- \rightarrow C_2H_5OH + 3H_2O$	0.08

[a] Potentials at standard conditions with pH = 0 and 25 °C.

Figure 2.6: The half reactions and the corresponding electrode potentials of common products in aqueous Carbon Dioxide Reduction Reaction (CDRR) are shown, Table 1 from Xie et al. [94]. The electrode potential is characterized with a reference electrode of a standard hydrogen electrode (SHE).

2.3.2. Influence of the Industry on Product Choice

In the industry, the choice of product is dependent on the market size and price. This means that a high product demand is important for the choice of product. Simultaneously, the price also needs to be compatible with existing ways to obtain the same product. From the analysis done by Kibria et al. [49], the products carbon monoxide, formate and propanol are promising together with ethanol and ethylene, that have high energy values and large market sizes. Another thing that is important are the capital and investment costs. The feasibility of the products is determined by the electricity costs. Compared to hydrogen, carbon dioxide is already more expensive to produce, since more energy is needed to start the reaction. In its own range of products, products with more C-H and C-C bonds are more sensitive to electricity prices [49]. A general way to express the reaction of carbon dioxide into a product, can be seen in equation:

$$\mathrm{mCO_2 + n(H^+ + e\text{-}) \longrightarrow product + xH_2O} \tag{2.3}$$

The formation of carbon monoxide is seen as a valuable product, since carbon monoxide can be used as an intermediate for the formation of multicarbon hydrocarbons and oxygenates [49]. Currently, much research is devoted to catalyst development, since improved catalysts can reduce the needed activation overpotential. Using other catalysts can also alter product selectivities [49]. The full reaction of the formation of carbon monoxide is shown below:

$$\mathrm{CO_2 \longrightarrow CO + \frac{1}{2}O_2} \tag{2.4}$$

2.3.3. Temperature Dependence

Temperature has a significant influence on the electrochemical performance. As stated, to know how much heat is generated and how this heat is distributed within the electrochemical cell is very important. This subchapter is devoted to emphasizing the significant influence of temperature, substantiated by experiments found in the literature. This subchapter also includes literature based on water electrolysis in a PEM electrolyzer. Although water electrolysis differs from carbon dioxide electrolysis, the knowledge of the effect of temperature in these systems can be considered as relevant for carbon dioxide electrolysis as well.

An experiment was done by Löwe et al. [60] to find an effect of the temperature on the cathode activity, product distribution and mass transport. The experiment was performed under ambient pressure and varying temperature between 20 °C and 70 °C, where CO_2 was reduced to formate in a gas diffusion electrode electrolyzer. The focus was on a maximum current density and energy efficiency. According to this experiment, an increase in temperature results in an increase in current density. Also, with increasing temperature, the reaction kinetics and diffusion coefficients are improved exponentially. This lowers the activation and diffusion overpotential, that will be discussed later in this report. However, higher temperatures in the electrochemical cell will result in a mass transport limitation, since the CO_2 solubility is lowered. For the product distribution, a previous study showed that for a current density of 200 $mAcm^{-2}$, temperature has no strong influence on hydrogen evolution [60]. Another aspect to keep in mind is the overall efficiency. A literature study on temperature optimization for PEM water-electrolysis [79] found that the overall efficiency does not increase necessarily when the temperature increases. This is dependent on the pressure of the system. This study also suggests that when the gas permeability decreases to lower temperatures, the Faradaic efficiency increases. This can be beneficial when the safety of the system is taken into account. Since hydrogen is a highly explosive gas, this factor plays a bigger role than for carbon dioxide electrolysis, because carbon dioxide is an inert gas.

Another important aspect is the heat distribution within an electrolyzer. The literature study of Olesen et al. [71] made a 3D model that examines the charge, mass and heat distribution in a PEM electrolysis cell. This study underpins the claim that heat generation causes a non-uniform heat distribution in an electrochemical cell, which can also be found in other literature studies [21]. This phenomenon will lead to hot spots within the electrochemical cell. The hot spots occurred underneath the outlet channels and at these regions, higher current densities can be observed [71]. Not only because of the non-uniform distribution of current density, the generation of heat is important to take the into consideration. According to Bauer et al. (2005) [10], there is a risk of a thermal and mechanical degradation of the membrane when the temperature becomes too high. In addition, as stated by Nandjou et al. (2015) [65], the increased permeation of hydrogen can also affect the membrane due to hot spot formation. Since other components in the electrochemical cell can also be sensitive to elevated temperatures, hot-spot formation will play a significant role for the durability of the electrolyzer. Moreover, in an electrolyzer stack, the rise in temperature can have a greater effect.

In the following subchapters, the thermodynamics, kinetics and transport within an electrochemical cell with the relevant conservation equations are discussed.

2.4. Thermodynamics

At standard conditions, T = 298 K and p = 1 atm, carbon dioxide is a gas. The transition from solid to a gas already occurs at -78 °C. Different from hydrogen, carbon dioxide is considered as an inert gas that is not explosive or flammable. Green plants use carbon dioxide to convert water into oxygen and glucose, a useful fuel. The reduction of carbon dioxide, and thus the reduction of GHGs, into the desired product is an endothermic reaction, which means that energy has to be put in for the reaction to start. To determine how much energy is needed for endothermic reactions, one has to look at the thermodynamics behind the reaction [70].

For the thermodynamics, the difference between the enthalpy and Gibbs free energy of reaction is important to emphasize. The enthalpy is defined as the internal energy. Gibbs free energy of reaction is defined as the minimum amount of work the reaction can produce or is required to produce a product and can be derived from any system under constant temperature and pressure. A positive Gibbs free energy indicates an endothermic reaction, and a negative Gibbs free energy indicates an exothermic reaction. Every chemical has its own standard heat of formation ($\Delta {H_f}^0$) and standard free energy of formation ($\Delta {G_f}^0$). These values are defined for a standard pressure and temperature of 1 atm and 298 K, respectively. Gibbs free energy of reaction is determined by the individual free energy of formations of the chemicals in the reaction. The summation of the Gibbs free energy of formation of the products minus the summation of the Gibbs free energy of formation of the reactants gives the Gibbs free energy of reaction [70]:

$$\Delta G_r = \Delta G_{f,prod} - \Delta G_{f,reac}. \tag{2.5}$$

Likewise, the enthalpy of reaction can be determined [70]:

$$\Delta H_r = \Delta H_{f,prod} - \Delta H_{f,reac}. \tag{2.6}$$

The Gibbs free energy of reaction can also be determined by [70]:

$$\Delta G_r = \Delta H_r - T\Delta S_r, \tag{2.7}$$

where G (J), H (J), S (JK^{-1}), T (K) are Gibbs free energy, enthalpy, entropy and temperature, respectively. For electrolysis mostly endothermic reactions are considered, meaning that an external energy input is necessary to drive the reaction. The equilibrium potential indicates the minimum potential difference that is needed to drive this specific reaction. First, the equilibrium potential is taken into account at standard reference conditions, also known as the reversible potential, E^0. Since the position of equilibrium is determined by the Gibbs free energy of reaction, the standard equilibrium potential E^0 is given by [78]:

$$E^0 = -\frac{\Delta G_r}{nF}, \tag{2.8}$$

where E^0 [V], n and F [A mol^{-1}] represent the equilibrium potential at standard conditions, the number of electrons transferred and Faraday's constant, respectively. When no standard conditions are assumed, another term needs to be added to compensate for this. This is done with the Nernst equation:

$$E_{\text{eq}} = E^0 + \frac{RT}{nF}\ln\left(\frac{a_{Ox}}{a_{Red}}\right), \tag{2.9}$$

where E_{eq} [V], R [$JK^{-1}mol^{-1}$] and a are the equilibrium potential, the universal gas constant and the activity, respectively. Besides the equilibrium potential, there is the thermoneutral potential E_{th} that corresponds to the heat of reaction. When the electrochemical cell operates at thermoneutral potential, no heat is lost or required by the cell. Thus, the thermal efficiency is equal to 100%. The thermoneutral E_{th} is given by:

$$E_{\text{th}} = -\frac{\Delta H_r}{nF}. \tag{2.10}$$

When more potential is added to a reaction, heat will be generated. This is caused by the overpotentials, that will be discussed further in this thesis.

2.5. Kinetics

When looking at the thermodynamics, a cell equilibrium is taken into account with no current flowing in the system. The kinetics are important when a reaction is observed with a current flowing in the electrochemical cell. The next subchapter will describe electrochemical kinetics and in particular the Butler-Volmer equation.

2.5.1. Arrhenius Equation

The rate constant k [ms^{-1}] is described by the Arrhenius equation [8]:

$$k = Ae^{-E_{\text{A}}/RT} \tag{2.11}$$

Here, E_A represents the activation energy and A represents a pre-exponential factor. The higher the temperature, the higher the reaction rate and consequently results in a faster reaction. It can be stated that the influence of the temperature has significant influence during electrochemical reactions.

2.5.2. Butler Volmer

From the Arrhenius equation, the Butler-Volmer equation can be derived when assuming that the activation energy is driven by the potential. The Butler-Volmer equation represents the relation between the current density j and the applied potential η, where η= (E_{cell}-E_{eq}). The Butler-Volmer equation is stated as follows, Equation 2.12:

$$j = j^0 \left[\exp\left(\frac{\alpha F \eta}{RT}\right) - \exp\left(\frac{-(1-\alpha)F\eta}{RT}\right) \right], \tag{2.12}$$

where j [Am^{-2}], j^0 [Am^{-2}] and α are the current density, the exchange current density and the transfer coefficient, respectively. R represents the gas constant and η [V] the overpotential. The two exponential terms in the Butler-Volmer equation are equal to the anodic and cathodic term, respectively. With the exchange current density, j^0, the rate per area of the reactions is determined at equilibrium. The higher the exchange-current density, the faster the reaction rate. The exchange current density is temperature and concentration dependent. The parameters in the Butler-Volmer equation are based on empirical data.

2.5.3. Tafel approximation

When the applied potential becomes very positive, the cathodic term can be neglected. For that reason, the Butler-Volmer equation far from equilibrium can be approximated by the Tafel equation, Equation 2.13 .

$$j \approx j^0 \exp\left(\frac{\alpha F}{RT}\eta\right) \tag{2.13}$$

Vice versa, the same holds for potentials that have a very large negative value, which means the anodic term can be neglected. Like mentioned, the exchange current density is not only temperature dependent, but also concentration dependent. Since a reaction takes place at the electrode, carbon dioxide can be consumed or generated, which will cause a concentration difference from the bulk.
The reason for the different approaches, is that the mass diffusion term is not always considered. The inclusion of the mass diffusion term is dependent on the current distribution. When considering the secondary current distribution, only the kinetics and the thermodynamics are important. This means that the mass transport model can be neglected and thus the mass diffusion term. However, when a tertiary current distribution is considered, the mass diffusion term and thus a mass transfer model is important. At this point, the overpotential needed to compensate for the mass transfer resistance has to be taken into account. More details will be discussed later in section 2.7. Increasing the surface area of an electrode, will also increase the reaction rate. Since the internal surface of a porous electrode is much higher than the external surface, the volumetric current density is often used, to incorporate the internal surface [40]:

$$J = \pm j^0 a \left(\frac{C_i}{C_{i,ref}}\right)\left[\exp\left(\frac{\alpha F}{RT}\eta\right) - \exp\left(\frac{-(1-\alpha)\mathrm{F}}{RT}\eta\right)\right]. \tag{2.14}$$

Here, a represents the volumetric surface area [m^{-1}], which can be defined by the porosity ε and the surface area of a single electrode particle a_s [40]:

$$a = (1-\varepsilon)a_s. \tag{2.15}$$

2.6. Transport

Besides thermodynamics and the kinetics, transport within the electrochemical cell is an important phenomenon. The transport within an electrochemical cell is already briefly discussed in the previous subchapter, where the mass transfer due to diffusion becomes more important with increasing current density. With transport, not only diffusion but also convection and migration have to be considered. In the next subchapter, the conservation of species, charge and energy is discussed with their governing equations.

2.6.1. Conservation of species

For the conservation of species, the Nernst-Planck equation is most commonly used. The Nernst-Planck equation considers all three transport modes: migration, diffusion and convection [31]:

$$\vec{S}_{c,i} = \underbrace{-z_i u_i F c_i \nabla\phi}_{\text{migration}} + \underbrace{D_i \nabla c_i}_{\text{diffusion}} + \underbrace{c_i \vec{V}}_{\text{convection}}. \tag{2.16}$$

Here, $\vec{S}_{c,i}$ [mol $m^{-2}s^{-1}$], z [-], u [m^2mol J^{-1} s^{-1}], $\nabla\varphi$ [V], D [m^2s^{-1}], c [mol m^{-3}], $\vec{v}$ [ms^{-1}] are the molar flux, charge number, the mobility of ion, the potential, the molecular diffusivity, concentration and the velocity, respectively. The subscript i represents the species. It resembles Fick's law, that considers diffusion due to a concentration gradient. The convection contributes for the molar velocity of the bulk flow. The migration term arises from the gradient in electrical potential.

2.6.2. Conservation of charge

With the volumetric current density, the electric and protonic potentials can be obtained. To do so, the conservation of transport for both electrons and protons must be solved. The source terms S_e and S_m are zero everywhere, except for the catalyst layer, as can be seen in Table 4.4.

$$\frac{\partial}{\partial x}\left[-\sigma_e^{eff}\frac{\partial \varphi_e}{\partial x}\right] = S_e, \tag{2.17}$$

$$\frac{\partial}{\partial x}\left[-\sigma_m^{eff}\frac{\partial \varphi_m}{\partial x}\right] = S_m, \tag{2.18}$$

where σ_m and σ_e are the ionic and electric conductivity.

2.6.3. Conservation of energy

During operation, heat is generated and consumed by the reaction. For the heat transfer model, the energy balance is important. Therefore, the energy conservation equation is considered, Equation 4.3 [90]:

$$\rho c_p\left(\frac{\partial T}{\partial t} + \vec{V}\cdot\nabla T\right) = \nabla\cdot(k\nabla T) + S_T, \tag{2.19}$$

where ρ [kgm^{-3}] is the mass density,c$_p$ [J kg^{-1}K^{-1}] the specific heat and k [Wm^{-1}K^{-1}] is the thermal conductivity. S_T[(Wm^{-3}] represents the source term. For steady state analysis, the first term is zero. Also, when no flow is present, the convective heat transfer is negligible as well.

The heat generation is indicated by the source term, and in general the following heating generations occur within an electrochemical cell [35, 90]:

- **Joule or ohmic heating**: Ohmic losses occur in the entire electrochemical cell, where a distinction can be made for electric and ionic joule losses.
- **Irreversible heating due to activation and diffusion losses**: The irreversible heating is caused by the activation overpotential and diffusion overpotential. The activation losses are important at the catalyst layers of the electrochemical cell. Likewise, heating due to the diffusion losses occurs also at the catalyst layer.
- **Reaction or reversible heating**: Within the cathode and the anode, the source term also includes the entropy changes in the reaction [90, 97], called reversible heating. The reversible heating is determined by the difference between the thermoneutral and equilibrium potential. When the thermoneutral potential is larger than the equilibrium potential, heat is required from the system. When the opposite is true, heat is generated.
- **Heating due to phase change**: The source term for the phase change, S_{reac}, can be determined by the reaction rate between the different phases. This will not be taken into account in this research.

The total source term can be determined by the sum of the separate source terms and is dependent on the relevant heat transfer that occurs and can differ for every part within the electrochemical cell.

2.7. Overpotentials

According to the thermodynamics, a certain amount of energy is needed for the reaction. However, in practise, the theoretically required potential is shown to be not sufficient for electrolytic electrochemical cells. This shortage has to do with the efficiency of the electrochemical cell. For electrolytic cells, more energy is needed to drive the reaction and not all input energy can be recovered. In this case, the extra potential, deamed the overpotential, will generate heat. The total overpotential is caused by energy

losses, where the losses can be observed individually. In Figure 2.7, the polarization curve of a fuel cell is shown, and an indication is given which part of the polarization curve is characeterized by which overpotential. The polarization curve of an electrolytic cell is different, since the losses needs to be added to the cell potential instead of subtracted.

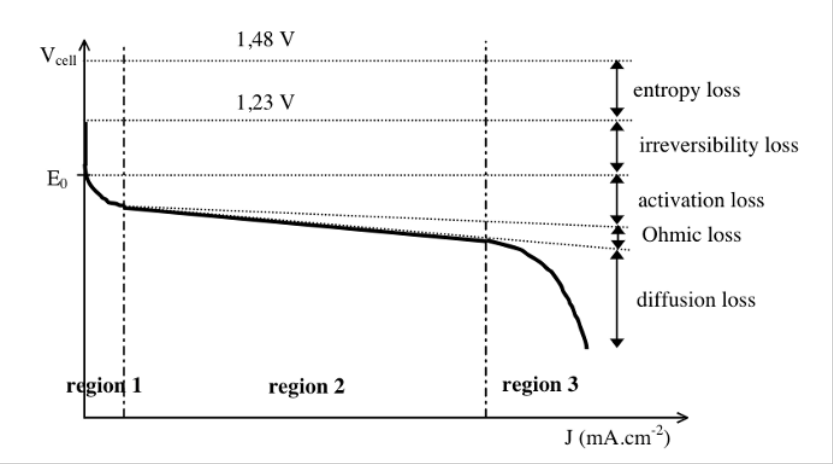

Figure 2.7: Fuel cell characteristic, where the cell voltage is plotted against the current density, Figure 1 from Busquet et al. [16]. The plot shows the potential losses that occur within a cell: entropy, irreversible, activation, ohmic and diffusion losses.

Here, the total cell potential is determined by the equilibrium potential, according to the thermodynamics, plus the activation, ohmic and diffusion losses, Equation 2.20.

$$E_{\text{cell}} = E_{\text{eq}} + E_{\text{act}} + E_{\text{ohm}} + E_{\text{diff}}, \tag{2.20}$$

where the subscripts eq, act, ohm and diff are reversible, activation, ohmic and diffusion, respectively.

Which overpotential needs to be taken into account for obtaining a proper model for the heat generation, is dependent on the made assumptions. In general, three approaches can be categorized [31]:

- Primary current distribution: Kinetics and mass transfer are neglected. The distribution is only dependent on the **ohmic overpotential**.
- Secondary current distribution: Kinetics are included and are assumed to be rapid. The distribution is dependent on the **ohmic overpotential** and **activation overpotential**.
- Tertiary current distribution: Mass transfer and kinetics are both included. The distribution is dependent on all three discussed overpotentials: the **ohmic, activation and diffusion overpotential**.

In the following subchapters, the ohmic, activation and diffusion overpotential are discussed in further detail.

2.7.1. Ohmic Overpotential

The ohmic overpotential is determined by resistances caused by the non-infinite conductivity of the electrochemical cell. Resistances can occur at every location in the electrochemical cell: the electrolyte, electrodes, membrane etc. In the electrolyte ions are transported and in the electrodes mainly electrons. Within the catalyst later, both electric as ionic ohmic losses occur. The ohmic overpotential is given by Ohm's law, where the ionic ohmic losses differ from the electronic ohmic losses:

$$E_{\text{ohm, ion}} = \frac{jL}{\sigma_m}, \tag{2.21}$$

$$E_{\text{ohm, ele}} = \frac{jL}{\sigma_e}, \tag{2.22}$$

where L [m] is the length of the considered part of the cell and σ is the conductivity [S m^{-1}]. Here, σ is the conductivity of the considered component within the electrochemical cell. The resistance value and the conductivity are often given by empirical relations [55].
There has been numerous studies that included the ohmic overpotential, but with varying extent. The study of Lebbal et al. [55] stated that for a PEM electrolyzer the main ohmic loss is caused by the polymer membrane. Another study of Cumming et al. [22] stated that the overpotential, and thus heat generation, in a SOEC is mainly caused due to the resistance of the electrolyte. However, according to the study of Han et al. [39] , all components are included for the ohmic resistance within an electrochemical cell. In summary, a literature review of Olivier et al. [72] provided an overview, where three predominantly ways are found to address the ohmic losses within an electrolyzer: (1) consider the ohmic voltage due to the electrolyte, (2) consider the ohmic voltage due to electrolyte and other materials conductivities and (3) consider only the equivalent resistance for the cell represented by a fitted parameter.

2.7.2. Activation overpotential

The electrodes of the electrochemical cell are in contact with the electrolyte, in which ions can move freely. The electrode has a charge on the outside, and as a result the ions are attracted, and a layer of opposite charge is formed around the electrode: the so-called double layer. In addition, a diffusion layer is formed by the non-uniform charge when a reactions occurs, where the electric field is very strong. A potential drop can be observed between the potential of the electrode and the potential just outside the diffusion layer. The half-reactions of the electrochemical cell take place at the surface of the electrodes. The rate of reaction is set by the changing potential of the electrodes, that also influences the potential drop across the double layer. The changing potential of the electrodes can also control the direction of the reaction [31]. To enable a reaction to take place, an energy barrier must be overcome: the activation overpotential. A lower Gibbs free energy of reaction means a lower needed activation overpotential. The activation overpotential is equal to the difference between the voltage drop across the double layer with the applied voltage and in equilibrium.
The activation overpotential is a loss that needs to be added to activate the reaction. To describe it in more detail: the reactant and product molecules have different arrangements of atoms, which also correspond to different potential energy minima. Between those two minima, a maximum energy potential can be found which has to be overcome to activate the reaction [37]. This can be done by adding a certain amount of energy: the activation overpotential.

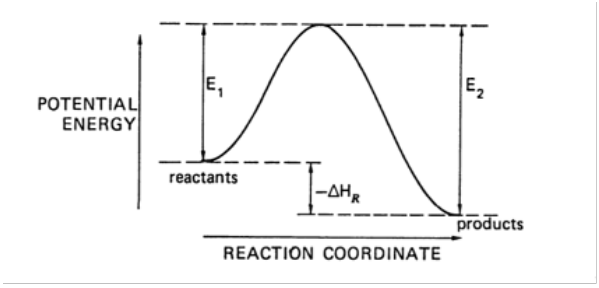

Figure 2.8: Plot of potential energy along the reaction coordinate, Figure 3.1 from Goodridge et al. [37]. The plot shows the amount of potential energy that is needed to activate the reaction (E_1).

This overpotential is highly dependent on physical and chemical parameters, like operating temperature, the type of catalyst used, active reaction site and electrode morphology [39]. The activation overpotential can be calculated using the Butler-Volmer equation. The Butler-Volmer equation is an approximation of the real current-density overpotential relation for a reversible process.

2.7.3. Diffusion Overpotential

The diffusion overpotential is an overpotential that is caused due to the mass transport limitations inside the electrodes of an electrolyzer [39, 91]. The reactants and products need to be transported and removed from the electrolyte, respectively. Because of the slowness in mass transport within the electrochemical cell, a resistance occurs for the reactants and products to be transported to and removed from the reaction sites, respectively. This results into a concentration gradient between the bulk electrolyte and the surface of the electrodes. This especially happens at high current densities,

when the reaction is no longer controlled by electronic transport but by mass transport [72]. Following Newman and Thomas, the diffusion overpotential can be approximated with [31]:

$$\begin{aligned} E_{\text{diff}} =& i \int_0^{\infty} \left(\frac{1}{\sigma} - \frac{1}{\sigma_{ref}} \right) dx + \frac{RT}{nF} \ln \left(\frac{c_{i,ref}}{c_{i,0}} \right) \\ &+ F \int_0^{ref} \sum_i \frac{z_i D_i}{\sigma} \left(\frac{c_{i,ref} - c_i}{\delta} \right) dx, \end{aligned} \tag{2.23}$$

where σ [Sm^{-1}] is the electrical conductivity and δ [m] the thickness. This diffusion overpotential has to be taken into account for both the anode and cathode electrode. The diffusion overpotential is divided into three parts: the error for using the bulk concentration for the ohmic losses, the equilibrium potential difference and the diffusion potential. When assuming an excess supporting electrolyte and assuming that the third term is relatively small, Equation 4.57 can be used:

$$E_{\text{diff}} \approx \frac{RT}{nF} \ln \left(\frac{c_{i,ref}}{c_i} \right). \tag{2.24}$$

In the literature, it is also mentioned as the concentration overpotential [24, 91]. The diffusion overpotential is not always considered when modeling the electrochemical cell. However, the diffusion overpotential does play a significant role for the modelling of the electrochemical cell when current densities are high [3, 33]. The way the diffusion overpotential is implemented in the model is also not consistent, which is in line with Olivier et al. [72], that also states that in literature different descriptions can be found. Often, the diffusion overpotential is taken into account with only the second term, Equation 4.57.

The diffusion and activation overpotential both influence the overpotential. When the kinetics are slow, the current is limited by the kinetics. Likewise, when the mass transfer is slow, the current is limited by the mass transfer. The applied overpotentials affects the influence of both the kinetics as the transport in the electrochemical cell: higher overpotentials result in higher current densities and faster reaction rates and is therefore only dependent on mass transfer.

2.8. Electrolysis Modeling

The literature study on electrochemical modeling demonstrates that two submodels can be considered: an electrochemical model and a thermal model. Several approaches can be found in the literature for both, with varying levels of complexity. In Table A.3 all literature studies that are examined are showed. These literature studies are used to substantiate the choices made in this modeling research. Furthermore, in Figure 2.9 a summary for electrolysis modeling is shown.

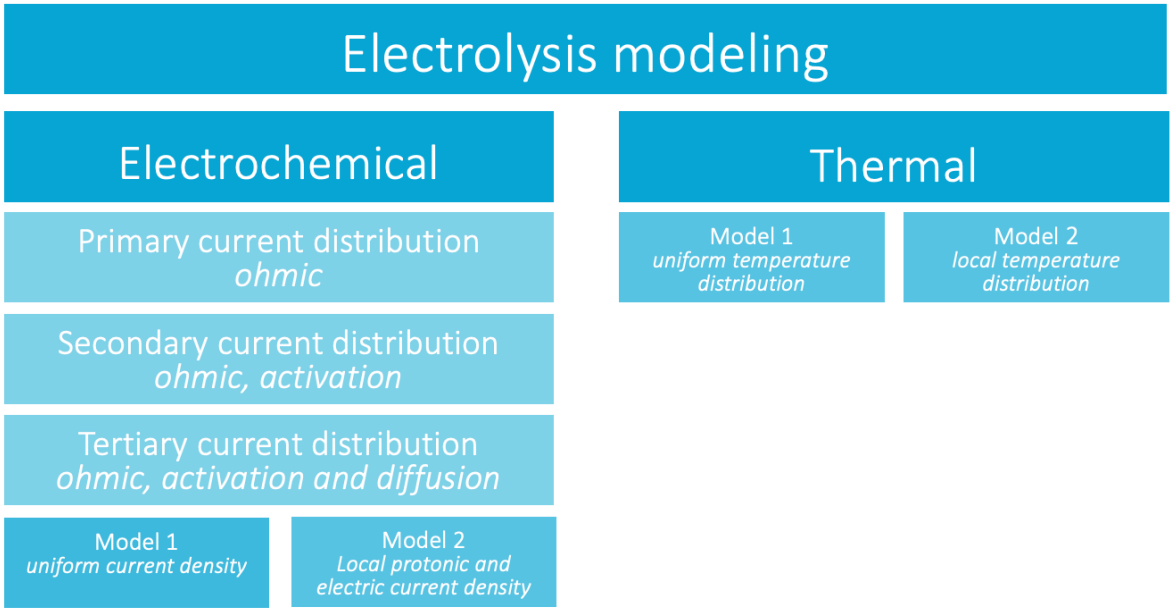

Figure 2.9: A summary of the electrochemical model and thermal model is shown. The electrochemical model can be approached in three ways: (1) a primary current distribution, with only the equilibrium and ohmic overpotential, (2) a secondary current distribution, where the activation overpotential is important, and (3) a tertiary current distribution, where the cell's potential is also dependent on the diffusion overpotential. The thermal model can be divided into ordinary differential equations and partial differential equations, where a uniform and local temperature distribution are taken into account, respectively.

The thermal model and electrochemical model are dependent on each other. As mentioned a steady state electrochemical model and a dynamic thermal model are often used, where sometimes a mass model is implemented as well. However, for this research, also a steady state thermal model is used. This is done considering the computation time.

The temperature in the electrochemical model is continuously updated by the thermal model and vice versa the potential and current density by the electrochemical model. In this way, it is possible to include temperature dependent material properties.

3

Method

In chapter 1 the research question and its subquestions are formulated. In the following chapter, the chosen parameters that are needed in order to answer the research question and subquestions are elaborated. Subsequently, the approach for this research is explained.

3.1. Parameters

The goal of this thesis is to get a better understanding of the heat distribution within an electrochemical cell for different geometries. As different geometries need to be examined for comparison, the membrane electrode assembly (MEA) and the gas diffusion electrode (GDE) are both chosen to investigate. Both geometries can operate at low temperatures. The GDE has an additional electrolyte, and as a result the influence of the electrolyte can assessed. The geometries are discussed in further detail in chapter 4.

Additionally, different input parameters are chosen for the volumetric gas flow rate as it is desired to know the effect of the gas flow rate. The flow rate will have an impact on the concentration gradient and thus on the current distribution. Only two different values are examined, considering the large computation time. The volumetric gas flow rates are chosen within the laminar range and are different in order of magnitude: 10 and 100 ml min^{-1} . The volumetric gas flow rates correspond to a velocity of 0.21 and 2.1 m s^{-1}, respectively. The surface of the gas channel is calculated with the diameter mentioned in Table 4.1. The volumetric flow rate used for the electrolyte remains constant and is assumed to be 0.01 ml min^{-1} in both the anolyte as the catholyte. This corresponds to a maximum velocity of 0.021 m s^{-1}. Due to the parabolic profile, the velocity is not constant, which is calculated in subsection 4.10.7. Consequently, four different models are considered within this research, as can be seen in Figure 3.1.

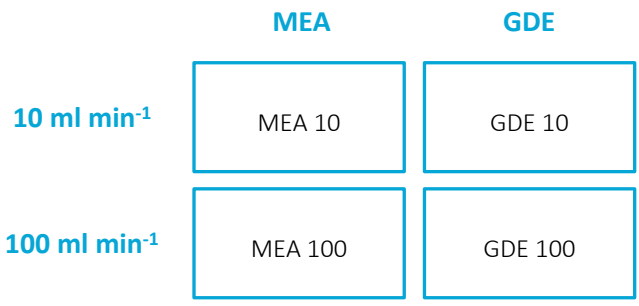

Figure 3.1: Representation of the decisions made in this research. In order to answer the research questions, two different geometries need to be considered. Moreover, it is desired to know the influence of the gas flow rate on the heat distribution. In sum, four different models are looked at in this research.

3.2. Target Product

As stated earlier, research suggested that 16 products were detected for the reduction of carbon dioxide. For the choice of target product, high Faradaic efficiencies and high current densities are preferred. A common target product is carbon monoxide, with a Faradaic efficiency of >95% (using state-of-the-art catalysts and high production rate conditions) [29]. Compared to other potential products, such as alcohols, carbon monoxide has a lower required cell potential. Additionally, carbon monoxide is a desired target product, because of its kinetic accessibility. High current densities can be achieved at high pressure (300 mA cm^{-2}). Therefore, carbon dioxide electrolyzers that have carbon monoxide as a target product are front runners in the commercialization. On that account, this thesis will focus on the carbon dioxide electrolysis with carbon monoxide as a target product.

Half reaction	**Potential [V] vs. RHE**
$CO_2 + H_2O + 2\,e^- \longrightarrow CO + 2\,OH^-$	0.932
$2\,OH^- \longrightarrow \frac{1}{2}O_2 + H_2O + 2\,e^-$	0.404
Total reaction	
$CO_2 \longrightarrow CO + \frac{1}{2}O_2$	1.34

Table 3.1: The half reactions, together with the potentials (vs. RHE) needed to drive the reaction are shown. The total cell reaction is also mentioned, which is calculated by the difference between the anodic and cathodic potential.

In Table 3.1, the half reactions are shown for the conversion of carbon dioxide into carbon monoxide. This is true for standard reference conditions. As can be seen from the Nernst equation, Equation 2.9, it is dependent on the pH, temperature and pressure. The exact potential for the half-reactions be discussed in subsection 4.10.1, where the Shomate equation is used for elevated temperatures under isobaric conditions.

3.3. Approach

To be able to properly model the theoretical heat distribution within an electrochemical cell and subsequently answering the research question, a modeling approach is used. Since two different geometries will be considered, the modeling approach is divided in different intermediate steps.

1. First, a 1-dimensional estimate is made, based on hydrogen PEM fuel cell parameters. The geometry that is modeled is a MEA electrochemical cell. This will be done to check whether the partial differential equations are implemented correctly and to validate the outcomes of the model.
2. Secondly, the 1-dimensional PEM fuel cell model is converted to a 2-dimensional MEA electrolyzer and GDE electrolyzer. Instead of subtracting the losses from the cell potential, the losses are added. For the GDE, extra layers that serve as an electrolyte are added to the model.
3. To answer the research subquestions, both models need to run with the same input parameters, where the only difference is the extra electrolyte layers. In this way, the heat generation within the models can be compared. Moreover, the gas flow rate needs to be altered.
4. A sensitivity analysis will be done for assumed parameters that are uncertain. For this research, a sensitivity analysis will be done for the thermal conductivity of the catalyst layers, as it is expected that a small difference can have an impact on the outcome [15]. Moreover, the influence of the concentration gradient of oxygen is observed, as this gradient is also approximated in the model. If no big difference can be observed, the concentration will not have a big influence on the total outcome and vice versa.

For all steps, the following will be applied: the 2-dimensional models consist of a steady-state thermal model, that is coupled to a steady state electrochemical model. The electrochemical model calculates the needed overpotential with a known current density, incorporating not only activation, but also the diffusion overpotentials. In the thermal model, the ionic and electronic potential will be updated and the new source terms for heat generation can be calculated. The thermal model calculates the temperature by solving the partial differential equations with the finite difference method. In the electrochemical cell the temperature will be updated. This will continue until the temperature difference of the system converges to 10^{-5}. This will be further explained in section 4.4. For the 1-dimensional model, used as validation, the data is used from only one loop.

4

Model

In the following chapter, the model is explained in further detail. The geometries that are taken into account for this research are demonstrated and a comprehensive explanation of the discretization of the conservation equations is given in this chapter. The made assumptions and chosen parameters in this research are listed and the calculations for some parameters are defined.

4.1. Model Geometries

The focus point of this modeling study is to give insight of the heat generation within different electrochemical cells. Another condition that is preferred is that the cell can operate at low temperatures. From the geometries discussed in section 2.2, the gas diffusion electrode (GDE) and the membrane electrode assembly (MEA) are further investigated within this modelling study. This subchapter provides a representation of the cells with its dimensions and the studied plane.

4.1.1. Membrane Electrode Assembly

In Figure 4.1, a representation of the MEA configuration of the electrochemical cell is shown. The numbers 1-9 indicate the separate parts of the cell. Numbers 4 and 6 are not present in the MEA, as these numbers refer to the electrolyte. In Figure 4.1b (3D) and Figure 4.2 (2D), the plane that is taken into account is indicated for the model.

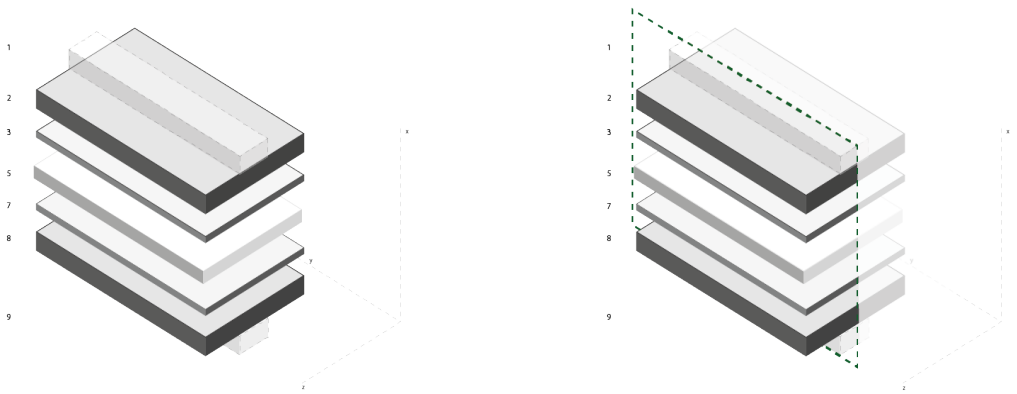

(a) (b)

Figure 4.1: A presentation of the membrane electrode assembly geometry. On the left (a) the full cell in 3D is shown, where on the right (b) the x-y plane is indicated.The gas channels, number 1 and 9, are not included in the model, but approximated by convective boundary conditions.

Figure 4.2: The x-y plane that is taken into account within this modeling research is demonstrated. The gas flows from left to right in the channel (1,9), indicated with the arrow. The anode is indicated with numbers 2,3 and the cathode with numbers 7,8.

4.1.2. Gas Diffusion Electrode

In Figure 4.3, a representation of the GDE configuration of the electrochemical cell is shown. The numbers 1-9 indicate the separate parts of the cell. In Figure 4.3b (3D) and Figure 4.4 (2D), the plane that is taken into account for the model is presented.

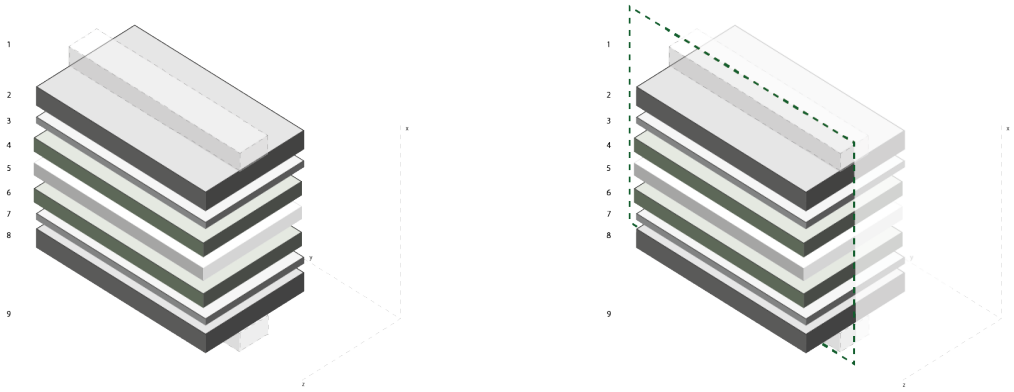

(a) (b)

Figure 4.3: A representation of the gas diffusion electrode geometry. On the left (a) the full cell in 3D is shown, where on the right (b) the x-y plane is indicated. The gas channels, number 1 and 9, are not included in the model, but approximated by convective boundary conditions.

Figure 4.4: The x-y plane that is taken into account within this modeling research is demonstrated. The gas flows from left to right in the channel (1, 9), indicated with the arrow. The anode is indicated with numbers 2,3 and the cathode with numbers 7,8. The electrolyte is indicated with a green color and the numbers 4 and 6. Similar to the channel, the electrolyte flows from left to right, as demonstrated by the arrow.

4.2. Materials

The different layers of the MEA and GDE consist of different materials. Although not much research has been devoted to the heat generation within carbon dioxide electrolysis, many experiments have already been conducted for other research purposes regarding carbon dioxide electrolysis systems. In order to be in line with recently done experiments, materials that are used often in literature and are proven to be advantageous will be chosen as materials for this research. Literature studies that are taken into account are: [12, 34, 53, 54, 56, 59, 86, 92]. In the following subchapter, the separate parts from the MEA and GDE are discussed together with a short description of the material to provide more insight on the decision.

4.2.1. Electrodes

For the cathodic electrode, the material is chosen to be carbon paper. This material is also used in lab-scale experiments, according to the Dioxide Materials technology [25]. According to Lee et al. [56], carbon paper is unstable at oxygen evolution potential. For this reason, the material used for the anode is Ti felt. Moreover, porous electrodes benefit the reaction rate and are used in many experiments. Both electrodes are therefore assumed to be porous electrodes with the same porosity ε_{DL} = 0.8 [90]. The porosity of the electrodes has an influence on the diffusivity and current density in this research.

4.2.2. Catalyst cathode

For this research, the formation of carbon monoxide from carbon dioxide is taken into account. For this specific reaction, silver is considered to have the highest selectivity for the formation of carbon monoxide [26], and is therefore chosen as the cathodic catalyst.

4.2.3. Catalyst anode

For oxygen evolution reaction, IrO_2 is chosen to be the most optimal catalyst. It must be taken into account that it will not be the most optimal material for large scale electrolysis, due to its scarcity and high cost [53].

4.2.4. Membrane

From previous research, e.g. Hori et al. [43], it was found that anion exchange membranes are more suitable for carbon dioxide electrolysis, instead of cation exchange membranes. Sustainion has a high conductivity, leading to less ohmic losses. Furthermore, Sustainion is used as the membrane in multiple experiments and therefore implemented within this modeling study.

4.2.5. Electrolyte

The reduction of carbon dioxide is favoured at basic conditions. Common solutions for the choice of electrolyte are KOH, $KHCO_3$ en K_2CO_3. The research of Liu et al. [59], that examines CO_2 electrolysis to CO with Sustainion membranes, uses 1M KOH. This solution will also be used in this modeling research.

4.3. Dimensions

For this thesis, the plane that is taken into account for the 2D model is the xy-plane, as seen in Figure 4.3 and Figure 4.1 for the GDE and MEA geometry. The dimensions chosen for both the MEA configuration model as the GDE configuration model are shown in Table 4.1. The dimensions are based on dimensions found in literature and are representative in order of magnitude. In spite of the fact that it is part of the electrochemical cell, the current passes through the backing plate with a very low resistance due to the high electric conductivity. As a consequence, it is expected that not much heat will be generated in the backing plate. Therefore, to save computation time, the backing plate is not included in the model. Additionally, the macro- and microporous layer are modeled as one diffusion layer.

For this research, the width of the cell (z-direction) is 10^{-3} m.

#	Part	**Length (x)**, L_x [m]	**Length (y)**, L_y [m]
1	Anodic flow channel	$D_{channel} = 10^{-3}$	10^{-2}
2	Gas diffusion plate (GDP)	10^{-4}	10^{-2}
3	Anodic catalyst layer	10^{-5}	10^{-2}
4	Anolyte	$8{\cdot}10^{-5}$	10^{-2}
5	Membrane	$5{\cdot}10^{-5}$	10^{-2}
6	Catholyte	$8{\cdot}10^{-5}$	10^{-2}
7	Cathodic catalyst layer	10^{-5}	10^{-2}
8	Gas diffusion plate (GDP)	10^{-4}	10^{-2}
9	Cathodic flow channel	$D_{channel} = 10^{-3}$	10^{-2}

Table 4.1: Dimensions of MEA and GDE electrolyzer. These values are based on dimensions found in literature. The numbers are presented in Figure 4.3 and Figure 4.1

4.4. Model development

A 2-dimensional model is developed including a steady state electrochemical model and a steady state thermal model. The total model is divided in three models: the mass model, the electrochemical model and the thermal model, where the relevant conservation equations are considered. For the mass model, the conservation of species is solved:

$$D_i \nabla c_i = S_{c,i} \tag{4.1}$$

The concentration gradient within the electrochemical cell is used as an input for the Butler-Volmer equation, used in the electrochemical model. Subsequently, the electrochemical model is solved using the conservation of charge:

$$\nabla \cdot (\sigma^{eff} \nabla \varphi) = S_{e,m} \tag{4.2}$$

Finally, the ionic and electric potential serve as an input for the thermal model. The potentials and the local volumetric current density determine the local source terms. For the thermal model, the conservation of thermal energy is solved:

$$\rho c_p \left(\vec{V} \cdot \nabla T \right) + \nabla \cdot (k \nabla T) = S_T \tag{4.3}$$

All governing equations are solved using the finite difference method for 2-dimensional steady state problems in Python 3.0. The mesh is formed by non-equally sized spatial iteration steps: Δx=2·10^{-6} and Δy=10^{-4}. The detailed discretization of the models is shown in section 4.8. In the following subchapter, these three models will be discussed in further detail. Moreover, the computational steps are based on the modeling study done by Al-Baghdadi et al. (2007) [5]. A representation of the steps is shown in Figure 4.5.

4.4.1. Simulation

First, input parameters are chosen and all three models are initialized. The electrochemical cell initial has a uniform temperature of 298K, and all parameters are determined by the initial temperature and the desired input current density. Hereafter, the mass model is considered. The mass model is divided in two different submodels: the gas channel together with the channel | cell interface and the transport within the electrochemical cell. Once the mass model reaches a steady state, the concentration gradient is used as an input for the electrochemical model. The higher the concentration loss with respect to the reference concentration input, the less current is obtained. To get an average current density equal to the desired input current density, the current is multiplied by a factor with respect to the average concentration.

Next, the electrochemical model is initialized. The ionic potential is zero at the start. The electric potential on both the anode as cathode is equal to the potential of the electrode together with an initial guess of the local activation overpotential. This is done with the input of the concentration model, where the local overpotentials are calculated, according to the local current density, also explained in section 4.6. Subsequently, the model runs until it reaches steady state. The anodic potential is updated for each loop to remain the average desired current density that is set at the initialization. As the cathodic potential also has to keep a fixed value of the overpotential, the difference between the ionic and electric current needs to be updated as well. Before shifting the anode, the value is updated by shifting the ionic potential to the desired value.

Lastly, the thermal model uses the electrochemical model as an input to set the thermal source terms from Table 4.4. Accordingly, the source terms will determine the temperature profile until it reaches steady state. With the new temperature, the temperature dependent properties within the electrochemical model can be updated: the cell potential, the conductivity and the current density. This goes on until it reaches the convergence criteria. The convergence criteria of the mass, electrochemical and thermal model are defined as the difference between the old and the new maximum concentration, electric potential and temperature for each loop. The convergence criteria of the full model is determined by the difference between the old maximum electric potential and the new maximum electric potential.

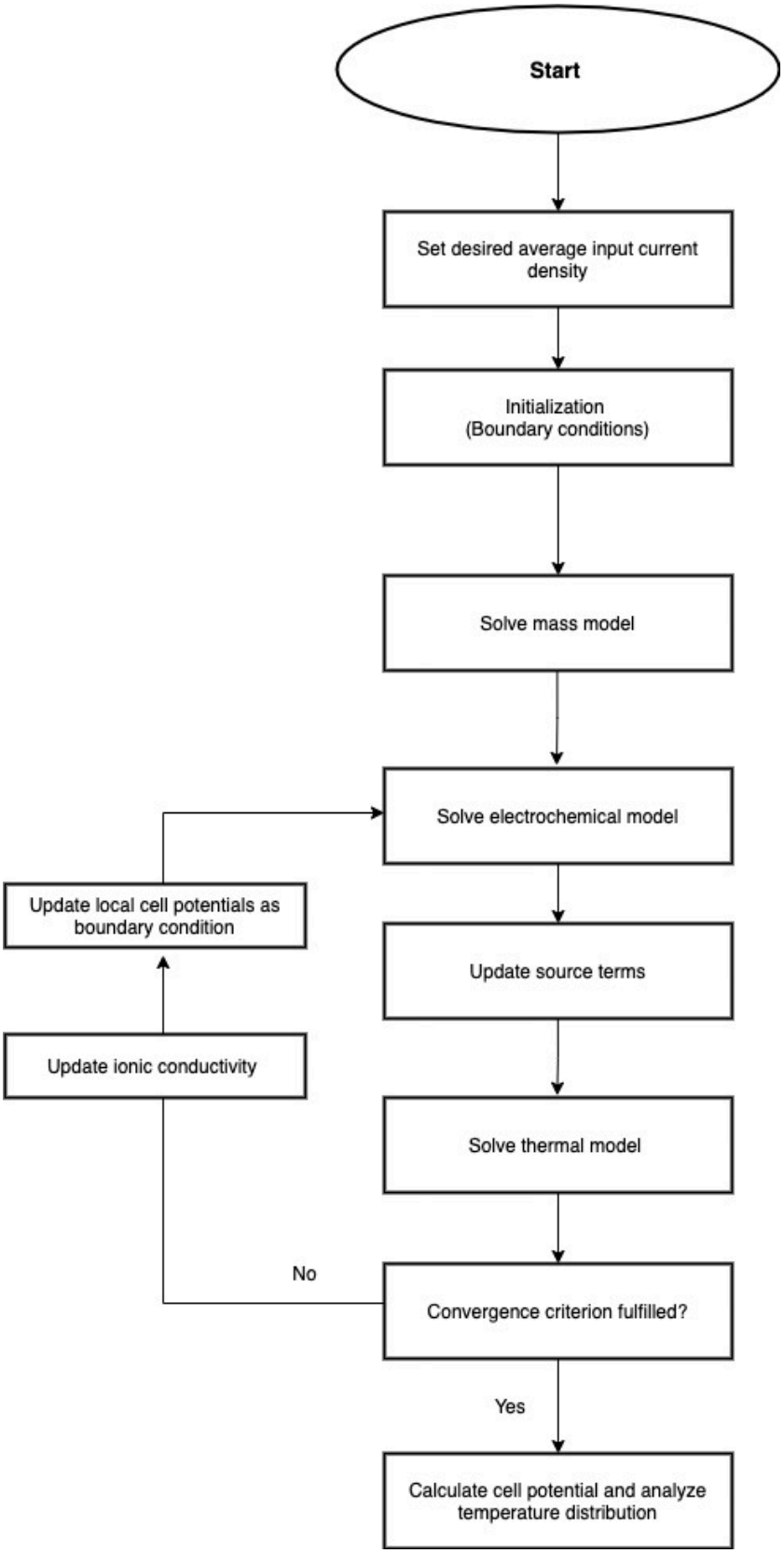

Figure 4.5: The flow diagram, explaining the different steps of the 3 models combined for the simulation.

Operational parameter	Value
Δx	$2 \cdot 10^{-6}$
Δy	10^{-4}
Convergence criteria electrochemical model	10^{-6}
Convergence criteria mass model	10^{-4}
Convergence criteria thermal model	10^{-4}
Convergence criteria full model	10^{-4}

Table 4.2: Operational parameters used for the model. All models have to converge to the indicated value. Finally, the convergence criteria of the full model indicates when the full model reaches steady state.

A more comprehensive explanation of the model can be found in Appendix B, where the full script in Python 3.0 is included.

4.5. Assumptions

To be able to solve the partial differential equations and to avoid over-complexity, pre-made assumptions need to be made. The assumptions are divided into categories.

4.5.1. General

- steady state operation for mass, electrochemical and thermal model;
- single phase flow;
- constant pH;
- the ionic conductivity of the membrane is assumed to be only dependent on temperature.

4.5.2. Transport

- all gases are assumed to be ideal;
- pressure drop is neglected;
- laminar inlet flows;
- developed hydrodynamics within the inlet channels;
- negligible velocity in x-direction;
- sufficient feedstock;
- low saturation in the catalyst layer;
- liquid free diffusion layer;
- small concentrations are considered, so it is assumed that $D_{bulk} = D_{c,i}$;
- contribution from migration is assumed to be negligible.

4.5.3. Thermodynamics

- the heat loss caused by the feedstock flows is set as a convective boundary condition;
- insulated in z-plane;
- all losses generate heat.

4.5.4. Kinetics

- no side reactions, only CO is formed;
- no phase change;
- no bubble formation.

4.6. Boundary Conditions

To be able to solve the partial differential equations in Python 3, boundary conditions need to be specified. For every spacial derivative, a separate boundary condition has to be applied. An explanation of the choice of boundary conditions for this model is given below.

4.6.1. Pressure

Pressure effects are neglected since this research does not involve high-pressure electrolyzers and operates only with laminar flow rates.

4.6.2. Electric potential

The electrochemical cell operates at an average current density equal to the desired input current density. The current runs through the electrode, where the current is calculated locally. An estimation can be made of the needed local overpotential that needs to be applied at the electrodes at the beginning of the loop using the Nernst equation,Equation 2.9 and the Butler Volmer equation, Equation 2.14. Here, the concentration gradients in both directions are also taken into account. With the input current density, the anodic potential can be calculated when considering an electrolyzer.

$$\varphi_{e,anode} = E_{\text{eq, anode}} + E_{\text{act,anode}}. \tag{4.4}$$

Likewise, the cathodic potential can be calculated.

$$\varphi_{e,cathode} = E_{\text{eq, cathode}} + E_{\text{act,cathode}}. \tag{4.5}$$

There are no electrons in the membrane and electrolyte, and therefore there will be no electron transport:

$$\left[-\sigma_e^{eff}\frac{\partial \varphi_e}{\partial x}\right] = 0 \qquad \text{at the CL | EL or AEM boundary.}$$

When running the script, the average current density within the catalyst layer needs to be equal to the desired input current density in order to keep the desired current density at the DL | flow channel interfaces. Therefore the electric potential on the anode shifts with the difference that arises when running the script. The shift can be calculated by first calculating the average concentration, in order to determine the local current density. The local current density is determined by a factor that is equal to the ratio between the local concentration and the average concentration. Hereafter, the difference of the desired local input current density and the mean volumetric current density times the length of the catalyst layer is calculated. This shift needs to be small to avoid errors in the script, so the difference must be multiplied by Δx.

4.6.3. Ionic potential

The transport of ions occurs in the membrane, the electrolyte if present and catalyst layers, where the ionic current decreases strongly in the catalyst layer towards the electrode. There is no ionic transport in the rest of the electrode, meaning the diffusion layer. The initial value of the ionic potential, when no current is running, is zero.

$$\left[-\sigma_m^{eff}\frac{\partial \varphi_m}{\partial x}\right] = 0 \qquad \text{at the CL | DL boundary.}$$

4.6.4. Temperature

For the 1D model, the boundaries at DL | flow channel are held at 298 K. For a 2D model, the inlet flows of the feedstock have been approached by a convective boundary condition, where the temperature of the flow is 298 K:

$$-n\cdot\left(-k_{DL}\frac{\partial T}{\partial y}\right) = h_{T,\,\text{cool}}\,(T_w - T)\,. \tag{4.6}$$

4.6.5. Concentration

For an electrolyzer, at the cathode carbon dioxide is converted into a fuel e.g. CO, and at the anode, oxygen is converted into water. For this model, it is assumed to have sufficient feedstock at the inlet of the flow channel. The flow channel is not included in the model and to compensate this, a convective mass transfer boundary condition is implemented at DL | flow channel. As a consequence, not only a decrease in concentration in the x-direction is obtained, but also along the y-direction. Within the cell, diffusion is the dominant transport mechanism. It is assumed that the reaction is infinitely fast, meaning that all CO_2 is converted to CO at the CL | AEM interface. Also, no diffusion of species occurs in the membrane, so no concentration gradient can be observed.

$$-n\cdot\left(-D_i\frac{\partial C_i}{\partial y}\right) = k_m\,(C_w - C)\,. \tag{4.7}$$

4.6.6. Temperature electrolyte

To ensure that the flow through the electrolyte is continuously refreshed, a boundary condition must be applied at the inlet of the electrolyte channel. The temperature at the inlet remains 298 K, which is the initial temperature, plus additional heat at the beginning. In the electrolyte, a zero gradient boundary condition holds at the outlet of the electrolyte channel.

Variable	AEM or EL | CL	CL | DL	DL | flow channel
Ci	$\frac{\partial C_i}{\partial x} = 0$, C_i=0	-	$-n\cdot\left(-D_i\frac{\partial C_i}{\partial y}\right) = k_m\,(C_w - T)$
T	$\frac{\partial T}{\partial y} = 0$	-	$-n\cdot\left(-k_{DL}\frac{\partial T}{\partial y}\right) = h_{T,\,\text{cool}}\,(T_w - T)$
φ_e	$\frac{\partial \varphi_e}{\partial x} = 0$	-	$\varphi_{e,\text{half reaction cathode}}$ + activation loss
φ_m	-	$\frac{\partial \varphi_m}{\partial x} = 0$	-

Table 4.3: In order to solve the partial differential equations, boundary conditions are needed and presented in this table. No concentration of species is present in the membrane, and the species flux is also zero at the membrane. Since the gas channel is not included in the model, a convective mass boundary condition needs to be applied. The same holds for temperature. Moreover, no electrons are present in the membrane and no ions are present in the diffusion layer. The electric potential at the cathodic boundary is set at the value of the potential of the half reaction plus activation losses.

4.7. Source Terms

In Table 4.4, the source terms for the conservation of energy, species, protons and electrons are shown. The conservation equations used in the model are explained in section 4.4. A brief explanation for the source terms is given in this subchapter.

Conservation of species (Equation 4.1) In the catalyst layer, the flux of Equation 4.1 is related to the current and equal to $\frac{-J_{a,c}}{nF}$. Everywhere else in the cell, the source term is zero.

Conservation of electrons and protons (Equation 4.2) The electric current and the ionic current flow in opposite directions, and therefore the minus signs at the electric and ionic source terms are the exact opposites. As the reactions only occur in the catalyst layers, the flux is related to the current and zero in the other parts.

Conservation of energy (Equation 4.3) The thermal source terms in the anode and cathode catalyst layer are determined from left to right: irreversible, reversible, electric and ionic joule losses. In the electrolyte and membrane, only ionic joule losses occur and similar in the diffusion layer, where only electric losses occur. For this research, the heat generation due to phase change is neglected.

- **Joule heating**:

$$S_{\text{T, Joule}} = \sigma^{eff}\left(\frac{\partial \varphi}{\partial x}\right)^2 = \frac{j^2}{\sigma^{eff}}. \tag{4.8}$$

- **Irreversible heating**:

$$S_{\text{T, irr}} = J_{a,c}\eta_{a,c}. \tag{4.9}$$

  Here, η is the overpotential and is defined as:

$$\eta = \varphi_e - \varphi_m - \varphi_{eq}. \tag{4.10}$$

- **Reversible heating**:

$$S_{\text{T, rev}} = \frac{T\Delta S}{nF}J_{c,a} = (\frac{-\Delta G}{nF} - \frac{-\Delta H}{nF})J_{c,a} = (E_{eq} - E_{tn})J_{c,a}. \tag{4.11}$$

When the thermoneutral potential is larger than the equilibrium potential, heat is needed and one can speak of a heat sink. When the opposite is true, heat is generated and the part of the electrochemical cell acts as a heat source.

	CL anode	CL cathode	AEM - electrolyte	DL
S_{el}	$-J_A$	J_C	0	0
S_{ion}	J_A	$-J_C$	0	0
S_i	$\frac{-J_A}{nF}$	$\frac{-J_C}{nF}$	0	0
S_T	$J_A\eta_A + \frac{T\Delta S}{nF}J_A + \sigma_e^{eff}\left(\frac{\partial \phi_e}{\partial x}\right)^2 + \sigma_m^{eff}\left(\frac{\partial \phi_m}{\partial x}\right)^2$	$-J_C\eta_C + \frac{T\Delta S}{nF}J_C + \sigma_e^{eff}\left(\frac{\partial \phi_e}{\partial x}\right)^2 + \sigma_m^{eff}\left(\frac{\partial \phi_m}{\partial x}\right)^2$	$\sigma_m^{eff}\left(\frac{\partial \phi_m}{\partial x}\right)^2$	$\sigma_e^{eff}\left(\frac{\partial \phi_e}{\partial x}\right)^2$

Table 4.4: The four different source terms, needed to solve the partial differential equations, are shown per part of the electrochemical cell. The electron and ionic soure terms are in opposite directions, since the ions and electrons also flow in opposite directions. The thermal source term represent the heat loss due to irreversible, reversible, and ohmic losses. In the membrane, electrolyte and diffusion layer, only ohmic losses occur.

4.8. Discretization

The conservation equations are explained in chapter 2. This subchapter aims to explain how the conservation equations for species, charge and energy are applied within this modeling study.

4.8.1. Conservation of species

The conservation of species is divided in two different parts: the gas channel and within the electrochemical cell. The concentration within the gas channel is explained at subsection 4.10.5. A convective boundary conditions of the third kind is employed to approximate transport by convection. At the boundary, the diffusion coefficient is assumed to be constant. In Figure 4.6, the discretization of the electrochemical cell at the boundary is shown. A flow with velocity V at the boundaries causes a convective flux, $S_{in,x}$. Furthermore, at the boundary, both advection and diffusion take place, $S_{out,x}$, $S_{in,y}$ and $S_{out,y}$.

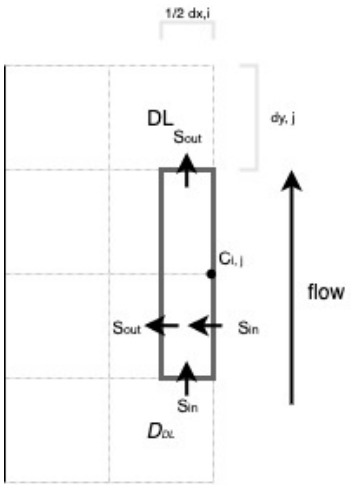

Figure 4.6: The discretization of the concentration at the boundary of the electrochemical cell. A volume is chosen within the electrochemical cell. Note that only half the area in the x-direction is considered. S_{in} and S_{out} represent the transported mass. Since a flow is present, convective mass transfer must be added to the discretization too.

The sum of all fluxes is zero:

$$(S_{in,x} + S_{in,y} - S_{out,x} - S_{out,y}) \cdot A = 0. \tag{4.12}$$

Note that at the boundary, the control volume is $\frac{1}{2}\Delta x\ \Delta y$. The individual terms can be explained as follows:

$$S_{in,x} = k(C_{flow} - C_{i,j}) \cdot \Delta y, \tag{4.13}$$

$$S_{in,y} = D \cdot \frac{C_{i,j} - C_{i,j-1}}{\Delta y} \cdot \frac{1}{2}\Delta x, \tag{4.14}$$

$$S_{out,x} = D \cdot \frac{C_{i,j} - C_{i-1,j}}{\Delta x} \cdot \Delta y, \tag{4.15}$$

$$S_{out,y} = D \cdot \frac{C_{i,j+1} - C_{i,j}}{\Delta y} \cdot \frac{1}{2}\Delta x. \tag{4.16}$$

Adding all terms results in:

$$D \cdot \frac{C_{i,j+1} + C_{i,j-1} - 2C_{i,j}}{\Delta y} \cdot \frac{1}{2}\Delta x - D \cdot \frac{C_{i-1,j} - C_{i,j}}{\Delta y} \cdot \frac{1}{2}\Delta x + k(C_{flow} - C_{i,j}) \cdot \Delta y = 0. \tag{4.17}$$

At last, the concentration at the boundary $C_{i,j}$ can be described as:

$$C_{i,j} = \frac{C_{flow} \cdot \frac{k\Delta y}{D} + C_{i-1,j} \cdot \frac{\Delta y}{\Delta x} + \frac{1}{2}(C_{i,j+1} + C_{i,j-1}) \cdot \frac{\Delta x}{\Delta y}}{\frac{k}{D}\Delta y + \frac{\Delta y}{\Delta x} + \frac{\Delta x}{\Delta y}}. \tag{4.18}$$

Referring to modeling literature, to solve the conservation of species in the electrochemical cell, Fick's third law is used. Looking at Figure 4.7, the discretization of the concentration within the electrochemical cell is as follows:

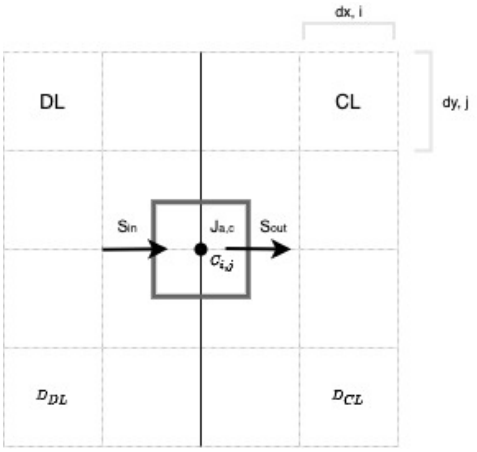

Figure 4.7: The figure shows the discretization for the concentration within the electrochemical cell. A volume between two different material layers is demonstrated: the diffusion and catalyst layer. S_{in} and S_{out} indicate the transported mass. For the two different material layers, two different values for the diffusion coefficient have to be taken into account.

$$S_{in}\Delta y - S_{out}\Delta y + J_{a,c}\Delta x\Delta y = 0. \tag{4.19}$$

With the separate parts for S_{in} and S_{out} as:

$$S_{in} = \frac{(C_{i-1,j} - C_{i,j})}{\Delta x} \cdot \frac{1}{2} \cdot (D_{i-1,j} + D_{i,j}), \tag{4.20}$$

$$S_{out} = \frac{(C_{i,j} - C_{i+1,j})}{\Delta x} \cdot \frac{1}{2} \cdot (D_{i,j} + D_{i+1,j}). \tag{4.21}$$

Note that the diffusion coefficient is variable and different for each layer in the cell. The inclusion of this variable can be observed in Equation 4.20 and Equation 4.21. At the edges of the layers, the flux is defined with the average of the separate diffusion coefficients. The local concentration $C_{i,j}$ can be derived with the following steps:

$$(C_{i-1,j} - C_{i,j}) \cdot \frac{1}{2} \cdot (D_{i-1,j} + D_{i,j}) - (C_{i,j} - C_{i+1,j}) \cdot \frac{1}{2} \cdot (D_{i,j} + D_{i+1,j}) + J_{a,c}\Delta x^2 = 0, \tag{4.22}$$

$$C_{i,j}(D_{i+1,j} + D_{i-1,j} + 2D_{i,j}) = C_{i+1,j}(D_{i+1,j} + D_{i,j}) + C_{i-1,j}(D_{i-1,j} + D_{i,j}) + J_{a,c}\Delta x^2, \tag{4.23}$$

$$C_{i,j} = \frac{C_{i+1,j}(D_{i+1,j} + D_{i,j}) + C_{i-1,j}(D_{i-1,j} + D_{i,j}) + J_{a,c}\Delta x^2}{(D_{i+1,j} + D_{i-1,j} + 2D_{i,j})}. \tag{4.24}$$

4.8.2. Conservation of charge

As the current flows between the electrodes, it is assumed that the diffusion of protons and electrons is only in the x-direction. Again, the summation of fluxes of the ionic and electric potential are zero:

$$(N_{in} - N_{out}) \cdot A + J_{a,c} \cdot V = 0. \tag{4.25}$$

Here, the width can be neglected. Moreover, multiple materials are used, so a local electric or ionic conductivity needs to be included as well. Looking at Figure 4.8, the discretization of the equation of the potential is as follows:

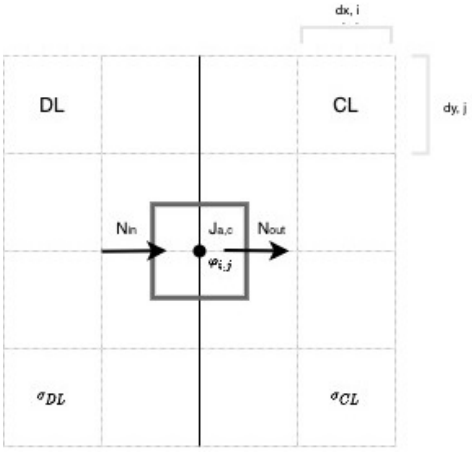

Figure 4.8: A representation of the discretization for the potential within the electrochemical cell. A volume between two different material layers is demonstrated: the diffusion and catalyst layer. N_{in} and N_{out} indicate the transported charge. As two different material layers are considered, different values for the ionic or electric conductivity have to be taken into account.

$$N_{in}\Delta y - N_{out}\Delta y = J_{a,c}\Delta x \Delta y, \tag{4.26}$$

$$N_{in} = \frac{(\varphi_{i-1,j} - \varphi_{i,j})}{\Delta x} \cdot \frac{1}{2} \cdot (\sigma_{i-1,j} + \sigma_{i,j}), \tag{4.27}$$

$$N_{out} = \frac{(\varphi_{i,j} - \varphi_{i+1,j})}{\Delta x} \cdot \frac{1}{2} \cdot (\sigma_{i,j} + \sigma_{i+1,j}). \tag{4.28}$$

All separate parts combined gives:

$$(\varphi_{i-1,j} - \varphi_{i,j}) \cdot \frac{1}{2} \cdot (\sigma_{i-1,j} + \sigma_{i,j}) - (\varphi_{i,j} - \varphi_{i+1,j}) \cdot \frac{1}{2} \cdot (\sigma_{i,j} + \sigma_{i+1,j}) + J_{a,c}\Delta x^2 = 0, \tag{4.29}$$

$$\varphi_{i,j}(\sigma_{i+1,j} + \sigma_{i-1,j} + 2\sigma_{i,j}) = \varphi_{i+1,j}\frac{1}{2}(\sigma_{i+1,j} + \sigma_{i,j}) + \varphi_{i-1,j}\frac{1}{2}(\sigma_{i-1,j} + \sigma_{i,j}) + J_{a,c}\Delta x^2. \tag{4.30}$$

The solution for the local potential results in the following:

$$\varphi_{i,j} = \frac{\varphi_{i+1,j}\frac{1}{2}(\sigma_{i+1,j} + \sigma_{i,j}) + \varphi_{i-1,j}\frac{1}{2}(\sigma_{i-1,j} + \sigma_{i,j}) + J_{a,c}\Delta x^2}{(\sigma_{i+1,j} + \sigma_{i-1,j} + 2\sigma_{i,j})}. \tag{4.31}$$

Note that the source term is zero everywhere except within the catalyst layers.

4.8.3. Conservation of thermal energy

Lastly, for the conservation of energy, the electrochemical cell can be divided into three parts:

1. Boundaries in the x-direction
2. If present: the electrolyte
3. All other parts

Using Equation 4.3 and the boundary equations, all three can be solved. In all parts, heat is distributed via conduction. Since multiple materials are used, the heat transfer coefficients is variable within the electrochemical cell and this must be included.
To start with the energy conservation at the boundaries, the discretization is shown in Figure 4.9. For the boundaries, an additional convection term for the flow needs to be taken into account.

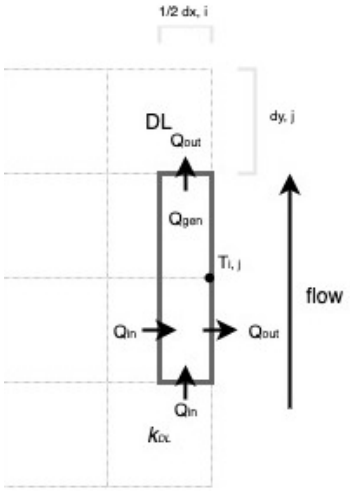

Figure 4.9: The discretization of the temperature at the boundary of the electrochemical cell. A volume is chosen within the electrochemical cell. Note that only half the area in the x-direction is considered. Q_{gen} is the generated heat and Q_{in} and Q_{out} represent the transported heat. Since a flow is present, convective heat transfer must be added to the discretization too.

The separate heat fluxes can be describes as:

$$(Q_{in,x} + Q_{in,y} - Q_{out,x} - Q_{out,y}) \cdot A = 0 \tag{4.32}$$

$$Q_{in,x} = h(T_{flow} - T_{i,j}) \cdot \Delta y \tag{4.33}$$

$$Q_{in,y} = k \cdot \frac{T_{i,j} - T_{i,j-1}}{\Delta y} \cdot \frac{1}{2}\Delta x \tag{4.34}$$

$$Q_{out,x} = k \cdot \frac{T_{i,j} - T_{i-1,j}}{\Delta x} \cdot \Delta y \tag{4.35}$$

$$Q_{out,y} = k \cdot \frac{T_{i,j+1} - T_{i,j}}{\Delta y} \cdot \frac{1}{2}\Delta x \tag{4.36}$$

Adding all fluxes as indicated gives:

$$k \cdot \frac{T_{i,j+1} + T_{i,j-1} - 2T_{i,j}}{\Delta y} \cdot \frac{1}{2}\Delta x - k \cdot \frac{T_{i-1,j} - T_{i,j}}{\Delta y} \cdot \frac{1}{2}\Delta x + h(T_{flow} - T_{i,j}) \cdot \Delta y = 0 \tag{4.37}$$

This results in the following equation for the local temperature at the boundary:

$$T_{i,j} = \frac{T_{flow} \cdot \frac{h\Delta y}{k} + T_{i-1,j} \cdot \frac{\Delta y}{\Delta x} + \frac{1}{2}(T_{i,j+1} + T_{i,j-1}) \cdot \frac{\Delta x}{\Delta y}}{\frac{h}{k}\Delta y + \frac{\Delta y}{\Delta x} + \frac{\Delta x}{\Delta y}}. \tag{4.38}$$

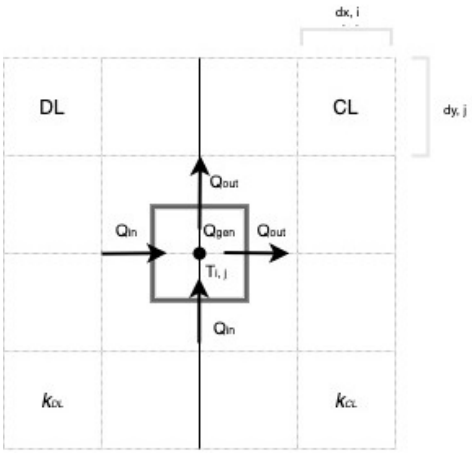

Figure 4.10: The discretization of the temperature within the electrochemical cell. A volume between two different material layers is demonstrated: the diffusion and catalyst layer. Q_{gen} is the generated heat and Q_{in} and Q_{out} represent the transported heat. As two different material layers are considered, the thermal conductivity is variable as well.

In Figure 4.10, a small part of the discretization is shown between the DL and CL. This represents the discretization within the electrochemical cell. Again, seperate fluxes can be added:

$$(Q_{in,x} + Q_{in,y} - Q_{out,x} - Q_{out,y}) \cdot A + Q_{gen} \cdot V = 0, \tag{4.39}$$

$$Q_{in,x} = \frac{(T_{i-1,j} - T_{i,j})}{\Delta x} \cdot \frac{1}{2} \cdot (k_{i-1,j} + k_{i,j}), \tag{4.40}$$

$$Q_{out,x} = \frac{(T_{i,j} - T_{i+1,j})}{\Delta x} \cdot \frac{1}{2} \cdot (k_{i,j} + k_{i+1,j}), \tag{4.41}$$

$$Q_{in,y} = \frac{(T_{i,j-1} - T_{i,j})}{\Delta x} \cdot \frac{1}{2} \cdot (k_{i,j} + k_{i,j-1}), \tag{4.42}$$

$$Q_{out,y} = \frac{(T_{i,j} - T_{i,j+1})}{\Delta x} \cdot \frac{1}{2} \cdot (k_{i,j} + k_{i,j+1}). \tag{4.43}$$

The summation of all fluxes gives:

$$\frac{(T_{i-1,j}-T_{i,j})\cdot\frac{1}{2}\cdot(k_{i-1,j}+k_{i,j})}{\Delta x}\Delta y+\frac{(T_{i,j-1}-T_{i,j})\cdot\frac{1}{2}\cdot(k_{i,j-1}+k_{i,j})}{\Delta y}\Delta x$$

$$-\frac{(T_{i,j}-T_{i+1,j})\cdot\frac{1}{2}\cdot(k_{i,j}+k_{i+1,j})}{\Delta x}\Delta y-\frac{(T_{i,j}-T_{i,j+1})\cdot\frac{1}{2}\cdot(k_{i,j}+k_{i,j+1})}{\Delta y}\Delta x \tag{4.44}$$

$$+Q_{gen}\Delta x\Delta y=0.$$

The local temperature within the electrochemical cell is then formulated as:

$$T_{i,j}=\frac{T_{i+1,j}\frac{1}{2}(k_{i+1,j}+k_{i,j})\frac{\Delta y}{\Delta x}+T_{i-1,j}\frac{1}{2}(k_{i-1,j}+k_{i,j})\frac{\Delta y}{\Delta x}}{(k_{i+1,j}+k_{i-1,j}+2k_{i,j})}$$

$$+\frac{T_{i,j-1}\frac{1}{2}(k_{i,j-1}+k_{i,j})\frac{\Delta x}{\Delta y}+T_{i,j+1}\frac{1}{2}(k_{i,j+1}+k_{i,j})\frac{\Delta x}{\Delta y}}{(k_{i+1,j}+k_{i-1,j}+2k_{i,j})} \tag{4.45}$$

$$+\frac{Q_{gen}\Delta x\Delta y}{(k_{i+1,j}+k_{i-1,j}+2k_{i,j})}.$$

Within the electrolyte, the KOH-solution is continously flowing in the y-direction. An additional convection term within the energy conservation equation needs to be incorporated as well:

$$Q_{in,y}=\frac{(T_{i-1,j}-T_{i,j})}{\Delta y}\cdot\frac{1}{2}\Delta x\cdot(k_{i-1,j}+k_{i,j})+(T_{i,j-1}-T_{i,j})\rho c_pV\Delta x, \tag{4.46}$$

$$Q_{out,y}=\frac{(T_{i,j}-T_{i+1,j})}{\Delta y}\cdot\frac{1}{2}\Delta x\cdot(k_{i,j}+k_{i+1,j})+(T_{i,j}-T_{i,j+1})\rho c_pV\Delta x. \tag{4.47}$$

This results in a local temperature within the electrolyte:

$$T_{i,j} = \frac{T_{i+1,j}\frac{1}{2}(k_{i+1,j}+k_{i,j})\frac{\Delta y}{\Delta x} + T_{i-1,j}\frac{1}{2}(k_{i-1,j}+k_{i,j})\frac{\Delta y}{\Delta x}}{(k_{i+1,j}+k_{i-1,j}+2k_{i,j}+2\rho c_p \Delta x V))}$$

$$+ \frac{T_{i,j-1}\frac{1}{2}(k_{i,j-1}+k_{i,j})\frac{\Delta x}{\Delta y} + T_{i,j+1}\frac{1}{2}(k_{i,j+1}+k_{i,j})\frac{\Delta x}{\Delta y}}{(k_{i+1,j}+k_{i-1,j}+2k_{i,j})+2\rho c_p \Delta x V)} \tag{4.48}$$

$$+ \frac{Q_{gen}\Delta x \Delta y}{(k_{i+1,j}+k_{i-1,j}+2k_{i,j}+2\rho c_p \Delta x V)}$$

$$+ \frac{\rho c_p \Delta x V T_{i,j+1} + \rho c_p \Delta x V T_{i,j-1}}{(k_{i+1,j}+k_{i-1,j}+2k_{i,j}+2\rho c_p \Delta x V)}.$$

4.9. Fixed parameters

The choice of the fixed input parameters are explained in this subchapter. Furthermore, the chosen parameters that are fixed at a temperature of 25 °C and atmospheric pressure are mentioned in the tables below, organised by category: (1) material properties, (2) electrochemical reaction properties, (3) cell operation properties and (4) gas properties.

4.9.1. Input current density

For the model, a desired current density serves as an input. It can be stated from the validation that for the model an uncertainty arises in the range of tertiary current distribution from 1500 mA cm^{-2}. However, for carbon dioxide, high current densities for low temperature electrolysis are not yet achieved. From a review of Küngas et al. (2020) [53], the highest obtained current at which the electrochemical cell can sustain is 400 mA cm^{-2}. For this modeling study, the current is assumed to be 300 mA cm^{-2}.

4.9.2. Exchange current density

For carbon dioxide reduction, common catalysts are IrO_2 for the anode and Ag for the cathode. On the anode, the oxygen evolution reaction takes place in a basic environment. The exchange current density for the anode can be used from other literature studies [62]: $i_{0,anode}$ = 1.4·10^{-5}.
However, the exchange current density for a silver catalyst layer has yet to be determined. This can be obtained by looking at experiments, which is done in the study of Suter et al. [82]. This resulted in an exchange current density in the order of $i_{0,cathode}$ = 10^{-5}.

#	Part	Material	Thermal conductivity k, [$Wm^{-1}K^{-1}$]	Electrical conductivity σ, [Sm^{-1}]
2	Anode diffusion layer	Ti	1.3 [5, 92]	220 [90]
3	Anodic catalyst layer	IrO_2	0.21 (approximated, [4])	100 [92]
4	Anolyte	KOH solution	0.45 [89]	-
5	Membrane	Sustainion	0.17 [14]	-
6	Catholyte	KOH solution	0.45 [89]	-
7	Cathodic catalyst layer	Ag	0.21 (approximated, [4])	100 [92]
8	Cathode diffusion layer	Carbon paper	1.5 [14, 92]	220 [90]

Table 4.5: The variables for the electrochemical and thermal model. The material choice and material properties are based on literature and discussed in section 4.2. Where the material property is unknown, an estimation is made.

T= 298 K, p=1 atm	**cathode**	**anode**
Reference reactant molar concentrations, $C_{i,ref}$ [mol m^{-3}]	50	-
Enthalpy change, ΔH [J mol^{-1}]	109300	174000
Standard Gibss free energy change, ΔG [J K^{-1} mol^{-1}]	179600	77260
Exchange current density, i_0 [A m^{-2}]	10^{-5} [82]	$1.4{\cdot}10^{-5}$ [62]
Transfer coefficient, α [-]	1	1

Table 4.6: The parameters for the electrochemical reaction can be found in this table. At the cathode, the carbon dioxide reduction reaction takes place, where on the anode the oxygen oxidation takes place. The exchange current density is further explained in subsection 4.9.2. The chosen parameters are fixed at a temperature of 25 °C and atmospheric pressure.

T= 298 K, p=1 atm	**Value**
Input current density j, [$mAcm^{-2}$]	300
Volumetric electrolyte flow rate L, [m^3s^{-1}]	$0.1 \cdot 10^{-6}$
Volumetric gas flow rate G, [m^3s^{-1}]	$10, 100 \cdot 10^{-6}$
Initial temperature T_c, [K]	298
Channel temperature T_c, [K]	298
Porosity CL, GDL, ε [-]	0.5, 0.8 [92]
Faraday's constant, F [$Cmol^{-1}$]	96485
Gas constant, R [$Jmol^{-1}K^{-1}$]	8.314
Knudsen radius, R_{Kn} [m]	$0.5{\cdot}10^{-7}$ [90]
Volumetric surface area, a [m]	$(1\text{-}\varepsilon_{CL})\frac{6}{d_{particle}}$ [40]
Liquid water saturation CL, DL, S	0.2 ,0

Table 4.7: The cell operation properties for the electrochemical and thermal model. The chosen parameters are fixed at a temperature of 25 °C and atmospheric pressure.

T= 298 K, p=1 atm	**CO_2**	**O_2**	**1M KOH**
Density, ρ [kg m^{-3}] [64]	1.523 [64]	0.99948 [64]	$1.04{\cdot}10^{3}$ [36, 41]
Thermal conductivity, k [W $m^{-1}K^{-1}$]	0.02119 [64]	0.029921 [64]	-
Dynamic viscosity μ [Pa s]	$1.75{\cdot}10^{-5}$ [64]	2.0947 [64]	-
Specific heat capacity Cp[$Jkg^{-1}K^{-1}$]	-	-	1646.75 [11]
Prandtl number, Pr [-]	0.747 [64]	0.70674 [64]	-
Diffusion coefficient, $D_{c,i}$ [m^2s^{-1}]	$6.49{\cdot}10^{-5}$ [92]	$0.357{\cdot}10^{-4}$ [13]	-

Table 4.8: The gas variables for the electrochemical and thermal model. The chosen parameters are fixed at a temperature of 25 °C and atmospheric pressure.

4.10. Parameter calculation

In this subchapter, the parameters that are calculated with correlations are shown. Also, the extrapolation of the ionic conductivity, which is temperature dependent is mentioned.

4.10.1. Equilibrium potential

In Equation 2.9, the equilibrium potential can be calculated with the Gibbs free energy at standard conditions with an additional term to obtain the equilibrium potential at the relevant temperature. Another way of obtaining Gibbs free energy is from the Maxwell relations. Gibbs free energy is a function of entropy, temperature, volume, pressure, chemical potential and molar number [42]. When considering an isobaric process with a pure substance, the following equation can be derived:

$$\left(\frac{\delta^2 G}{\delta T^2}\right)_p = -\left(\frac{\delta S}{\delta T}\right)_p \tag{4.49}$$

The entropy and enthalpy differences can be approached with the Shomate equation. The parameters are found in the Chemistry Webbook of the National Institute of Standards and Technology (NIST) [58]. In section A.3, the derivation of the enthalpy, entropy and subsequently the Gibbs free energy is explained more extensively. In Figure 4.11, the dotted lines represent the potentials at the anode. The higher the temperature, the larger the difference between the equilibrium and thermoneutral potential. This will result in a larger heat sink at the anode, as the reaction requires more energy to operate 100% thermal efficient. The opposite holds for the reaction at the cathode, as the thermoneutral potential is lower than the equilibrium potential. The higher the temperature, the more heat is expected to be generated.

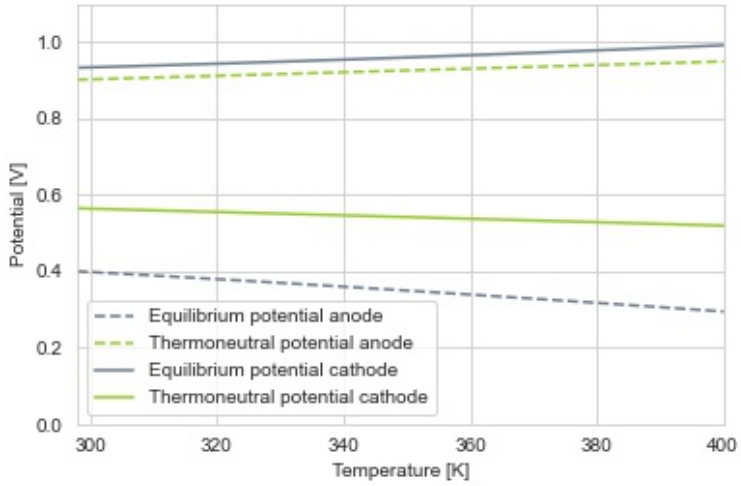

Figure 4.11: A plot with the equilibrium and thermoneutral potentials for both the anode and cathode. The half reactions at the anode are indicated with striped lines, and the half reactions at the cathode with lines. Furthermore, the green color represents the thermoneutral potential. It can be seen that the thermoneutral potential at the anode is larger than the equilibrium potential and at the cathode the thermoneutral potential is smaller than the equilibrium potential. At higher temperatures, for both half reactions, the difference between the equilibrium and thermoneutral potential increases.

In Figure 4.12, the calculated equilibrium and thermoneutral cell potential are plotted. An increase of the thermoneutral potential can be observed, as well as a decrease in equilibrium potential. The difference between the potentials becomes larger at higher temperatures, suggesting that more heat will be required from the system.

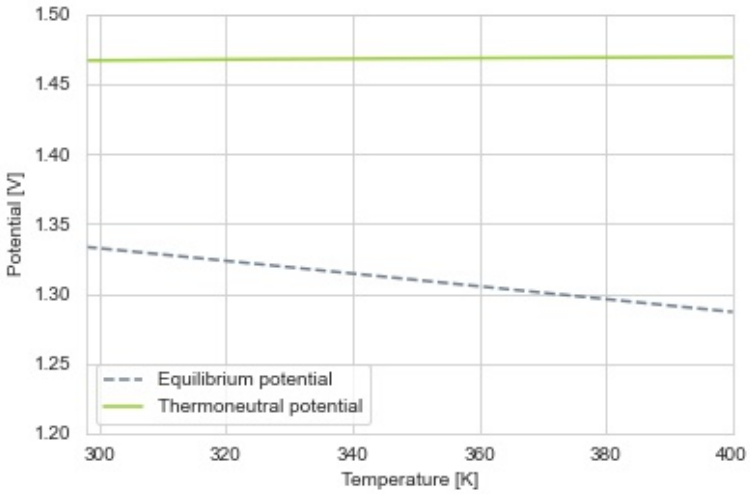

Figure 4.12: A plot of the full electrochemical cell potential. The green line is the thermoneutral potential and the grey line the equilibrium potential. The equilibrium potential is smaller than the thermoneutral potential, suggesting that the overal reaction needs energy from the surroundings to enable a thermoneutral reaction. The difference between the thermoneutral potential and equilibrium potential increases with temperature.

4.10.2. Heat transfer coefficient

The heat transfer coefficient h_y is a function of the Nusselt number. The Nusselt number is the ratio between convective and conductive heat transfer, and can be expressed with the Prandtl number and Péclet number. It is assumed that the flow in the pipe is a laminar hydrodynamic developed flow and thus having a developed velocity profile. On the contrary, the thermal boundary layer can not be assumed to be fully developed and consequently a local Nusselt number needs to be determined.

The correlation for the local Nusselt number for a flow in a pipe with fully developed hydrodynamics is approximated as follows [74]:

$$\mathrm{Nu}_y \sim \left(\mathrm{Pe}\frac{D}{y}\right)^{1/3} \tag{4.50}$$

The Reynolds number indicates the ratio of inertial forces to viscous forces. For a laminar flow in a pipe, the Reynolds number should be below 2300. The Reynolds number is defined as:

$$\mathrm{Re}_D = \frac{\rho u D}{\mu} \tag{4.51}$$

For heat transfer, the Péclet number indicates the ratio between axial advective heat transfer and radial conductive heat transfer [74]. The Péclet number is a function of the Reynolds number and the Prandtl number:

$$\mathrm{Pe} = \mathrm{RePr} \tag{4.52}$$

With the local Nusselt number known, the local heat transfer coefficient can be obtained using Equation 4.53, where the results are plotted in Figure 4.13:

$$h_y = \frac{\mathrm{Nu}_y y}{k} \tag{4.53}$$

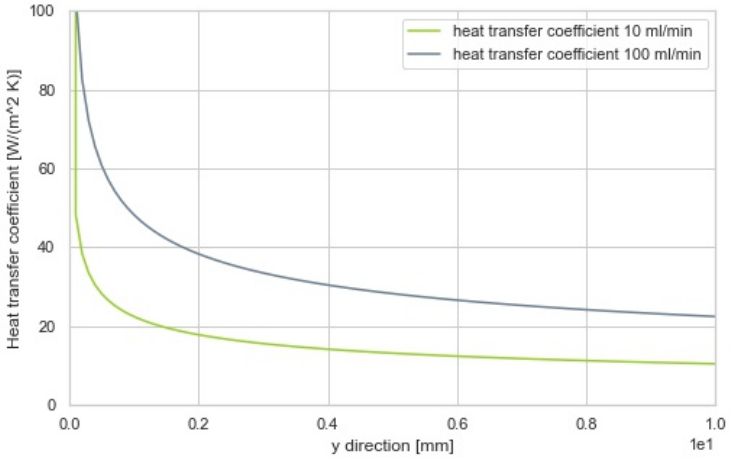

Figure 4.13: The heat transfer coefficient plotted against the channel length. At the beginning, the temperature profile is not yet developed, which results in a higher heat transfer coefficient. Further along the channel, the heat transfer coefficient decreases to a constant value.

4.10.3. Diffusion coefficient

The effective diffusion coefficient can be determined by three diffusion mechanisms: the ordinary diffusion, Knudsen diffusion and surface diffusion. Surface diffusion is dominant for very small pores, when the ordinary diffusion and Knudsen diffusion are very small. At intermediate pressures and pore sizes, it can be assumed that only Knudsen and ordinary diffusion are relevant to describe the mass transport.

Ordinary diffusion describes the diffusion from the particle movements from a higher concentration to a lower concentration, where molecules collide with each other. Ordinary diffusion can be calculated accordingly to Wang et al. [90] for the catalyst layer and diffusion layer [90]:

$$D_{i,CL}^{eff} = D_{c,i}(1-S)^2\left(\frac{\varepsilon - 0.25}{1-0.25}\right)^2 \tag{4.54}$$

$$D_{i,DL}^{eff} = D_{c,i}(1-S)^{2.15}(0.906\varepsilon - 0.252). \tag{4.55}$$

The liquid water saturation S can have a large influence on the effective diffusion coefficient. The liquid saturation in the catalyst layer is assumed to be constant and is listed in Table 4.7. The diffusion layer is assumed to be liquid free [92]. The influence of the porosity on the diffusion coefficient is incorporated in the correlations.
Knudsen diffusion describes the free molecule flow, and is important when the molecules also collide with the walls. Knudsen diffusion can be calculated as follows [64]:

$$D_{Kn,i} = 97 r_{Kn} \sqrt{\frac{T}{M_i}}, \tag{4.56}$$

where M [kg mol^{-1}] is the molar mass of the compound and r_{Kn} [m] is the Knudsen radius.
An approximation can be made for the effective diffusion coefficient by assuming that the separate diffusion mechanisms are additive resistances [64]:

$$D_{c,i} = \left(\frac{1}{D_{Kn,i}} + \frac{1}{D_{ij}^{eff}} \right)^{-1} \tag{4.57}$$

When looking at the order of magnitude, Knudsen diffusion is in the order of 10^{-2} and the effective ordinary diffusion in the order of 10^{-5} - 10^{-6}. Applying Equation 4.57, Knudsen diffusion does not affect the effective diffusion coefficient in a significant manner. Hence, the contribution of Knudsen diffusion to the effective diffusion coefficient can be neglected. The implementation of the varying effective diffusion coefficient is further explained in section 4.8.

4.10.4. Mass transfer coefficient

The mass transfer coefficient k_m is a function of the Sherwood number Sh:

$$k_{m,y} = \frac{\mathrm{Sh}_y y}{D_{c,i}} \tag{4.58}$$

Similar to the temperature profile, the concentration profile of the inlet, CO_2, is also not fully developed and consequently the mass transfer coefficient will decrease along the y-direction. As a result, a local Sherwood number is needed. The Sherwood number is analogue to the Nusselt number, and for this reason the correlation used for the heat transfer coefficient can be used for estimating the mass transfer coefficient. Where the Prandlt number is the ratio between momentum and thermal diffusivity, the Schmidt number is the ratio between viscous and molecular diffusivity. The Schmidt number is analogue to the Prandtl number and therefore, the Peclet can be expressed with the Reynolds number and Schmidt number.

$$\mathrm{Sh}_y \sim \left(\mathrm{ReSc} \frac{D}{y} \right)^{1/3} \tag{4.59}$$

In Figure 4.14, the profile of the mass transfer coefficient is plotted.

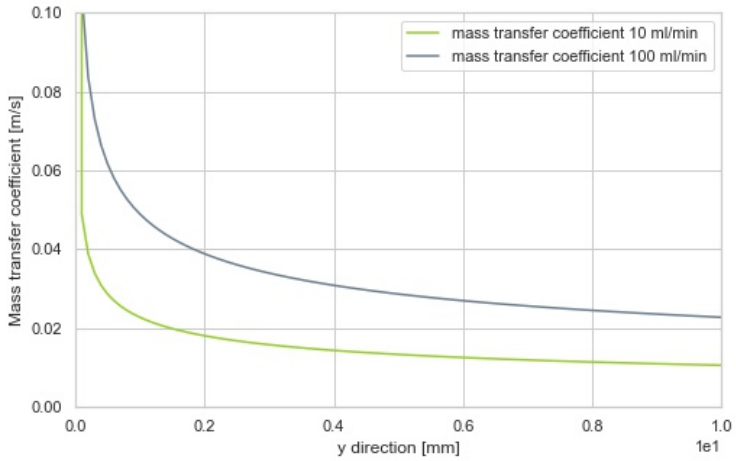

Figure 4.14: The mass transfer coefficient plotted against the channel length. At the beginning, the concentration profile is not yet developed, which results in a higher mass transfer coefficient. Further along the channel, the mass transfer coefficient decreases to a constant value.

4.10.5. Concentration gas channel

In the gas channel, the concentration losses due to advection are dominant. The losses due to diffusion from the bulk to the channel | cell interface are ignored. Therefore, the concentration gradient can be approximated by an exponential decrease [40]:

$$c_{CO_2} = e^{-\frac{\langle S \rangle}{Gz}\tilde{y}} \tag{4.60}$$

Here, S is the mass transfer resistance, equal to the Sherwood number in the channel and in the diffusion layer. For a gas flow rate of 10 and 100 ml min^{-1}, the concentration profile for both geometries looks like the following:

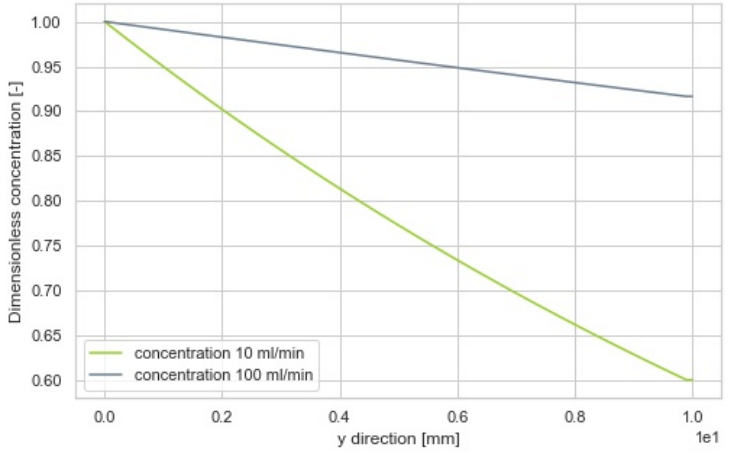

Figure 4.15: The concentration profile along the y-direction at 10 and 100 ml min^{-1}: due to advection the concentration decrease is exponentially. The slope is determined by the Sherwood number and Graetz number.

Furthermore, convective mass losses needs to be included. As explained above, the mass transfer coefficient determines the mass flux to the electrochemical cell. The higher the mass transfer coefficient, the more efficient mass will be transported. For this reason, more mass will be transported to the electrochemical cell at the beginning of the channel, as the Sherwood number will be very large due to an undeveloped concentration profile.

4.10.6. Ionic conductivity

The ionic conductivity is dependent on the temperature. Therefore, a relation between the temperature and the ionic conductivity of the Sustainion membrane is derived from data obtained from an experiment of Dioxide Materials [44]:

$$\sigma_m = 0.12T + 4.05, \tag{4.61}$$

where T is in °C. In Appendix A.4. the derivation for the polyfit is shown in further detail. For the electrolyte KOH, the ionic conductivity is a fixed value $\sigma_{m,KOH} \sim 10$ [Sm^{-1}] [6].

4.10.7. Electrolyte velocity profile

A fully developed velocity profile is assumed within the electrolyte, which is plotted in Figure 4.16. The flow rate of the electrolyte is assumed to be 0.1 ml min^{-1} in both the anolyte as the catholyte, which corresponds to a maximum velocity of 0.021 m s^{-1}. The surface of the electrolyte is calculated with the length of the electrolyte times the width of the electrochemical cell.

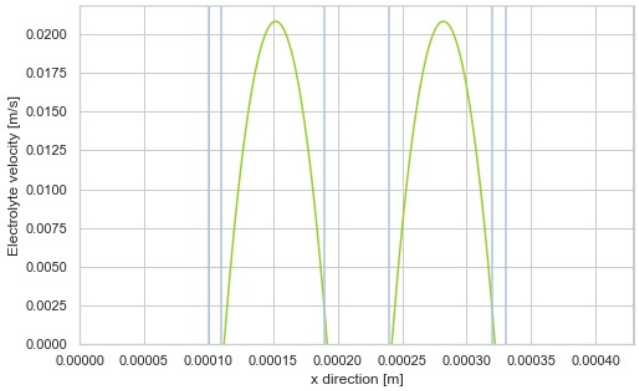

Figure 4.16: The velocity profiles in the anolyte and catholyte. Since it is assumed to have a developed velocity profile, the velocities are assumed to have a parabolic profile. The highest temperature is 0.021 ms^{-1}.

4.11. 1D Model Validation

Since not much research is devoted to carbon dioxide electrolysis, parameters for hydrogen electrolysis are examined in order to validate this model. The parameters of the hydrogen PEM fuel cell of the research of Wang et al. [90] are used for validation. Below, the electrochemical model is validated with the polarization curve. The temperature model is first analytically validated, and afterwards validated by looking at the source terms of the research of Wang et al.[90]. In addition, the research of Burheim et al. [15] is considered, where the temperature profiles are compared.

4.11.1. Comparison of the Polarization Curve

For the polarization curve, the current density is plotted against the calculated cell potential. The cell potential includes activation, ohmic and diffusion losses and is calculated using Equation 2.20. There are 11 different current densities used as input, in a range from 0 to 2200 mA cm^{-2}. In Figure 4.17, the polarization curve of the article of Wang et al. [90] is plotted as well as the polarization curve obtained from the 1-dimensional model. It must be emphasized that there are some differences with the model used in the research of Wang et al. [90] and the model made for this research. The backing plate and a separate microporous layer (MPL) are not considered in this research. The ohmic losses within these layers is not taken into account for the calculations of the grey line, but must be included for comparison. These additional ohmic losses are calculated by including the ionic and electric conductivities, together with the lengths of the microporous layer and the backing plate of the article. The two green lines show the polarization curve with the correction for ohmic losses that are not taken into account in the model of this research. Also, even more ohmic losses can be added due to the uncertainty of the ionic conductivity used in the article. The ionic conductivity ranges from 2.5 Sm^{-1} to 12 Sm^{-1}, which is based on ionic conductivities found for a Nafion membrane. As can be seen in Figure 4.17, the

polarization curve of the model with correction corresponds to the polarization curve from Wang et al. [90]. From the range from 0 to 1400 mA cm^{-2}, the corrected curve, considering a low membrane conductivity, is off with less than 1%. At higher currents, the diffusion overpotential plays a bigger role, and it can be seen from Figure 4.17 that the difference between the curves is larger, up to 16% for the low membrane conductivity and 47% for the highest considered membrane conductivity. Since the diffusion overpotential is not the main focus of this research, it can be stated that the model gives a good interpretation of other experiments done in previous research.

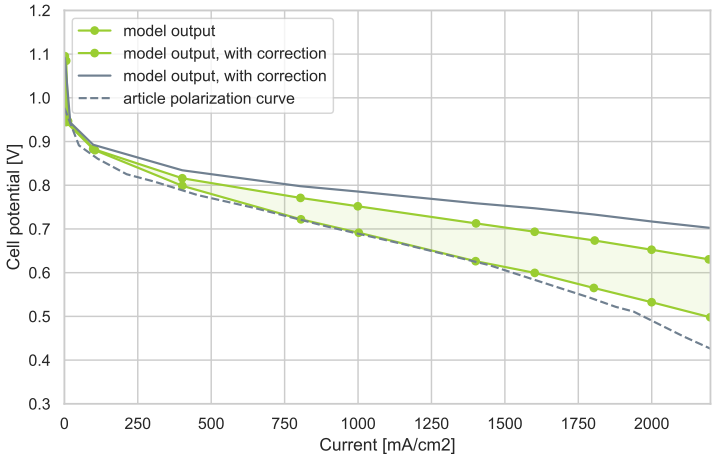

Figure 4.17: The polarization curve from [90] is compared to the results from the model. The orange line represents the outcome without correction for ohmic losses. The green lines are obtained by including additional ohmic losses, with an uncertainty in the ionic conductivity in the membrane. For an ionic conductivity of 2.5 Sm^{-1}, the lines are matching until higher current densities.

4.11.2. Analytical Comparison Thermal Model

The thermal model is first validated analytically, where the source terms and thermal conductivity where kept constant and independent of the electrochemical model. The grey line shows the analytic validation. The analytical calculation and the modeling calculations show a matching profile. From this, it can be stated that the partial differential equations in the model are implemented correctly.

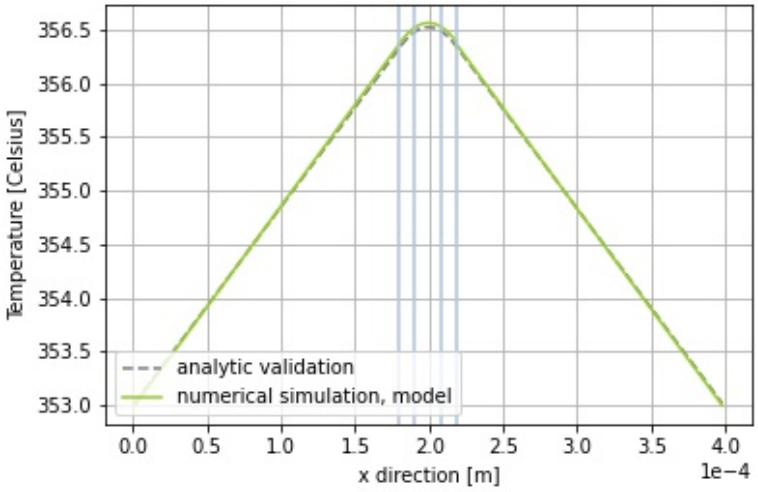

Figure 4.18: Plot of the temperature distribution to check whether the partial differential equations for 1D are implemented correctly. This is done by comparing it with analytical calculations, the grey striped line. It can be seen that the lines are matching.

4.11.3. Analytical Comparison Cathodic Source Terms

To get an idea of the magnitude of order of the heat generation, a pre-calculated estimation of the source terms is done. This estimation of the overpotential can be made by approximating the overpotential with the Butler Volmer equation with the desired current density. The heat generations are analytically calculated with a constant temperature and compared to the outcomes of the model. Within the cathodic catalyst layer, the following heat generations take place:

- Protonic and electric joule heating
- Irreversible heat
- Reversible heat

For the comparison of the source terms in W cm^{-3}, temperature deviations will not be taken into account. Furthermore, the desired current density is assumed to be 2200 mA cm^{-2} and the volumetric current density $2.2 \cdot 10^{-8}$ mA cm^{-3}.
In Table 4.9, the equations used for the estimated values for the source terms are mentioned. All calculations are compared with the local current density and overpotentials in the center of the catalyst layer. The order of magnitude for each heat source is comparable. However, looking at joule heating, the model predicts twice as much electronic heat generation, where the estimation of protonic joule heating is approximately half the amount of the heat generation by the model.

Heat source	Equation estimation	Outcome estimation	Outcome model
Electronic joule heating, [Wcm^{-3}]	Equation 4.8	2.42	4.06
Protonic joule heating, [Wcm^{-3}]	Equation 4.8	40.33	24.37
Reversible heating, [Wcm^{-3}]	Equation 4.9	182.99	182.99
Irreversible heating, [Wcm^{-3}]	Equation 4.11	657.74	676.43

Table 4.9: The estimated values, calculated with equations mentioned in this research, for the different types of heat generation are compared to the outcomes of the model. There is some uncertainty looking at joule heating, but the reversible and irreversible heat sources are quite similar and are expected to have the most impact on the total heat generation.

4.11.4. Temperature Profile Validation

Visible in Figure 4.19, most heat is generated within the cathodic catalyst layer for a fuel cell. When comparing this to the graph Wang et al. (2021, Figure 2a) [90], a similar profile of the graph can be observed qualitatively, but not quantitatively. A lower temperature is obtained in the validation, which can be explained by a lower heat generation. A lower conductivity can cause higher ohmic losses and thus higher source terms, as can be seen in Figure 4.17. Another explanation is not including a difference in conductivity for the microporous and macroporous layer within the diffusion layer.

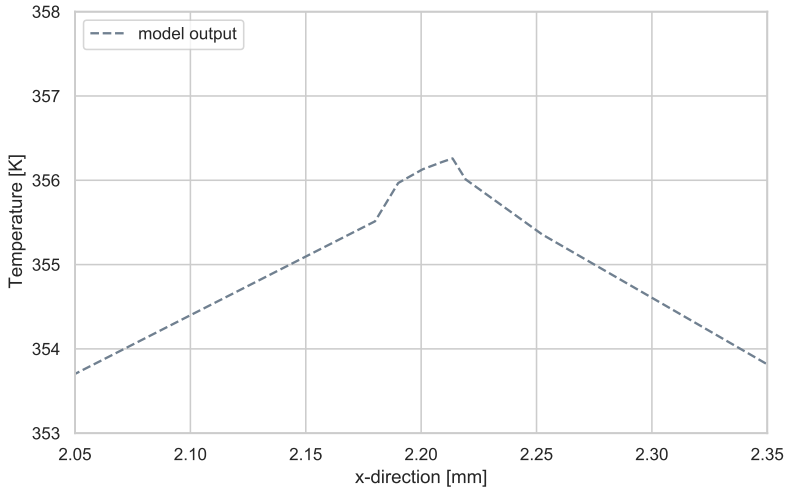

(a) Model temperature profile

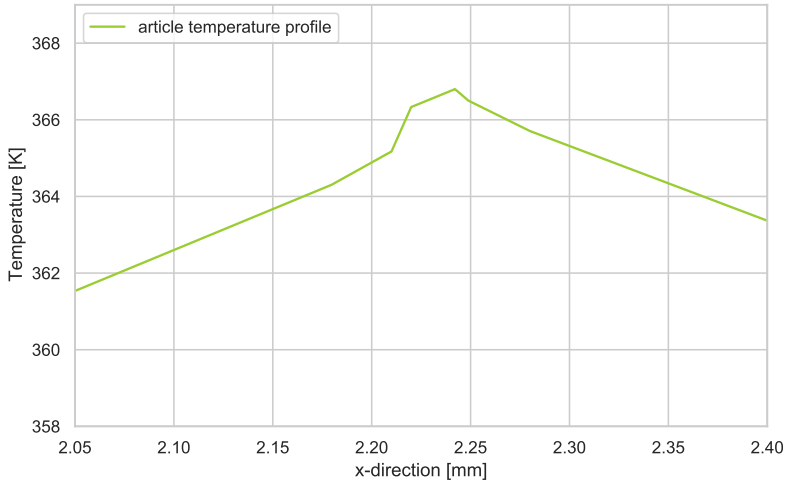

(b) Article temperature profile

Figure 4.19: Plot of the steady state temperature distribution within a MEA hydrogen fuel cell. The data from the left figure (a) is obtained from the model in Python, where the anode is on the left and the cathode is on the right. The highest temperature can be observed at the cathode. The temperature profile is in agreement with temperature profiles found for hydrogen fuel cells in the literature qualitatively, but not quantitatively. An example from the research Wang et al. [90] (2021), that is shown in (b).

4.11.5. Carbon Dioxide Electrolysis Heat Generation

An initial guess of the heat sources for every location within the electrochemical cell is made. This is done in the same fashion as the estimation done in subsection 4.11.3. Since this research is focusing on electrolyzers, all reactions are endergonic. This means that a energy, driven by the potential, needs to be applied for the reaction as the reaction is non-spontaneous. At the anode, the equilibrium potential is lower than the thermoneutral potential. From this, it can be seen that reversible losses in the anode are negative. On the contrary, the cathodic reaction has a lower thermoneutral potential than the equilibrium potential. As a result, the excess energy from the potential is converted into thermal energy and therefore acts as a heat source. Similar, the activation overpotentials that are applied to the system are converted into thermal energy. It can be concluded that most heat generation is expected to be in the cathodic catalyst layer. It can also be suggested that not much heat generation can be expected from losses in the diffusion layer. Compared to the hydrogen fuel cell of Wang et al. (2021) [90], more heat generation is expected at the cathode and anode. The activation overpotentials are

larger at both the anode and the cathode. Approximately 0.75 versus 0.18 V for the anodic reactions for a carbon dioxide electrolyzer and a hydrogen fuel cell, respectively. Moreover, 1.19 versus 0.3 V approximately for the cathodic reaction.

Heat souce	DL	CL anode	CL cathode	electrolyte	AEM
Electronic joule heating, [Wcm^{-3}]	0.041	0.09	0.09	-	-
Protonic joule, [Wcm^{-3}]	-	0.9	0.9	0.9	1.125
Reversible heating, [Wcm^{-3}]	-	-149.6	448.8	-	-
Irreversible heating, [Wcm^{-3}]	-	225.4	358.1	-	-
Total	0.041	76.79	807.89	0.9	1.125

Table 4.10: An estimation for the heat generation within the electrochemical cell is made, to predict the temperature distribution of the electrochemcical cell. It can be seen that the anode acts as heat sink and the cathode as a heat source, where the summation suggest that the temperature of the electrochemical cell will increase due to the losses.

5 Results

In this chapter, the results of the models are shown. The relevant results from the electrochemical model are the potential and the current density. For thermal model, the temperature and the heat generation are important. The results are discussed side by side for the volumetric flow rates. For each model, the MEA will be analysed first, followed by the GDE.

5.1. Electrochemical results

First, the results of the electrochemical model are presented. The electrochemical model serves as an input for the thermal model, although the potentials are influenced by the temperature calculated in the thermal model. The local current density and the activation overpotential in both catalyst layers are discussed in further detail.

5.1.1. MEA current density

The mean current density in the electrochemical cell is equal to the desired input current density and determined by the concentration profile of carbon dioxide in the y-direction. For both flow rates, the mean current density is equal to the input current density, 300 mA cm^{-2}. Figure 5.1c shows that the current is more evenly distributed for 100 ml min^{-1}, compared to 10 ml min^{-1}. In addition, the deviations from the dimensionless mean current density is 0.3 and 0.04 for 10 and 100 ml min^{-1}, respectively. Looking at Figure 4.15, it can be observed that the concentration is more linear for 100 ml min^{-1}.

(a)

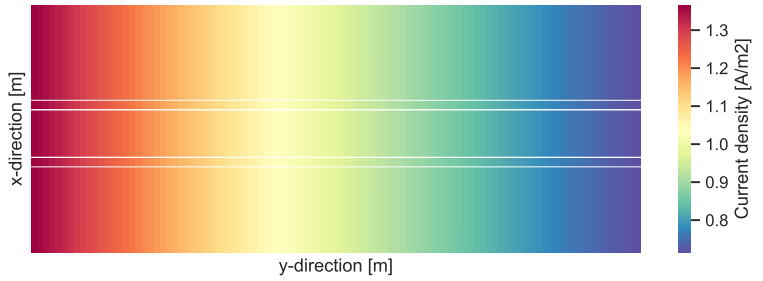

(b) 10 ml min^{-1}

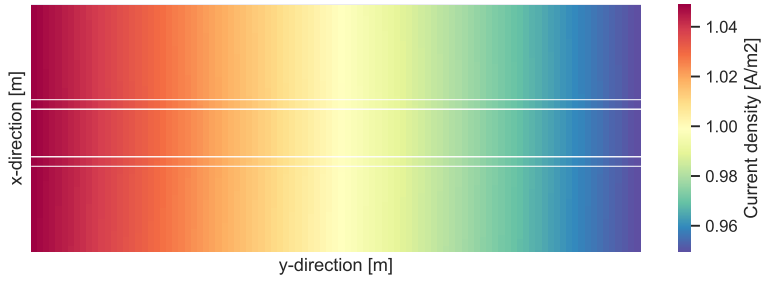

(c) 100 ml min^{-1}

Figure 5.1: (a) Representation of the xy-plane of the MEA that is considered within this modeling study. The different layers include the channel, diffusion layer (DL), catalyst layer (CL), and anion exchange membrane (AEM). Figure b and c show the 2-dimensional current density of the MEA geometry for (b) 10 ml min-1 and (c) 100 ml min-1. The current density distribution corresponds to the concentration gradient and is calculated using the ratio with the mean current density. **Note that the legends are not similar**.

5.1.2. GDE current density

The current density for 10 ml min^{-1} and 100 ml min^{-1} are shown in Figure 5.2b and in Figure 5.2c, respectively. The concentration profile in the y-direction is influenced by the volumetric flow rate, but is not dependent on the geometry. Consequently, the same current density range can be obtained compared to a MEA geometry. Similar to the results for the MEA, the current density is better distributed for higher flow rates, 100 ml min^{-1}. Higher current densities can be observed for 10 ml min^{-1} close to the inlet. This observation is in line with the concentration profile, as the profile is less linear and therefore the concentration difference with respect to the mean dimensionless concentration is larger for lower flow rates. On the other hand, at the outlet, the current density is lower for a flow rate of 10 ml min^{-1}.

(a)

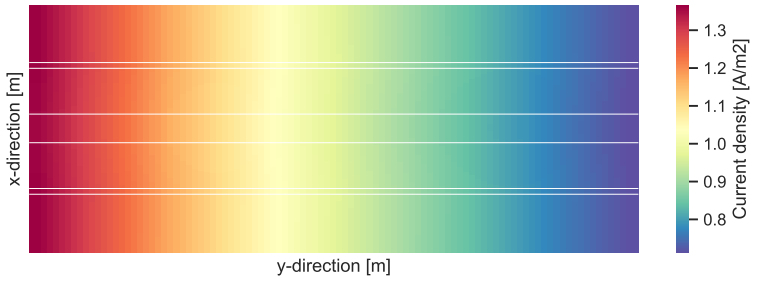

(b) 10 ml min^{-1}

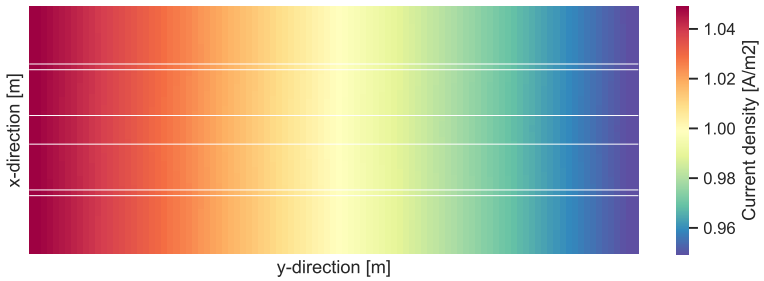

(c) 100 ml min^{-1}

Figure 5.2: (a) Representation of the xy-plane of the GDE that is considered within this modeling study. The different layers include the channel, diffusion layer (DL), catalyst layer (CL), electrolyte (EL) and anion exchange membrane (AEM). Figure b and c show the 2-dimensional current density of the GDE geometry for (b) 10 ml min−1 and (c) 100 ml min−1. The current density distribution corresponds to the concentration gradient and is calculated using the ratio with the mean current density. **Note that the legends are not similar**.

5.1.3. MEA potential

The activation overpotential is calculated with the Butler-Volmer equation and it resembles the extra potential that is needed for the reaction. Figure 5.3 presents the anodic activation overpotential and Figure 5.4 the cathodic overpotential in the middle of the cell. Towards the membrane, the activation overpotential in the cathodic catalyst layer becomes more negative. This can be related to the decreasing concentration of CO_2. Since it is assumed that a higher concentration of OH^- is present at the CL | AEM interface, less activation potential is needed, which is in line with the potential profile in Figure 5.3. For higher flow rates, higher activation overpotentials are needed in the anode. On the other hand, higher activation overpotentials are calculated for lower flow rates in the cathode.

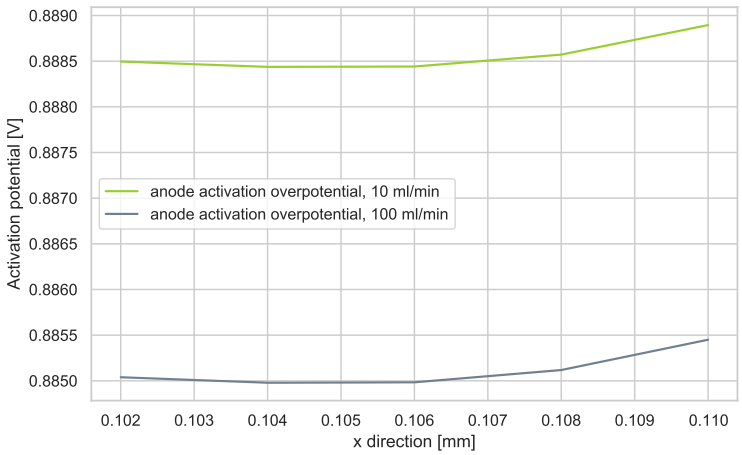

Figure 5.3: The activation overpotential is plotted against the x-direction and demonstrates the profile of the activation overpotential within the anodic catalyst layer. Both flow rates are plotted in the graph, where higher values are obtained for 100 ml min^{-1}. Near the membrane, larger values for the activation overpotential can be observed.

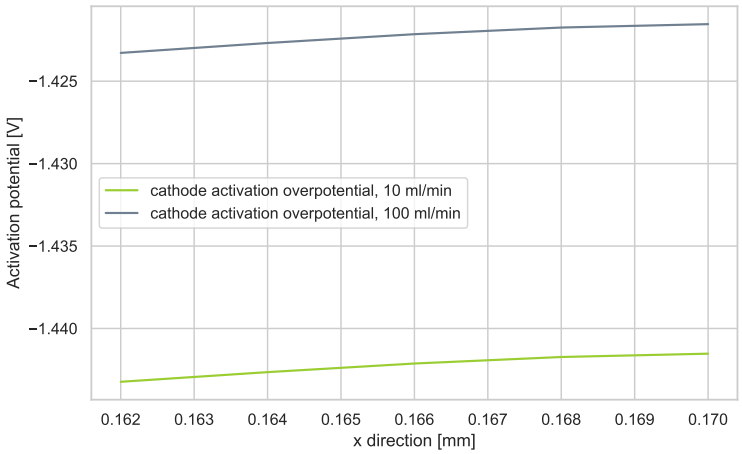

Figure 5.4: The activation overpotential is plotted against the x-direction and demonstrates the profile of the activation overpotential within the cathodic catalyst layer. Both flow rates are plotted in the graph, where more negative values are obtained for 10 ml min^{-1}, indicating that more heat will be generated. Near the membrane, more negative values for the activation overpotential can be observed.

5.1.4. GDE potential

The graphs in Figure 5.5 and Figure 5.6 show the anodic and cathodic activation overpotentials. Again, the left graph shows the higher flow rate, 100 ml min^{-1}. Similar to the MEA, a higher activation overpotential is required at the anode for higher flow rates. Also, a higher activation overpotential is required for lower flow rates at the cathode. The anodic and cathodic overpotential profiles for the GDE are qualitatively similar to those of the MEA. A higher activation overpotential is calculated for the MEA compared to the GDE. The higher overpotential of the MEA can be related to steeper increase in temperature for the same configuration.

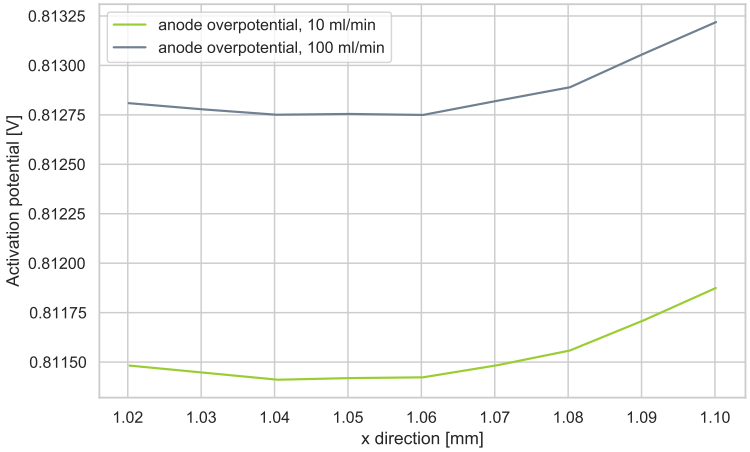

Figure 5.5: The graph shows the activation overpotential within the anodic catalyst layer for a GDE geometry. The grey line indicates the gas flow rate of 100 ml min^{-1}, where the green line represents the gas flow rate of 10 ml min^{-1}. The gas flow rate of 10 ml min^{-1} has higher obtained values, indicating that more heat is generated.

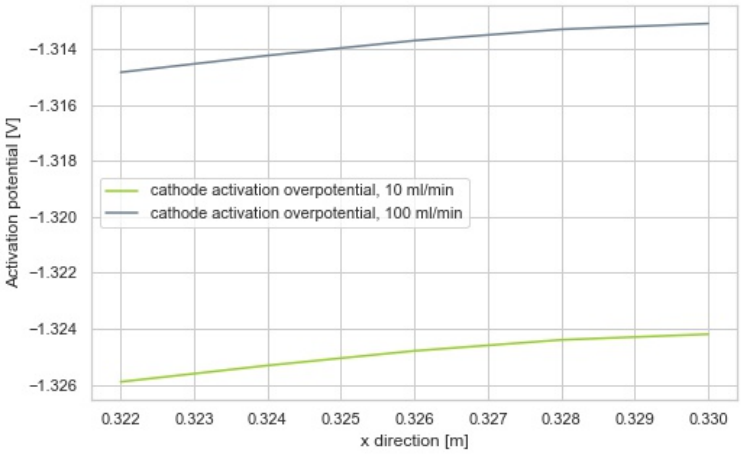

Figure 5.6: The graph shows the activation overpotential within the cathodic catalyst layer for a GDE geometry. The grey line indicates the gas flow rate of 100 ml min^{-1}, where the green line represents the gas flow rate of 10 ml min^{-1}. The gas flow rate of 10 ml min^{-1} reach more negative values, indicating that more heat is generated.

5.2. Thermal results

The results of the thermal model are discussed in this subchapter. The temperature distribution is discussed in further detail in 2D and 1D. The legends for the 2D temperature plot differ to emphasize the individual hot-spots. A 2D plot of the heat distribution is also presented. Also, the separate heat sources are plotted within the catalyst layers. This will give insight to the individual contribution of the heat source of the heat generation.

5.2.1. MEA temperature distribution

In Figure 5.7, the temperature in the x-direction of both flow rates is plotted. The y-location is fixed at half the channel length. In the middle of the cell, the flow rate of 100 ml min^{-1} reaches a higher temperature than for flow rates at 10 ml min^{-1}. The difference of the maximum temperatures is less than 1 K. A temperature decrease at the anode can be seen for both flow rates. This can be explained by the fact that the anode generates less heat. However, a temperature rise relative to the input temperature for both flow rates is achieved. This is in agreement with the expectations, as the net heat generation is positive. Convective heat transfer can be observed: the temperature decreases in the diffusion layer.

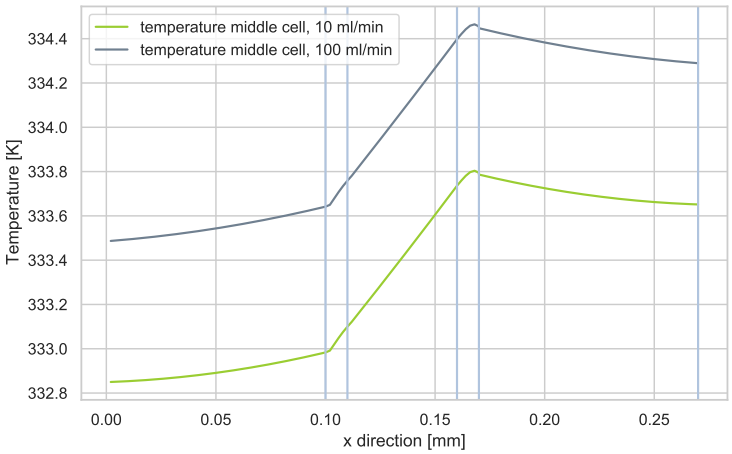

Figure 5.7: The 1D temperature distribution within the electrochemical cell for both flow rates. The y-direction is chosen at half the channel length. The grey line indicates the higher flow rate and the green line the lower flow rate. The difference between the two temperature profiles is approximately 1K.

The 2-dimensional temperature distribution of the MEA is divided in three parts. Figure 5.8 and Figure 5.9 show the temperature distribution within the different layers. Here, the results for the higher flow rate, 100 ml min^{-1} are shown in Figure 5.8 and for the lower flow rate, 10 ml min^{-1} in Figure 5.9. The boundaries are indicated with a white line. The top part represents the diffusion layer and the anodic catalyst layer. The middle part shows the temperature distribution within the membrane. Lastly, the bottom part represents the temperature distribution within the cathodic catalyst layer and diffusion layer.

First, the maximum temperature is important to look at. For a gas flow rate of 100 ml min^{-1}, the maximum temperature is ~334 K. The lower gas flow rate, 10 ml min^{-1}, results in a higher temperature: ~340 K. Moreover, the location of the maximum temperature for a higher flow rate is approximately at the middle of the cell in the y-direction. The hot-spot is located at the cathodic diffusion layer and catalyst layer. The maximum temperature is also located within the membrane. The lower flow rate achieves the maximum temperature at the inlet. Similarly, the cathodic diffusion layer and catalyst layer and membrane obtain the highest temperature.
The lowest temperature for 10 ml min^{-1} can be found at the outlet. At this location, the lowest current density is present as well. Within the anode at 10 ml min^{-1}, the temperature distribution shows resemblances with the current density distribution. As mentioned, the undeveloped temperature profile at the inlet, should result in a higher heat transfer coefficient. Note that for 100 ml min^{-1}, the minimum temperature is obtained close to the inlet. Nevertheless, the maximum current is also located at the inlet. A higher current should lead to more heat generation at the cathode. This finding suggests that more convective cooling takes place at the inlet for higher flow rates. This is in agreement with the expectations. Moreover, for both gas flow rates, the heat generation is distributed fully over the length of the cell in the x-direction. For lower flow rates, the temperature in the x-direction is more equally distributed than for higher flow rates.

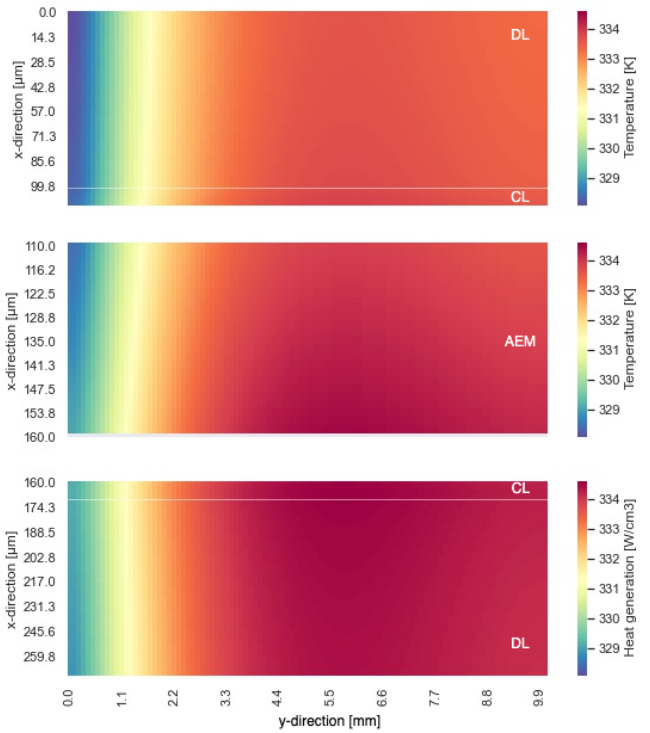

Figure 5.8: The 2-dimensional temperature distribution of the MEA geometry. The boundary between the layers is indicated with white lines. The distribution is shown for higher flow rates (100 ml min^{-1}). The x-direction's scale is in micrometers and the y-direction in millimeters. **Note that the legend for the temperature distributions differ for each figure.**

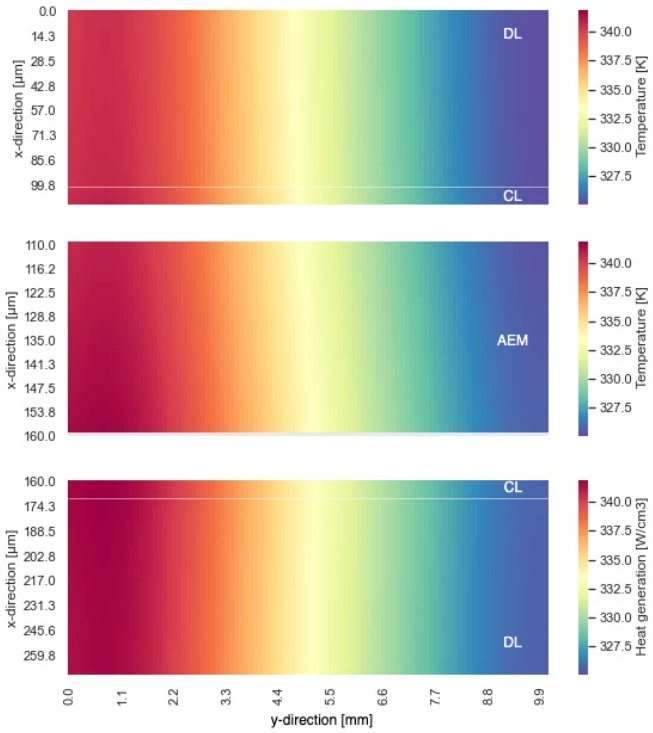

Figure 5.9: The 2-dimensional temperature distribution of the MEA geometry. The boundary between the layers is indicated with white lines. The distribution is shown for lower flow rates (10 ml min^{-1}). The x-direction's scale is in micrometers and the y-direction in millimeters. **Note that the legend for the temperature distributions differ for each figure.**

5.2.2. GDE temperature distribution

It can be observed that in the middle of the cell (y-direction), the same temperature profile is obtained. The maximum temperature appears to be the same for both flow rates. The value of the maximum temperature is close to 309 K. At the anodic diffusion layer, the lowest temperature can be observed. Between the catalyst layers, the temperature profile is approximately linear. At the diffusion layers, convective heat transfer can be seen, as the temperatures are slightly lower at the channel | DL boundary.

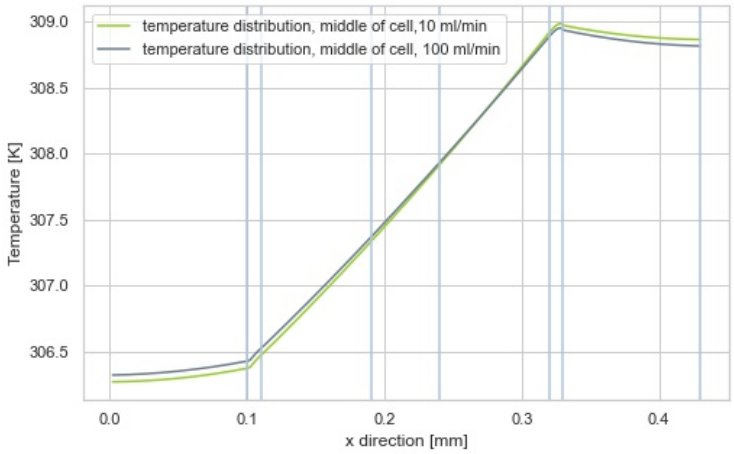

Figure 5.10: The 1D temperature distribution within the GDE electrochemical cell for both flow rates. The y-direction is chosen at half the channel length. The grey line indicates the higher flow rate and the green line the lower flow rate. The temperature profiles almost match quantitatively and qualitatively.

In Figure 5.11 and Figure 5.12 the temperature distribution is shown of the GDE geometry for both flow rates. Note that the legend differs for both figures. In Figure 5.12, the results for the higher flow rate are shown and in Figure 5.11 the results for the lower flow rate. The boundaries within the electrochemical cell are indicated with the white lines. Within the anode and cathode, the top and bottom parts of Figure 5.12, it can be observed that the temperature deviations are smaller in the y-direction, compared to the lower flow rate. Moreover, in the x-direction, it can be seen that the heat originated from the cathode does not reach the anode for higher flow rates. Quantitatively, a higher maximum temperature is achieved for a gas flow rate of 10 ml min^{-1} relatively to a gas flow rate of 100 ml min^{-1}. The maximum temperatures are 309 K and 312 K for 100 and 10 ml min^{-1}, respectively. The location of the hot-spots are more centered for 100 ml min^{-1} and at the inlet of the cell for 10 ml min^{-1}.

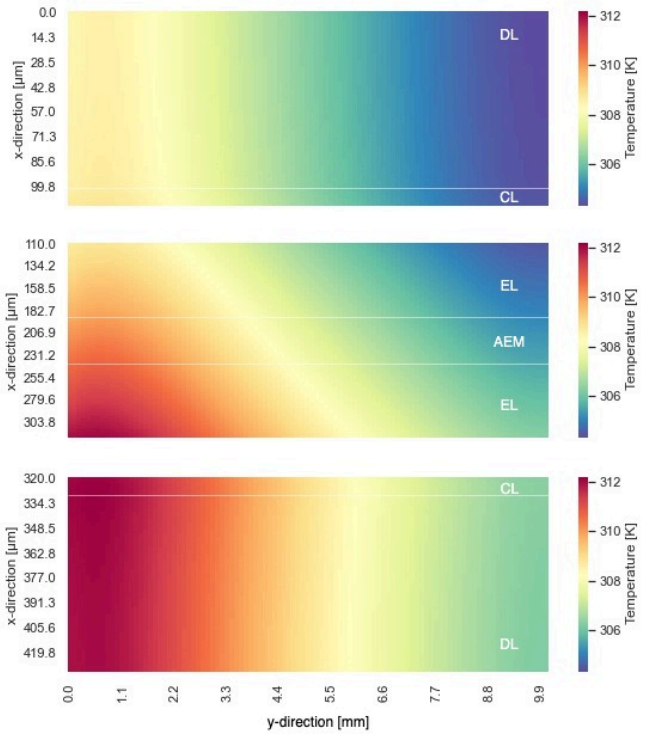

Figure 5.11: The 2-dimensional temperature distribution of the GDE geometry. The boundaries between the layers are indicated with white lines. The distribution is shown for lower flow rates (10 ml min^{-1}). The x-direction's scale is in micrometers and the y-direction in millimeters. **Note that the legend for the temperature distributions differ for each figure.**

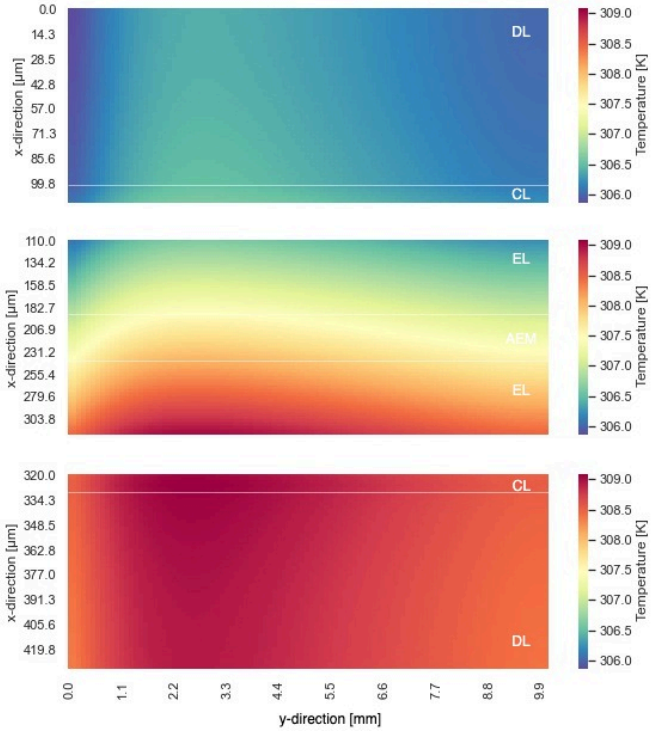

Figure 5.12: The 2-dimensional temperature distribution of the GDE geometry. The boundaries between the layers are indicated with white lines. The distribution is shown for higher flow rates (100 ml min^{-1}). The x-direction's scale is in micrometers and the y-direction in millimeters. **Note that the legend for the temperature distributions differ for each figure.**

5.2.3. Total temperature distribution

When comparing the geometries, it can be stated that higher temperatures are observed for the MEA geometry. Furthermore, when looking at the temperature distribution in the y-direction, the temperature is more evenly spread for the GDE. The locations of the hot-spots are similar for both the GDE and MEA for the different flow rates. For a GDE, the anode has a lower temperature relative to the cathode for both flow rates compared to the anode-cathode temperature difference of the MEA.

5.2.4. MEA heat distribution

The heat distribution within the electrochemical cell is determined by the summation of all source terms. As can be seen from Figure 5.13 and Figure 5.14, most heat is generated within the catalyst layers. For both flow rates, most of the heat can be observed at the cathodic catalyst layer. Here, most heat is located at the inlet. For a flow rate of 100 ml min^{-1}, the maximum generated heat within the cell is lower: the difference between the flow rates is $\sim$ 500 W cm^{-3}.

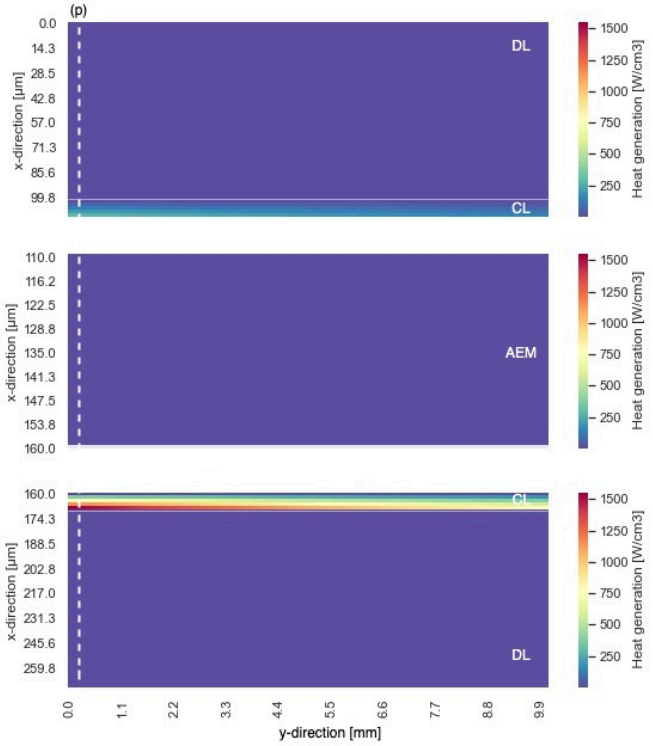

Figure 5.13: The 2D heat distribution within the MEA electrochemical cell for the flow rate of 10 ml min^{-1}. The different layers in the figure are shown, and the boundaries are indicated with white lines. The dotted line (p) in the y-direction shows the plane where most heat is generated. **Note that the legends are different for each figure.**

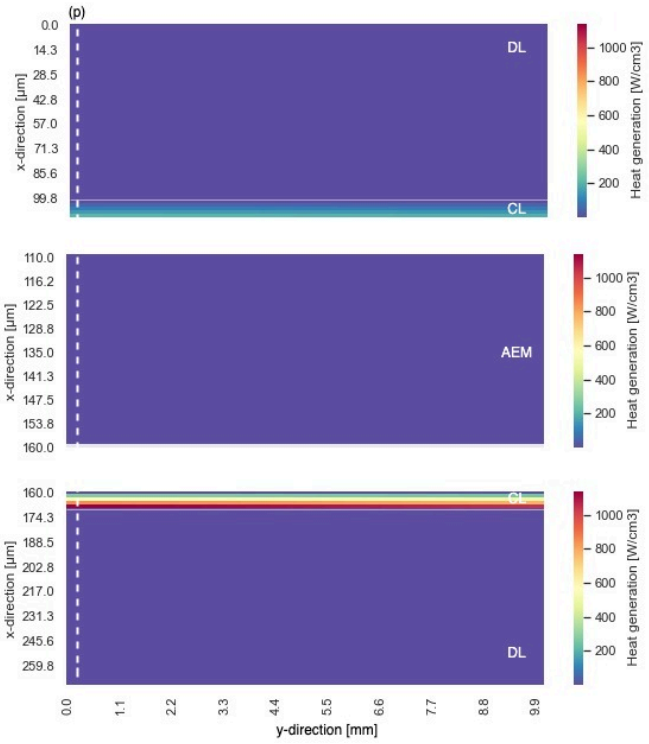

Figure 5.14: The 2D heat distribution within the MEA electrochemical cell for the flow rate of 100 ml min^{-1}. The different layers in the figure are shown, and the boundaries are indicated with white lines. The dotted line (p) in the y-direction shows the plane where most heat is generated. **Note that the legends are different for each figure.**

5.2.5. MEA heat generation

As previously discussed, most heat in a MEA is located at the inlet within the catalyst layers. The heat generation within the catalyst layers is a summation of the reversible heating, irreversible heating and joule heating. The contribution of each of these heat sources is shown in Figure 5.15 and Figure 5.16, for the anodic and cathodic catalyst layers at the inlet, respectively. The location is also shown with the dotted line in Figure 5.13 and Figure 5.14, indicated with the letter (p). On the left, the results for 100 ml min^{-1} can be found and on the right, the results for 10 ml min^{-1} can be found. As stated, the anode needs energy to operate at thermoneutral conditions. This can be seen in Figure 5.15, as the reversible heat is negative. At a lower flow rate, more heat is required, as the reversible heat is more negative. Similarly, more irreversible heating can be observed at lower flow rates. For both flow rates, the reversible heating is the biggest contributor to the total heat generation at the specific catalyst layer. The joule heating due to electric and ionic ohmic losses are very small. In section A.7, the graphs are more zoomed in on the joule heating in the anode.

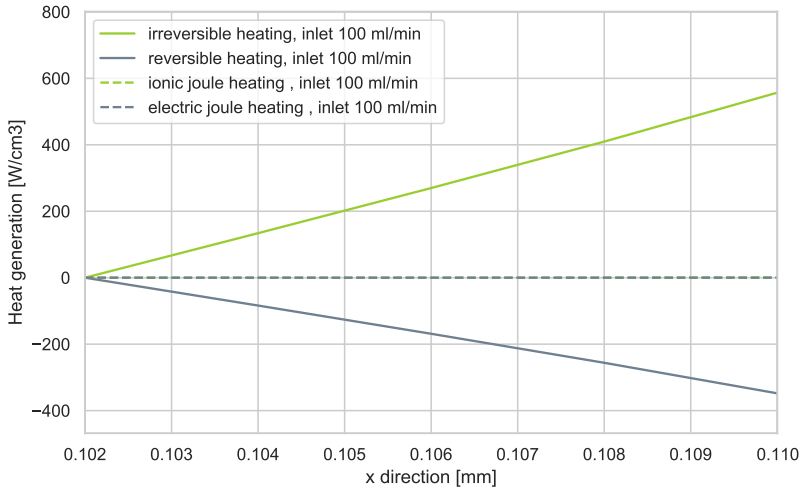

(a) 100 ml min^{-1}

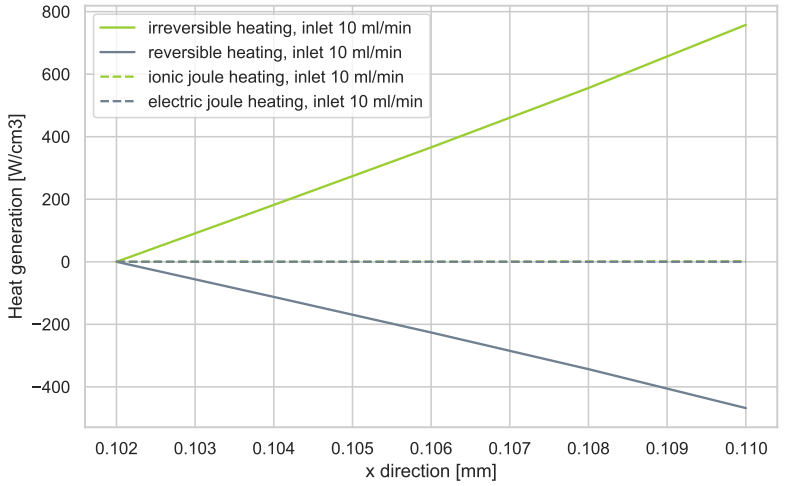

(b) 10 ml min^{-1}

Figure 5.15: The heat generation within the anodic catalyst layer for the MEA geometry. The reversible, irreversible and joule heatings are considered. The biggest contributor are the irreversible losses, which generate heat. The reversible losses are negative, and require heat from the system. The ohmic losses are very small compared to the other losses

The cathode has a higher thermoneutral potential than the equilibrium potential, so both reversible as irreversible losses are heat sources. Similar to the anode, more heat is generated at the inlet for lower flow rates. Compared to the heat sink at the anode, more heat is generated by reversible heating than required. The net heat generation is positive, so a temperature rise is expected. Again, joule heating is negligible.

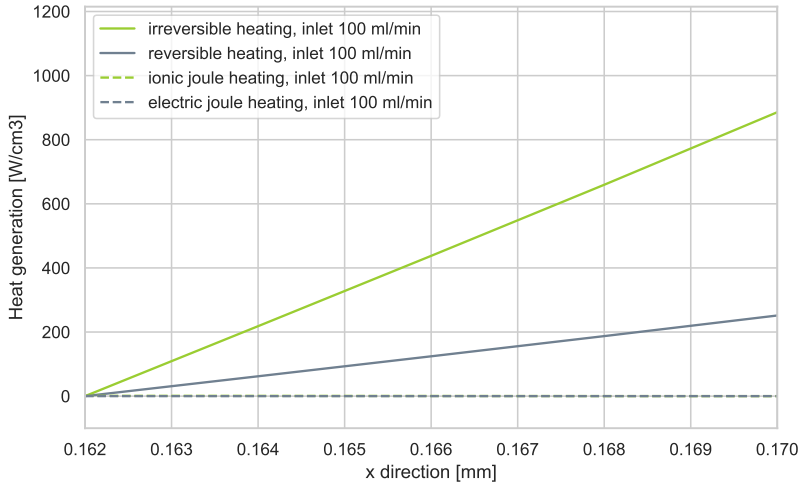

(a) 100 ml min^{-1}

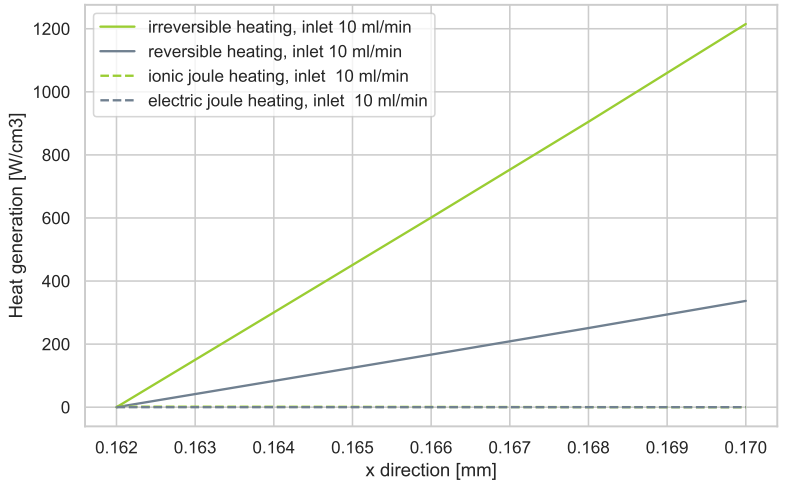

(b) 10 ml min^{-1}

Figure 5.16: The heat generation within the cathodic catalyst layer for the MEA geometry. The reversible, irreversible and joule heatings are considered. The biggest contributor are the irreversible losses, which generate heat. The reversible losses are also positive, and even more heat is generated within the cell. The ohmic losses are negligibly small compared to the other losses

5.2.6. GDE heat distribution

The 2D heat distribution within the GDE geometry is demonstrated in Figure 5.17 and Figure 5.18. Similar to the MEA geometry, most heat is generated within the catalyst layers. Again, the maximum heat generation is located at the inlet, indicated with the dotted line (p). In the other parts, only ohmic losses occur. The joule heating in these parts, that is caused by the ohmic losses, is relatively low compared to the heat generation in the catalyst layers.

5.2.7. GDE heat generation

In Figure 5.19 and Figure 5.20, the heat generation within the anodic and cathodic catalyst layers at the inlet are shown, respectively. This is indicated with the dotted line (p) in Figure 5.17 and Figure 5.18. At the anode, the reversible heat is negative. This is a result of the lower equilibirum potential relative to the thermal neutral potential. At a lower flow rate, a higher heat sink can be observed. Moreover, more irreversible heating can be observed at lower flow rates as well. For both flow rates, the irreversible heat is higher than the reversible heat. As a consequence, the net heat generation is positive and

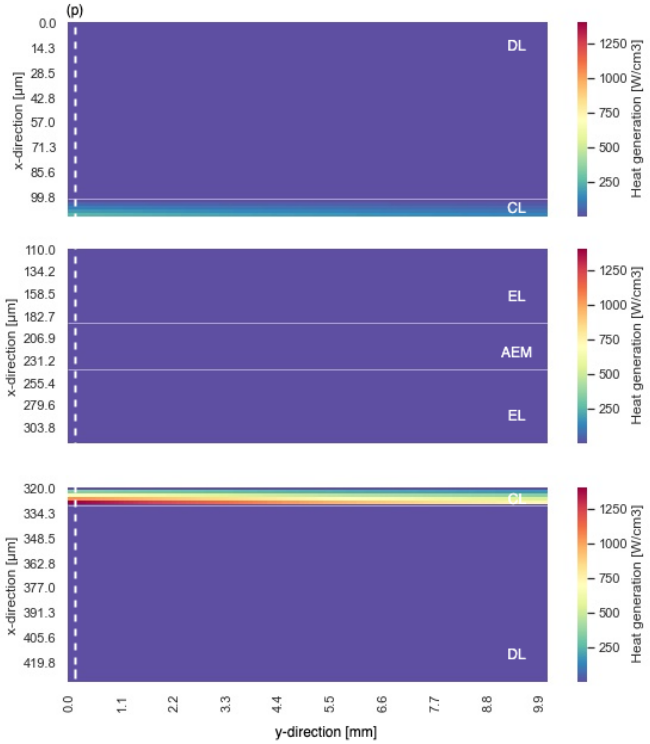

Figure 5.17: The 2D heat distribution within the GDE electrochemical cell for the flow rate of 10 ml min^{-1}. The different layers in the figure are shown, and the boundaries are indicated with white lines. The dotted line (p) in the y-direction shows the plane where most heat is generated. **Note that the legends are different for each figure.**

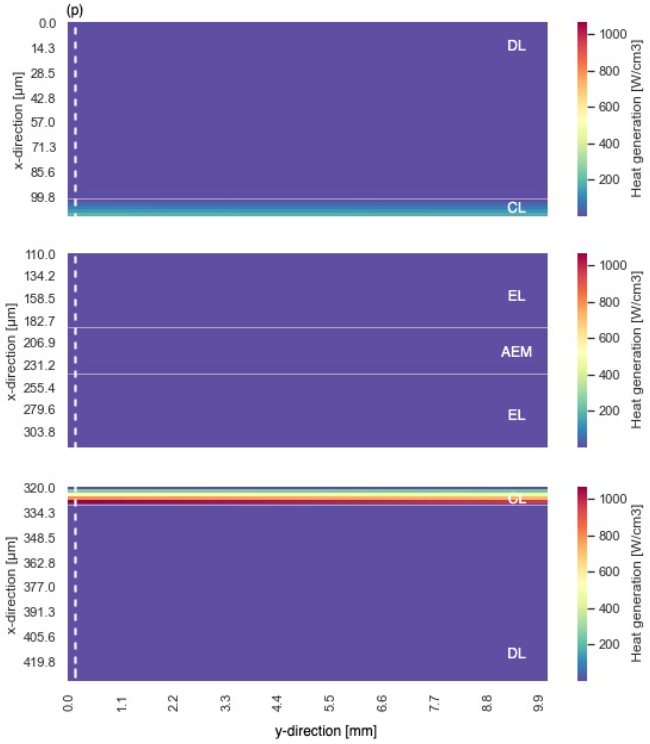

Figure 5.18: The 2D heat distribution within the GDE electrochemical cell for the flow rate of 100 ml min^{-1}. The different layers in the figure are shown, and the boundaries are indicated with white lines. The dotted line (p) in the y-direction shows the plane where most heat is generated. **Note that the legends are different for each figure.**

the temperature will rise in the anode. This also concludes that the irreversible heating is the biggest contributor in the anode. The joule heating due to ohmic losses are very small. In section A.7, the graph is more zoomed in on the joule heating in the anode.

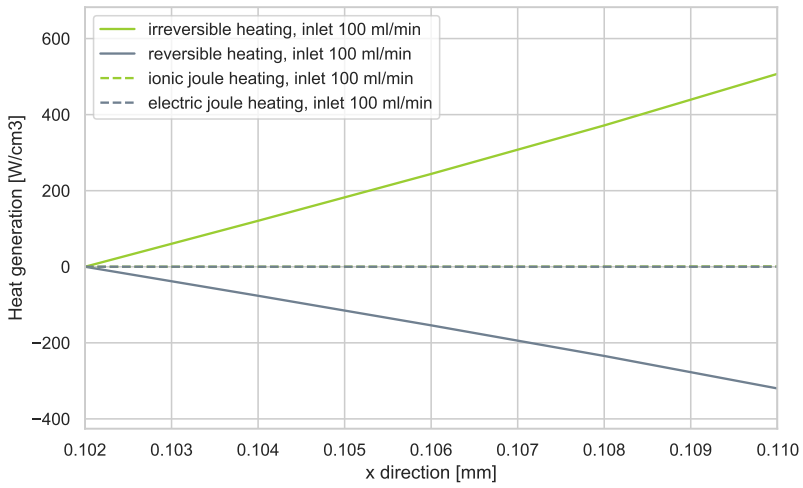

(a) 100 ml min^{-1}

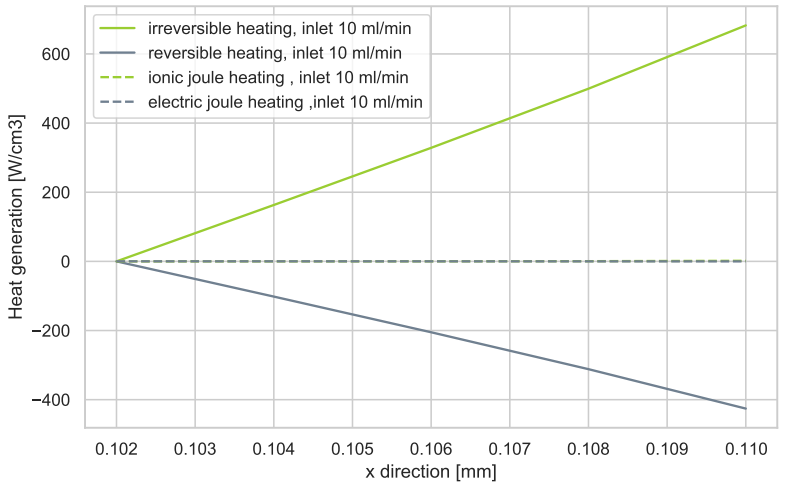

(b) 10 ml min^{-1}

Figure 5.19: The heat generation within the anodic catalyst layer for the GDE geometry. The reversible, irreversible and joule heatings are considered. The biggest contributor are the irreversible losses, which generate heat. The reversible losses are negative, and require heat from the system. The ohmic losses are very small compared to the other losses.

At the cathode catalyst layer, both reversible heating as irreversible heating are positive. Again, joule heating is negligibly small compared to reversible and irreversible heating. At higher flow rates, both reversible heating as irreversible heating are lower. Compared to the anode, the irreversible losses are higher in the cathode. This suggests that more heat is expected in the cathode. This statement is in agreement with the temperature results discussed earlier.

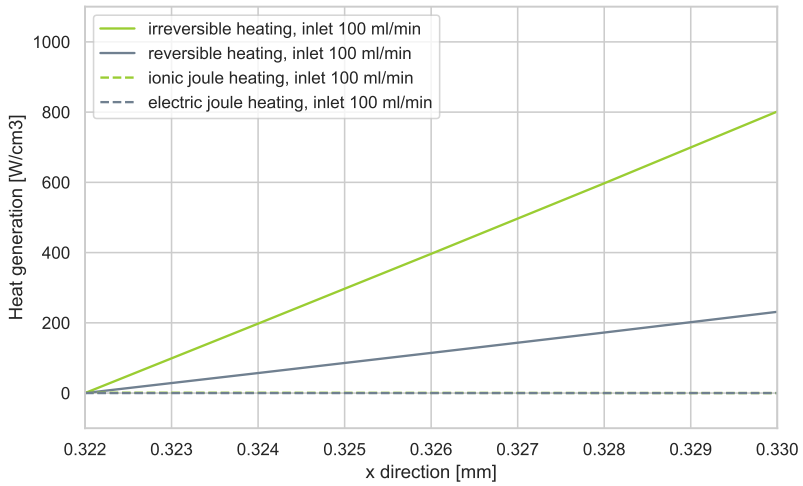

(a) 100 ml min^{-1}

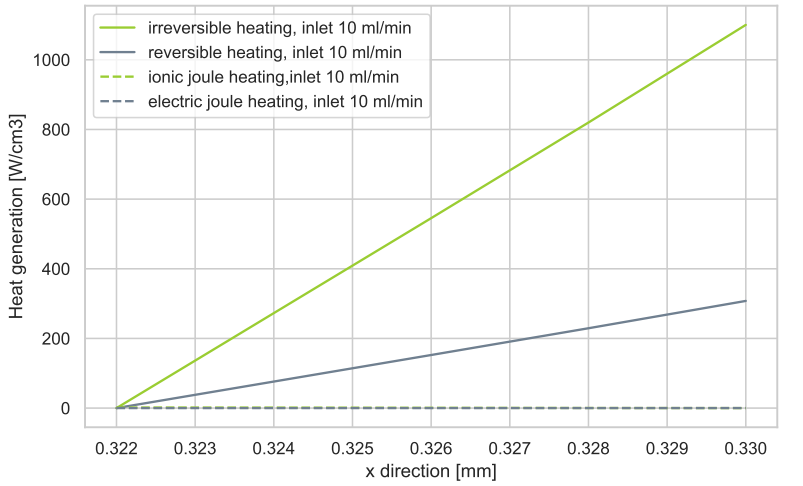

(b) 10 ml min^{-1}

Figure 5.20: The heat generation within the cathodic catalyst layer for the GDE geometry. The reversible, irreversible and joule heatings are considered. The biggest contributor are the irreversible losses, which generate heat. The reversible losses are also positive, and even more heat is generated within the cell. The ohmic losses are negligibly small compared to the other losses.

5.2.8. Total heat generation

Looking at the cathodic heat generation for both geometries, it can be stated that at the inlet more heat is generated by irreversible losses in the MEA. The same is true for the anodic heat generation. The difference is approximately 200 W cm^{-3}. The reversible losses are similar for both geometries. This is in agreement with the difference in temperature distribution as the MEA obtains higher temperatures.

5.3. Sensitivity analysis

Within this research, assumptions are made in order to keep the focus on the heat generation. Since carbon dioxide electrolysis is fairly new, some parameters are estimated, which cause uncertainties in the results. The concentration at the anode and the thermal conductivity are the parameters that are analysed in further detail. The sensitivity analysis is only done for the MEA geometry with a volumetric gas flow rate of 10 ml min^{-1} and one adjustment per analysis. This is done considering the large

computational time. It is assumed to have similar effects for the other geometry and flow rates.

- The concentration of oxygen is not calculated in detail, but approximated by looking at the mol ratio. To know how much influence the concentration of oxygen has, the cell will also operate with no concentration losses at the anode. Hereafter, the results will be compared to the outcomes of the model. It is expected that this will affect the overpotentials within the anodic catalyst layer and thus the temperature rise within the anodic catalyst layer.
- The thermal conductivity of the catalyst layer can have a significant influence on the total heat generation [15]. As this value is estimated, it is important to ascertain how much the deviation in heat generation is. The conductivity will be decreased to k=0.1 $Wm^{-1}K^{-1}$. Then, the temperature at the cathodic catalyst layers will be discussed at steady state. The biggest effect is assumed to be seen in the temperature distribution and the maximum temperature within the cathodic catalyst layer.

5.3.1. Influence of concentration O_2 MEA

In Figure 5.21 the temperature plots in the x-plane are shown in the middle of the cell (y-direction). The grey line shows the results of the sensitivity output and the green line shows the results of the output of the model. The graph demonstrates that the temperature matches in the cathodic catalyst layer and diffusion layer. However, a temperature deviation can be seen at the anodic catalyst layer and diffusion layer. The difference is less than 0.2 K. Another thing to take into account, is that the temperature profiles do not match within the anodic catalyst layer.

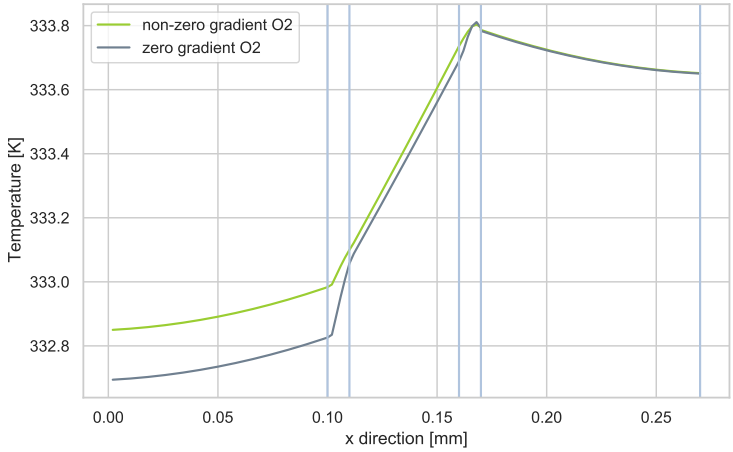

Figure 5.21: The 1D temperature profile for the MEA geometry at the middle of the cell in the x-direction. The results for the model and sensitivity analysis are both plotted. A difference can be seen in the anodic catalyst layer and the temperature in the anode. The electrochemical cell's temperature profile in the other parts do match.

For the activation overpotential, a decrease can be observed in Figure 5.22 for the sensitivity analysis results. This means that less heat generation is expected, which is in agreement with the temperature profile. Both the outcome of the model as the outcome of the sensitivity analysis have similar profiles.

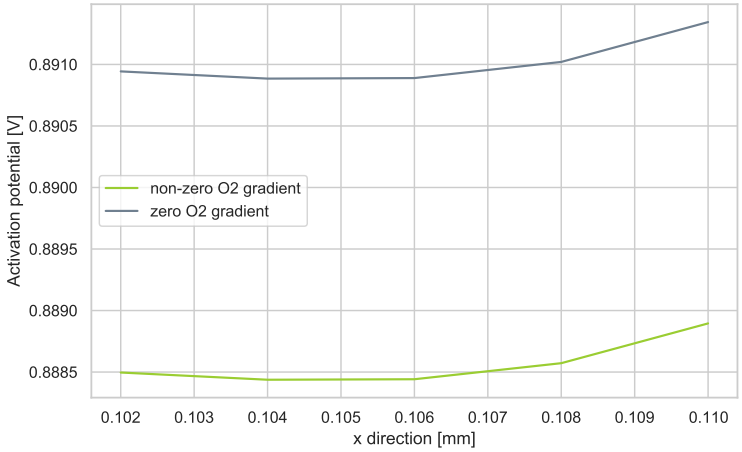

Figure 5.22: The activation overpotential is plotted against the x-direction within the MEA electrochemical cell. Both the results for the model as the sensitivity analysis are demonstrated. Lower values for the sensitivity analysis are obtained, where the concentration gradient within the electrochemical cell is neglected.

It is proven by the sensitivity analysis that the oxygen concentration does have an impact on the temperature distribution. To obtain a realistic temperature profile, it is necessary to calculate the oxygen concentration more accurately. However, as the maximum temperature difference is below 0.2 K, the influence of the oxygen concentration on the heat generation is not that large.

5.3.2. Influence of thermal conductivity MEA

The value of the thermal conductivity represents how well the heat is conducted in the material. Lower thermal conductivities indicate that less heat is conducted. This will result in higher temperatures in the material. For this reason, the thermal conductivity is a very important parameter. To know how big the effect is, the results are compared for different thermal conductivities. The values that are examined are k= 0.21, the value used in the research and k= 0.1 for the sensitivity analysis.
Figure 5.23 demonstrates the temperature profiles that are obtained from the model using two different thermal conductivities for the catalyst layers. The results support the assumption that the material conducts less heat, causing higher temperatures. The difference is approximately 4K. In a full electrolyzer stack, a difference of 4K for each individual cell can have a large impact. Hence, an uncertainty of the thermal conductivity of the catalyst layers is undesired.

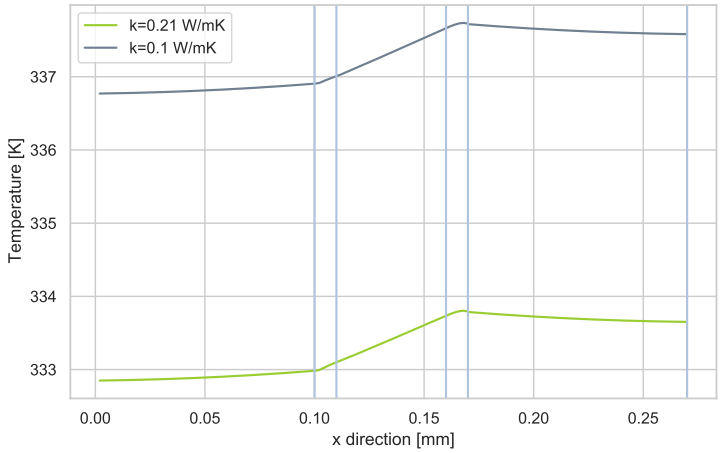

Figure 5.23: The 1D temperature profile for the MEA geometry at the middle of the cell in the x-direction. The results for the model and conductivity sensitivity analysis are both plotted. The electrochemical cell's temperature profile match. However, higher temperatures are achieved for the sensitivty analysis.

Overall, the membrane is assumed to be the most sensitive to high temperatures. Hence, the effect of both the concentration as the thermal conductivity on the membrane's temperature is important to take into account. In Figure 5.24, the temperature in the y-direction is shown at the centre of the membrane. The profiles of the concentration sensitivity analysis and the developed model are almost identical. As expected, the temperature is higher for the modeling outcome when a lower thermal conductivity is employed.

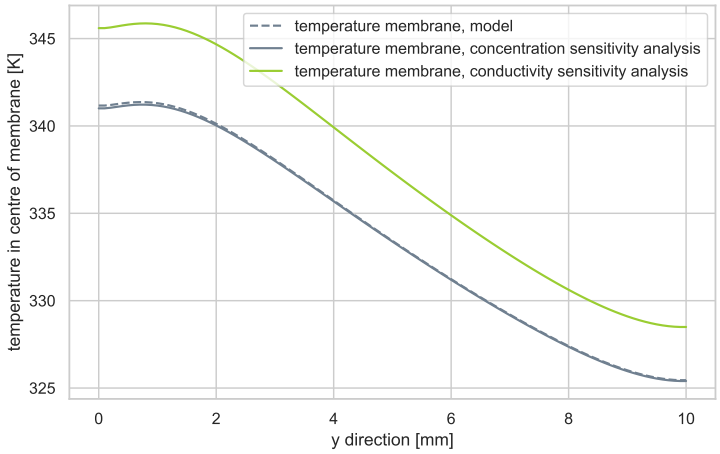

Figure 5.24: The 1D temperature profile for the MEA geometry at the middle of the membrane in the y-direction. The results for the model and sensitivity analyses are plotted. The temperature profiles match for the concentration sensitivity analysis and the outcome of the model. Higher temperatures are obtained for the conductivity analysis.

To summarize, the thermal conductivity plays a very important role in electrolysis modeling. Decreasing the thermal conductivity by 0.1 results in a temperature increase of 4 K, according to the modeling outcome. The concentration of the anode has an influence on the temperature profile in the anode, but does not influence the temperature profile in the membrane.

6 Discussion

Both geometries are studied for two different flow rates: 10 ml min^{-1} and 100 ml min^{-1}. The relevant results of the electrochemical and thermal are shown. In this chapter, these results will be discussed in order to answer the research questions.

6.1. Current density

The current density distribution is a function of the concentration in the y-direction. As the length of the channel does not differ, the current distribution is the same for both geometries. However, it does differ for alternating volumetric flow rates. Lower flow rates result in a better current distribution: smaller deviations from the mean current density and evenly distributed at the inlet and outlet. This can be explained by the concentration profile, that is more linear for lower flow rates. Note that the actual value of concentration does not matter. Nonetheless, the slope of the concentration profile does have an influence on the current density distribution. A small concentration deviation from the mean concentration is desirable. Larger deviations result in higher currents, which cause more temperature increase.

The data suggest that a higher flow rate would be more beneficial, as it gives a more evenly distributed current density.

6.2. Potential

The activation overpotential includes the diffusion losses. As expected, the needed overpotential increases at lower concentrations. Furthermore, the Butler-Volmer equation suggests that with higher temperatures, more activation energy is required from the system to obtain the same current density. The expected overpotential at the anode was ~ 0.75 V at 298 K. From Figure 5.3, it can be seen that the overpotential is raised with increasing temperature. Similar, for the GDE, Figure 5.5, a higher activation overpotential can be observed as the obtained temperature is also higher than the input temperature. Comparing the GDE and MEA at the cathode suggest that more overpotential is required for the reaction for the MEA for both flow rates. This is in agreement with the Butler Volmer equation. The Butler Volmer equation suggest that at higher temperatures, more overpotential is needed to obtain the same current density. Moreover, looking at Figure 4.12, the difference between the thermoneutral and equilibrium potential grows with increasing temperatures. This indicates that more potential is needed at higher temperatures.

The GDE is the most desirable geometry as it requires lower overpotentials for the reaction on both the anode as the cathode to obtain the same current density.

6.3. Heat generation

From the results, it became clear that the irreversible losses are dominant in the anode for both geometries and volumetric flow rates. Although the (negative) reversible heating can compensate for a

small part of these losses, one could say that the irreversible losses should be decreased in order to have zero heat generation. Lower flow rates generate more heat at the inlet. The MEA generates more heat by irreversible losses than the GDE at the inlet. The reversible losses are comparable.
At the cathode side, the irreversible losses are most dominant for both geometries and flow rates. Again, lower flow rates generate more heat at the inlet. This can be explained by the higher current density at the inlet. The cathodic heat generation of the MEA are higher relative to the heat generation of the GDE.

It can be concluded that higher flow rates are more favourable when less heat generation is desired at the anode and cathode. Also, less heat generation is expected in a GDE geometry. The GDE is favourable compared to the MEA regarding irreversible losses at the anode and cathode.

6.4. Heat distribution

As the reversible losses are negative in the anode, heat is required from the system. Also, less heat is generated by irreversible losses in the anode as well, compared to the cathode. In the cathode, both reversible as irreversible losses are positive. As a result, there is a less heat generation and thus a lower temperature in the anode than in the cathode. The hot-spot in the x-direction is located in the cathode. This is true for both geometries and both volumetric flow rates.
Furthermore, for the GDE geometry, the cell is continuously cooled by the electrolyte. Consequently, the heat is more evenly distributed in the flow direction (y-direction). Looking at the different flow rates for a GDE geometry, a greater maximum temperature can be observed at lower flow rates: ∼312 K compared to ∼309 K. The GDE at 100 ml min^{-1} does have a very small temperature deviation at the cathodic catalyst and diffusion layer, but it can be stated that the temperature is evenly distributed in the y-direction. The GDE at 10 ml min^{-1} has a hot-spot at the inlet of the cathode.
For a MEA, the temperature distribution for 100 ml min^{-1} also differs from 10 ml min^{-1}. A higher maximum temperature can be obtained at lower gas flow rates (∼340 K) than for higher gas flow rates (∼334 K). Moreover, the highest temperature for higher flow rates can be obtained in the middle of the cell in the y-direction. The inlet has lower temperatures, which is caused by convective cooling. On the other hand, the maximum temperature for lower gas flow rates is obtained at the inlet of the cell. It can be stated that less cooling takes place at lower gas flow rates.
Compared to a MEA, the temperature in a GDE is better distributed and less heat is generated. The temperature increase is also significantly lower compared to the MEA. The hot-spot is moved to the center of the cell (y-direction) for higher flow rates and located at the inlet for lower flow rates for both geometries. This is caused by convective heat transfer. For both geometries at lower flow rates, the heat is penetrated to the membrane, causing the membrane to heat up as well.

A GDE is more favourable with respect to hot spot formation, as lower maximum temperatures are achieved. It is expected that less damage is done on the membrane caused by heat for a GDE geometry as the hot-spot is not located at the membrane. At higher flow rates, less heat is generated and it is better distributed.

7

Conclusion

This thesis aimed to identify the heat generation within carbon dioxide electrolysis for different geometries. The observed geometries are the membrane electrode assembly (MEA) and the gas diffusion electrode (GDE). Based on the results, that are qualitatively and quantitatively analysed, the research question and its subquestions can be answered. The main research question and its subquestions were formulated as follows:

What is the heat generation and distribution within a CO_2 electrolysis system for different geometries?

- What is the local heat generation inside the electrochemical cell and how can it be quantified?
- Which factors contributes the most to heat generation and distribution?
- What is the effect the gas flow rate on the heat generation and distribution?
- What is the effect of electrolyte of the heat distribution in the cell?
- What is the most optimal configuration for CO_2 electrolysis with respect to heat management?

From the analysis, it can be concluded that most heat is generated within a MEA geometry. Since the electrolyte cools down the electrodes, the maximum temperature increase of the GDE geometry is 9 K and 12 K for 10 and 100 ml min^{-1} respectively. For the MEA geometry, a temperature increase can be expected of 36 K and 42 K for 10 and 100 ml min^{-1} respectively. The temperature difference between the electrodes is expected to be higher for a GDE, due to the added electrolyte. For a GDE geometry, the hot-spot is not located within the membrane, whereas for a MEA, the membrane also heats up significantly.
The biggest contributor to the heat generation are the irreversible losses within the cathodic and anodic catalyst layer: the activation overpotentials for carbon dioxide reduction are relatively high compared to the equilibrium potentials. Moreover, the ionic and electric ohmic losses are small.

In addition, higher flow rates result in a decrease in temperature at the inlet for both geometries. For the GDE geometry, the temperature distribution is also better for higher flow rates. The model shows that a maximum temperature can be expected for higher flow rates compared to lower flow rates.

The MEA differs from the GDE as the GDE has additional electrolyte layers. The electrolyte causes a better temperature distribution. The electrolyte also ensures that the increase in temperature stays relatively small compared to the MEA. Furthermore, the additional electrolyte layer prevents that the hot-spot is located within the membrane.

Given the above, the GDE has proved to cause a lower overall temperature rise. Temperature sensible components, like the membrane, are less impacted by the heat generation of the cathode compared to the MEA geometry. As described, for the same desired current density, less potential is needed. It can

be concluded that the GDE is more beneficial for carbon dioxide electrolysis for the given operating conditions. For a GDE geometry, operating with a gas flow rate of 100 ml min^{-1} can result in a lower temperature increase compared to 10 ml min^{-1}.

8

Recommendations

The scope of this research was to get insight of the heat generation and distribution within carbon dioxide electrolysis systems. To ensure that the research could be done in the given time, assumptions had to be made. Also, as not much research has been devoted to carbon dioxide electrolysis, more research is yet to be done. Based on this research, some recommendations for upcoming experiments and modeling studies are listed below.

8.1. Experiments

Focus on lowering the activation overpotential

From the results, it can be concluded that the irreversible losses are the biggest contributor to the total heat generation. The irreversible losses are caused by the activation overpotential. The activation overpotential is dependent on the chosen catalyst layer and operation conditions. In order to decrease the heat generation within the electrochemical cell, more research has to be devoted to the catalyst layer.

Volumetric Gas flow rate

The volumetric gas flow rate also proved to have a significant influence on the heat distribution within the electrochemical cell. The gas flow rate has an influence on the current distribution. More knowledge on the influence of the gas flow rate on the current distribution can help in order to obtain an equally distributed current density.

8.2. Modeling

More detailed concentration model

When looking at the sensitivity analysis, it can be concluded that the concentration in the x-direction is important to obtain the correct temperature profile. As the current density is also a function of the concentration in the y-direction, the concentration model has shown to be a very important aspect to investigate the heat generation and distribution within the electrochemical cell. For this research, it is assumed that the concentration decrease in the gas channel is limited by mass transfer. A better developed concentration model can be very useful to investigate the heat generation and distribution in further detail. Also the concentration at the anode can be looked at. Gas channel sizes can also be alternated. Another assumption that is made, is that the diffusion coefficient does not decrease much. However, carbon dioxide dissolves very poorly in water. This is also an interesting aspect to look at.

Larger scale

Another recommendation is to analyse the heat generation for larger cells in order to implement carbon dioxide electrolysis at industrial scale. Larger cells can cause larger current deviations. Also, at larger scale, the cell operates at higher currents. Higher currents cause more heat generation, so this is important to investigate as well. At larger scales and in electrolyzer stacks, it could also be interested to

look at the recycling of the generated heat.

Including separate microporous layer
In this research, the diffusion layer is not separated in a macroporous and microporous layer. A porous electrode, however, does have separate layers. These layers differ from porosity and ionic and electric conductivity. This can have an impact on the heat generation and the concentration profile. A more detailed research should include both layers separately.

Materials
For now, only temperature dependent ionic conductivity of the membrane is considered. For further research, temperature dependent properties of other materials can also be included within the models. Still a lot of research on carbon dioxide electrolysis is yet to be done. Therefore, multiple studies differ on the choice of materials for the catalyst layers. This can have a significant impact on the reaction kinetics and thus the heat generation. A research devoted to different materials used in literature can be very useful.

Electrolyte
The electrolyte has shown to be very useful to obtain a good temperature distribution and lowering the maximum temperature. In reality, the electrolyte can have different configurations and the electrolyte can be re-used in the system. Other electrolyte solutions can also be investigated.

Appendix A

A.1. Calculations Standard Gibbs Free Energy at Standard Reference Conditions

Species	ΔG_f [10^3 J mol^{-1}]
CO_2	-394.39
H_2O	-237.14
CO	-137.16
OH^-	-157.2
O_2	0

Table A.1: Gibbs free energy values for the relevant compounds for carbon dioxide electrolysis

$$\mathrm{CO_2 + H_2O + 2\,e^- \longrightarrow CO + 2\,OH^-} \tag{A.1}$$

$$\begin{aligned}\Delta G_r &= \Delta G_{f,prod} - \Delta G_{f,reac} \\ &= (-137.16 + 2 \cdot -157.2) - (-394.39 + -237.14) \\ &= (-451.56) - (-631.53) \\ &= 179.97\end{aligned} \tag{A.2}$$

$$\mathrm{2\,OH^- \longrightarrow \frac{1}{2}O_2 + H_2O + 2\,e^-} \tag{A.3}$$

$$\begin{aligned}\Delta G_r &= \Delta G_{f,prod} - \Delta G_{f,reac} \\ &= (0 + -237.14) - (2 \cdot -157.2) \\ &= (-237.14) - (-314.4) \\ &= 77.26\end{aligned} \tag{A.4}$$

A.2. Calculations Standard Enthalpy at Standard Reference Conditions

species	ΔH_f [10^3 J mol^{-1}]
CO_2	−393.5
H_2O	−285.8
CO	−110.5
OH^-	−229.9
O_2	0

Table A.2: Enthalpy values for the relevant compounds for carbon dioxide electrolysis

$$\mathrm{CO_2 + H_2O + 2\,e^- \longrightarrow CO + 2\,OH^-} \tag{A.5}$$

$$\begin{aligned}\Delta H_r &= \Delta H_{f,prod} - \Delta H_{f,reac} \\ &= (-110.5 + 2 \cdot -229.9) - (-393.5 + -285.8) \\ &= (-570.3) - (-679.3) \\ &= 109.3\end{aligned} \tag{A.6}$$

$$\mathrm{2\,OH^- \longrightarrow \frac{1}{2}O_2 + H_2O + 2\,e^-} \tag{A.7}$$

$$\begin{aligned}\Delta H_r &= \Delta H_{f,prod} - \Delta H_{f,reac} \\ &= (0 + -285.8) - (2 \cdot -229.9) \\ &= (-285.8) - (-459.8) \\ &= 174\end{aligned} \tag{A.8}$$

A.3. Temperature Dependence of Enthalpy, Entropy and Gibbs Free Energy

For the calculation, the Shomate equation is used to approximate the Enthalpy and Entropy of all compounds [58] to determine its values at the relevant temperature. The Shomate relation for enthalpy and entropy is as follows:

$$\Delta H_{0,T} - \Delta H_{0,ref} = At + Bt^2/2 + Ct^3/3 + Dt^4/4 - E/t + F - \Delta H_{0,ref}, \tag{A.9}$$

$$\Delta S_{0,T} = A\ln(t) + Bt + Ct^2/2 + Dt^3/3 + Dt^4/4 - E/(2 * t^2) + G, \tag{A.10}$$

where t= *T*/1000. Both the equations as the parameters for each compound can be found at the Webbook of the National Institute of Standards and Technology (NIST), where thermophysical properties of fluid systems are documented. The difference in enthalpy, entropy and Gibbs are plotted in Figure A.1,Figure A.2 and Figure A.3 for the relevant compounds. There are no values found for hydroxide-ions. Since the mol ratio is 2:2, it does influence the potential of the half reaction, but not the cell potential. Therefore, the hydroxide-ion enthalpy, entropy and Gibbs free energy is considered to be constant.

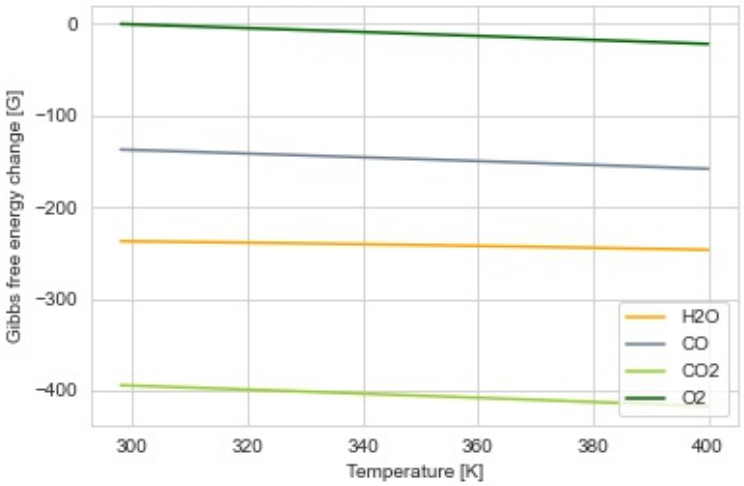

Figure A.1: Calculated Gibbs free energy values for different temperatures, using Maxwell equations and the Shomate equation.

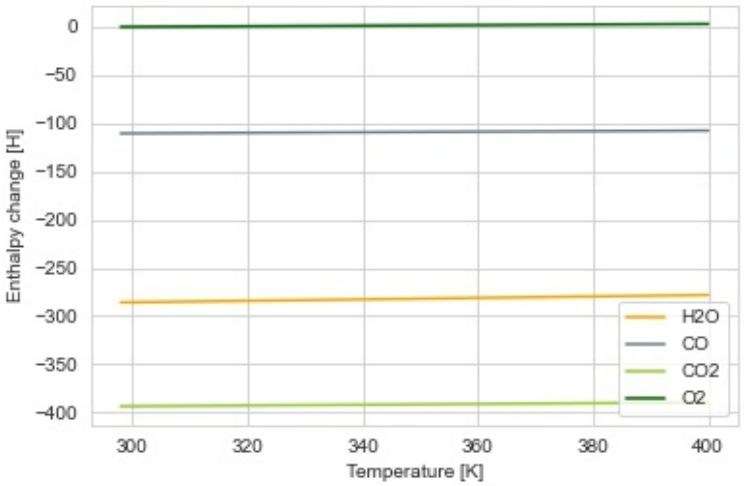

Figure A.2: Calculated enthalpy values for different temperatures, using the Shomate equation.

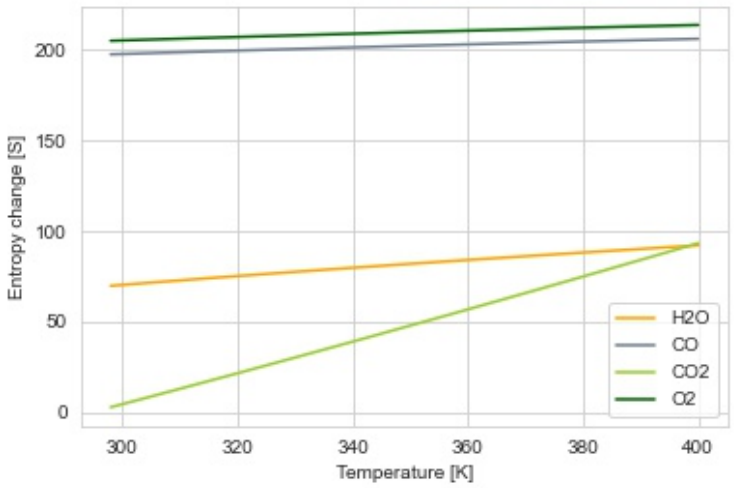

Figure A.3: Calculated entropy values for different temperatures, using the Shomate equation.

A.4. Polyfit Ionic Conductivity Sustainion

The data is obtained from experiments done by Dioxide Materials on anion exchange membranes, including Sustainion [25]. In Python, a curve is fitted on the data, resulting in a first-degree polynomial equation.

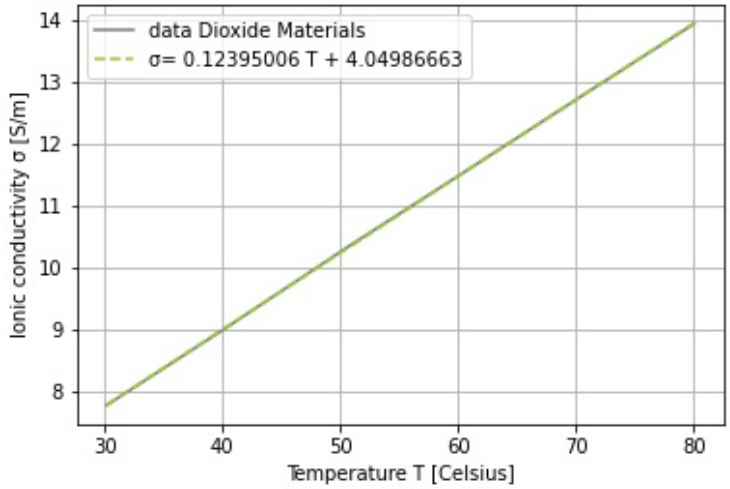

Figure A.4: A plot of the data obtained from the experiments done by Dioxide Materials [25] and the made polyfit in Python 3.

A.5. Literature review

Authors	Feedstock	Type	Electrochemical model	Thermal model	Reference
Marangio et al.	Hydrogen	Fuel cell	1	x	[61]
Ni et al.	Hydrogen	Fuel cell	1	x	[68]
Khalid et al.	Hydrogen	Fuel cell	1	x	[48]
Busquet et al.	Hydrogen	Fuel cell	1	1	[16]
Onda et al.	Hydrogen	Fuel cell	1	2	[73]
Burheim et al.	Hydrogen	Fuel cell	x	2	[15]
Wang et al.	Hydrogen	Fuel cell	2	x	[88]
Cheddie et al.	Hydrogen	Fuel cell	2	x	[18]
Wang et al.	Hydrogen	Fuel cell	2	1	[87]
Meng et al.	Hydrogen	Fuel cell	2	2	[63]
Secanell et al.	Hydrogen	Fuel cell	2	2	[80]
Secanell et al.	Hydrogen	Fuel cell	2	2	[1]
Al-Baghdadi et al.	Hydrogen	Fuel cell	2	2	[5]
Cetinbas et al.	Hydrogen	Fuel cell	2	2	[17]
Wu et al.	Hydrogen	Fuel cell	2	2	[93]
Abdul Rasheed et al.	Hydrogen	Fuel cell	2	2	[2]
Wang et al.	Hydrogen	Fuel cell	2	2	[90]
Siegel et al.	Hydrogen	Fuel cell	review	review	[81]
Falcão et al.	Hydrogen	Electrolyzer	1	x	[28]
Han et al.	Hydrogen	Electrolyzer	1	x	[39]
García-Valverde et al.	Hydrogen	Electrolyzer	1	1	[33]
Hammoudi et al.	Hydrogen	Electrolyzer	1	1	[38]
Agbli et al.	Hydrogen	Electrolyzer	1	1	[3]
Diéguez et al.	Hydrogen	Electrolyzer	1	1	[23]
Zhao et al.	Hydrogen	Electrolyzer	1	2	[98]
Lebbal et al.	Hydrogen	Electrolyzer	1	2	[55]
Kim et al.	Hydrogen	Electrolyzer	1	2	[50]
Zhang et al.	Hydrogen	Electrolyzer	2	2	[97]
Olivier et al.	Hydrogen	review	review	review	[72]
Xu et al.	CO2	Electrolyzer	1	x	[95]
Ni et al.	CO2	Electrolyzer	1	x	[66]
Ni et al.	CO2	Electrolyzer	1	2	[67]

Table A.3: A list is obtained of all considered literature studies on electrochemical modeling for this research. A distinction between model 1 and model 2 for both the electrochemical model as the thermal model is made. Also, the list is categorized for different feedstocks. Lastly, the literature studies are categorized for fuel cells and electrolyzers.

A.6. Results, Current density

A.6.1. MEA

The one-dimensional current density within the electrochemical cell for a MEA geometry is shown in Figure A.5. It corresponds to the current in the middle of the cell. The electric current is constant in the diffusion layer and the ionic current is constant in the membrane. At the catalyst layer, the sum of the ionic and electric current is equal to the input current density. The ionic current decreases as it approaches the diffusion layer, while the electric current decreases near the membrane.

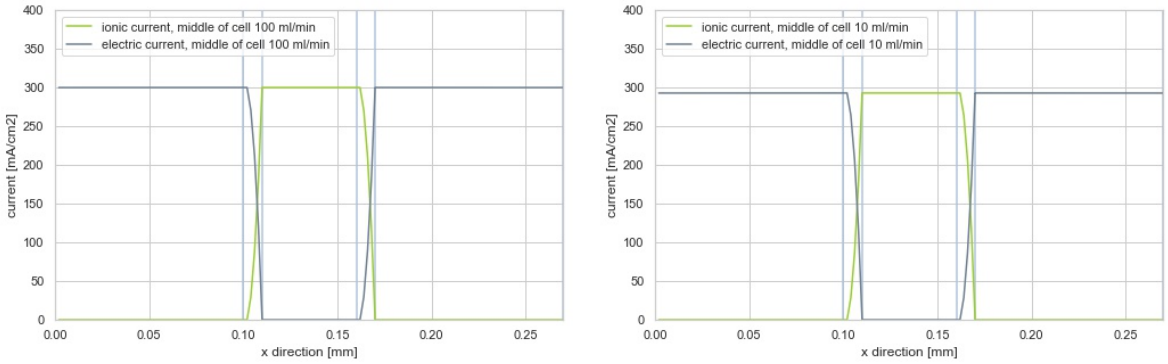

(a) 100 ml min^{-1} (b) 10 ml min^{-1}

Figure A.5: The 2D current density distribution within the MEA electrochemical cell in the x-direction. The y-direction is fixed at the half the channel length. The graphs show the results of both flow rates. The ionic and electric current are plotted separately.

A.6.2. GDE

The one-dimensional current density within the electrochemical cell for a GDE geometry is shown in Figure A.6. It corresponds to the current in the middle of the cell. The graph shows similarities to the MEA, except that there is also ionic current within the electrolyte.

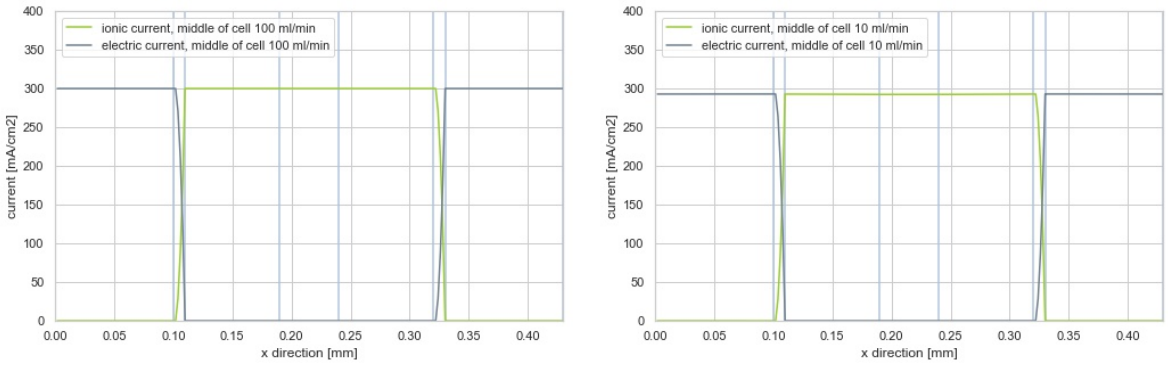

(a) 100 ml min^{-1} (b) 10 ml min^{-1}

Figure A.6: The 2D current density distribution within the GDE electrochemical cell in the x-direction. The y-direction is fixed at the half the channel length. The graphs show the results of both flow rates. The ionic and electric current are plotted separately.

A.7. Results, Heat generation

A.7.1. Joule heating

The contribution of joule heating by ohmic losses are presented in the following subchapter.

A.7.2. MEA

Figure A.7 shows that higher ionic losses occur. Near the membrane, the ionic losses are higher. Near the diffusion layer the electric losses increase.

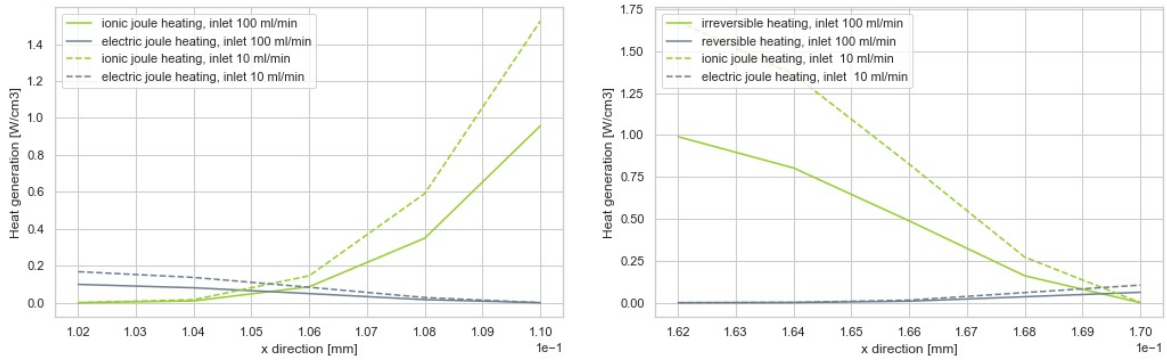

(a) MEA anode

(b) MEA cathode

Figure A.7: The joule heating divided for ohmic and ionic ohmic losses. The graphs show the results for both flow rates in the anode and cathode of the MEA. The ionic potential increases near the membrane and the electric potential decreases. Higher ionic ohmic losses can be expected.

A.7.3. GDE

From Figure A.8, it can be seen that overall, higher ionic losses occur. Closer to the membrane, the ionic losses are higher. On the other hand, the electric losses increase near the diffusion layer.

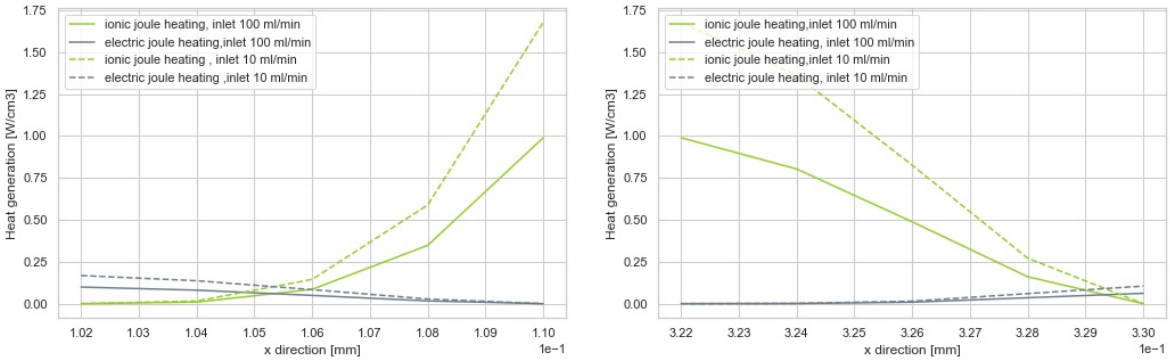

(a) GDE anode

(b) GDE cathode

Figure A.8: The joule heating divided for ohmic and ionic ohmic losses. The graphs show the results for both flow rates in the anode and cathode of the GDE. The ionic potential increases near the membrane and the electric potential decreases. Higher ionic ohmic losses can be expected.

B

Appendix B

B.1. Python Code

Below, a detailed description of the Python code can be found. The code is divided in the intialization, the mass model, electrochemical model and thermal model.

B.1.1. Initialization

For the code, packages need to be imported. The packages that are imported are numpy, statistics and math for the calculations, pyplot and seaborn for the plots and pandas for saving the data.

```
1
2  ### import packages
3
4
5
6  import numpy as np
7  import matplotlib.pyplot as plt
8  import math
9  import pandas as pd
10 import statistics
11 import seaborn as sns
12
13 exp= math.exp(1)
```

Listing B.1: The code describes the import of the packages used for the models in Python.

At the beginning, the initial values that are chosen are listed. In this way, the values can be easily found if any changes need to be applied.

```
1
2
3  ### initial values
4
5
6
7  T_0 = 298                                          # initial temperature [K]
8  Iin  =3000                                        # initial current density [A/m2]
9  flow_rate_gaschannel= 10 *10**-6                                  # initial flow rate [m3/min]
10 flow_rate= 0.1 *10**-6                             # initial flow rate [m3/min]
```

Listing B.2: The initial values used for this research. These values can be easily changes if other values have to be implemented.

The following part shows the dimensions of the cell. Also the discretization size Δx and Δy can be altered here. The parts creates arrays for the lengths from the dimensions.

```
1
2
3  ### initialization
4
5
6      ### dimensions
```

```

L_GDP = 10**-4                                  # gas diffusion plate length [m]
L_CL  = 10**-5                                  # catalyst layer length [m]
L_PEM = 5  *10**-5                                  # membrane length [m]
L_el  = 8*10**-5
L_cell     =  L_GDP + L_CL + L_PEM + L_CL + L_GDP + 2 * L_el    # total cell length [m]

radius_flowchannel = 10**-3 # = diameter
length_channel = 10**-2

width  = 1*10**-3                                    # cell width [m]
volume = L_CL*length_channel*width                   # catalyst volume [m3]

dx= 2 *10**-6                                   # x-direction step [m]
dy= 50*dx

n_GDP = L_GDP / dx                              # number of iterations in gas diffusion
    plate
n_el  = L_el / dx
n_CL  = L_CL / dx                               # number of iterations in catalyst layer
n_PEM = L_PEM / dx                              # number of iterations in membrane,
    recalculation

n_channel = length_channel/dy +1
n_radius = radius_flowchannel/dx +1

npts=  n_GDP + n_CL + n_PEM + n_GDP + n_CL +2*n_el +1       # number of iterations in full
    cell

x_GDP_L = np.linspace(0  ,                                      L_GDP,
              int(n_GDP)+1)
x_CL_L  = np.linspace(L_GDP,                                    L_GDP+L_CL,
              int(n_CL)+1)
x_el_L   = np.linspace(L_GDP+L_CL,                              L_GDP+L_CL+L_el,
              int(n_el)+1)
x_PEM   = np.linspace(L_GDP+L_CL+L_el,                          L_GDP+L_CL+L_el+L_PEM,
              int(n_PEM)+1)
x_el_R  = np.linspace(L_GDP+L_CL+L_el+L_PEM,                    L_GDP+L_CL+L_el+L_PEM+L_el,
              int(n_el)+1)
x_CL_R  = np.linspace(L_GDP+L_CL+L_el+L_PEM+L_el,               L_GDP+(2*L_CL)+L_PEM+2*L_el,
              int(n_CL)+1)
x_GDP_R = np.linspace(L_GDP+(2*L_CL)+2*L_el+L_PEM,              (2*L_GDP)+(2*L_el)+(2*L_CL)+
    L_PEM,       int(n_GDP)+1)

x_GDP_L = np.delete(x_GDP_L, 0)
x_CL_L  = np.delete(x_CL_L,  0)
x_CL_R  = np.delete(x_CL_R,  0)
x_PEM   = np.delete(x_PEM,   0)
x_el_L  = np.delete(x_el_L,   0)
x_el_R  = np.delete(x_el_R,   0)

x_cell  = np.concatenate(( x_GDP_L, x_CL_L,x_el_L, x_PEM,x_el_R, x_CL_R, x_GDP_R), axis=None)
x_channel  = np.linspace(0,                          length_channel,                      int(
    n_channel))
```

Listing B.3: The creation of the spatial arrays. The dimensions are used as input. The discretization size can also be altered here.

The initalization of the non-input parameters is done in this part of the code. Also, all other relevant input parameters are shown in this part of the code: The properties for the chosen materials and species, physical constants and electrochemical values.

```


    ### initial non-input parameters


phi_m0 = 0                                      # initial ionic potential [V]
phi_e0 = 0                                      # initial electric potential [V]
```

```
10
11 T_flow = T_0
12 J     =Iin * 1/L_CL                                    # initital volumentric current density
       [A/m3]
13 u= flow_rate_gaschannel/ (math.pi*(0.5*radius_flowchannel)**2*60) # velocity gas channel[m/s]
14
15
16
17
18
19 ### constants
20
21     ### general
22
23 R      = 8.314                                         # gas constant [J / (mol K )]
24 F      = 96485                                         # Faraday's constant [A/mol]
25 R_kn   = 0.5*10**-7
26
27
28
29
30     ### material properties
31
32
33         ### CO2
34
35 rho_CO2    = 1.795                                     # density [kg/m3]
36 mu_CO2 = 1.49*10**-5
37 Pr_CO2= 0.763378
38 M_CO2 = 44.04*10**-3
39 k_CO2= 0.01663
40 Re_channel= (rho_CO2 * u * radius_flowchannel) / mu_CO2
41 u_max= 2300*mu_CO2 / (rho_CO2 * radius_flowchannel)
42
43
44         #KOH
45 rho_KOH= 1.28*10**3
46 cp_KOH= 3*10**3
47
48
49 cp = 1646.75
50 rho_w = 1040
51
52
53         ### electrodes
54
55 Ag_diameter= 100*10**-9
56 IrO2_diameter = 10**10**-9
57
58
59
60         ### thermal conductivities
61
62 k_mem  = 0.17                                          # thermal conductivity coefficient [W
       /(L m)]
63 k_GDP  = 1.3                                          # thermal conductivity coefficient [W/(L
       m)]
64 k_CL   = 0.21                                         # thermal conductivity coefficient [W
       /(L m)]
65 k_el  = 0.45
66
67
68         ### electrical conductivities
69
70 sigma_eCL  = 100
71 sigma_eGDP = 220
72
73 sigma_mPEM   = 8
74 sigma_mKOH   = 10
75
76 C_CO2_ref = 50
```

```
C_O2_ref  = 100


        ### transport

S_GDP=0
S_CL =0.2
eps_GDP=0.8
eps_CL = 0.3

D_eff_CO2_flow= 0.21e-04

D_eff_CO2_value= 1.0231689519238029e-05
D_eff_O2_value=  5*10**(-4)


        ### electrochemical values


a_Ag = ((1-eps_CL)*6/Ag_diameter)              # electrocatalytic surface area [m2/m3]
a_IrO2= ((1-eps_CL)*6/IrO2_diameter)

delta_G_cath= 179600                                    # Gibbs free energy change cathode [J/
    mol]
delta_G_anode= 77260                                    # Gibss free energy change anode  [J/
    mol]

delta_H_cath= 108784                                    # enthalpy change cathode [J/mol]
delta_H_anode= 174200                                   # enthalpy change anode  [J/mol]


j0_a     = 1.4*10**(-5)                                 # exchange current density, cathode [A/
    m2]
j0_c     = 10**(-5)


E_th_calc_cathode = -(5.77902321e-04*T_0 + 7.58585483e-01)         # equilibrium potential [V
    ]
E_th_calc_anode =   -0.00103351*T_0 + 0.71061084


alpha_a = 1                                          # transfer coefficient [-]
alpha_c = 0.29                                            # transfer coefficient [-]

eta_m= 1                                              # electrolyte volume fraction of PEM [-]
lamda=14.15                                           # water content [-], eq=22, https://link.
    springer.com/article/10.1007/s40095-018-0288-2,  https://digitalcommons.odu.edu/cgi/
    viewcontent.cgi?article=1033&context=mae_etds
```

Listing B.4: Initialize non-input parameters.

Hereafter, the arrays are created from the input. This is needed in order to determine all values locally withtin the electrochemical cell.

```


### creating arrays

    ### conductivity

sigma_e = 0  *np.ones((int(npts),int(n_channel)))                    # [K]
sigma_m = sigma_mPEM  *np.ones((int(npts),int(n_channel)))                    # [K]

    ###temperature

Tn  = T_0  *np.ones((int(npts),int(n_channel)))                      # [K]
Tn1 = T_0 *np.ones((int(npts),int(n_channel)))           # [K]

factor_thermalconductivity = np.ones((int(npts),int(n_channel)))

    ### potentials
```

```
18
19 phi_m  = phi_m0*np.ones((int(npts),int(n_channel)))           # [V]
20 phi_m1 = phi_m0*np.ones((int(npts),int(n_channel)))              # [V]
21
22 phi_e  = phi_e0*np.ones((int(npts),int(n_channel)))          # [V]
23 phi_e1 = phi_e0*np.ones((int(npts),int(n_channel)))             # [V]
24
25 eta_a = 0*np.ones((int(npts),int(n_channel)))                          # [V]
26 eta_c = 0*np.ones((int(npts),int(n_channel)))             # [V]
27
28 eta_a_ALL = 0*np.ones((int(npts),int(n_channel)))           # [V]
29 eta_c_ALL = 0*np.ones((int(npts),int(n_channel)))                  # [V]
30
31
32     ### diffusion
33
34 D_eff_CO2 = 0*np.ones((int(npts),int(n_channel)))
35 D_eff_O2 = 0*np.ones((int(npts),int(n_channel)))
36
37
38     ### concentration
39
40 C_CO2 = 0*np.ones((int(npts),int(n_channel)))
41 C_CO21 = 0*np.ones((int(npts),int(n_channel)))
42 C_O2 = C_O2_ref*np.ones((int(npts),int(n_channel)))
43 C_O21 = C_O2_ref*np.ones((int(npts),int(n_channel)))
44 C_OH = C_O2_ref*np.ones((int(npts),int(n_channel)))
45
46
47 C_CO2_channel=0*np.ones([int(n_radius),int(n_channel)])
48 C_CO2_channel1=0*np.ones([int(n_radius),int(n_channel)])
49
50 Concentratie_flow=np.ones([int(n_radius),int(n_channel)])
51
52
53     ### source terms
54
55 Q_ohm_ion2  = 0*np.ones((int(npts),int(n_channel)))
56 Q_ohm_elec2 = 0*np.ones((int(npts),int(n_channel)))
57
58 Q_ohm_mem2=      0*np.ones((int(npts),int(n_channel)))
59 Q_cathode_irr  = 0*np.ones((int(npts),int(n_channel)))
60 Q_anode_irr    = 0*np.ones((int(npts),int(n_channel)))
61
62 Q_cathode_rev  = 0*np.ones((int(npts),int(n_channel)))
63 Q_anode_rev  = 0*np.ones((int(npts),int(n_channel)))
64
65     ### current density
66
67
68 J_mem_test= 0*np.ones((int(npts),int(n_channel)))
69 Jc= J*np.ones((int(npts),int(n_channel)))
70 Ja= J*np.ones((int(npts),int(n_channel)))
71
72 j_elec = 0*np.ones((int(npts),int(n_channel)))
73 j_prot = 0*np.ones((int(npts),int(n_channel)))
74 j_protonic = 0*np.ones((int(npts),int(n_channel)))
75
76
77
78     ### transfer coefficients + dimensionless numbers
79
80
81 k= 1*np.ones((int(npts),int(n_channel)))
82
83 Sh= 1*np.ones((int(n_radius),int(n_channel)))
84 Sh_m= 1*np.ones((int(n_radius),int(n_channel)))
85
86 K_CO2= 1*np.ones((int(n_radius),int(n_channel)))
87 K_O2= 1*np.ones((int(n_radius),int(n_channel)))
88
```

```

Re_CO2= 1*np.ones((int(n_radius),int(n_channel)))
Pe= 1*np.ones((int(n_radius),int(n_channel)))

Pe_m= 0*np.ones((int(n_radius),int(n_channel)))

Nu= 1*np.ones((int(n_radius),int(n_channel)))
h= 1*np.ones((int(n_radius),int(n_channel)))

    ## convergence

convergence_concentration=np.ones([int(npts),int(n_channel)])
convergence_electrochemical=np.ones([int(npts),int(n_channel)])
convergence_all= np.ones([int(npts),int(n_channel)])
convergence_thermal= np.ones([int(npts),int(n_channel)])
```

Listing B.5: Creating all arrays from the input.

All calculations that done beforehand can be found in this part of the code. All dimensionless numbers are defined here. Also, the diffusion and mass coefficients, needed for the mass model, are calculated here. Similar, the heat transfer coefficient is calculated in this part. The concentration in the channel is calculated separately from the electrochemical cell and is also presented. Lasty, the velocity profile in the electrolyte is determined.

```


### pre calculations


    ### cell potential calculations, if galvanostatic

eta_a_pre =   (R*T_0)/(F*alpha_a)* np.log( Iin /(L_CL*a_IrO2*j0_a))
eta_c_pre = -(R*T_0)/(F*alpha_c)* np.log( Iin /(L_CL*a_Ag*j0_c))
protonic_loss= Iin * (2*L_CL+L_PEM) / sigma_mPEM
electric_loss= Iin * 2*L_CL / sigma_eCL  + Iin * 2*L_GDP / sigma_eCL



    ### calculation effective diffusion coefficient


D_eff_GDP_O2 = D_eff_O2_value*(1-S_GDP)**2.15*(0.906*eps_GDP-0.252)
D_eff_GDP_CO2 = D_eff_CO2_value*(1-S_GDP)**2.15*(0.906*eps_GDP-0.252)

D_eff_CL_O2 = D_eff_O2_value*(1-S_CL)**(2)*((eps_CL-0.25)/(1-0.25))**2
D_eff_CL_CO2 = D_eff_CO2_value*(1-S_CL)**(2)*((eps_CL-0.25)/(1-0.25))**2



D_knudsen= (2/3)*R_kn*  ((8*R*T_0)/(math.pi*M_CO2))



        ### calculating heat and mass transfer coefficient


for j in range (0, int(n_channel)):
    for i in range (0, int(n_radius) ):

        Sc= mu_CO2/ (rho_CO2*D_eff_CO2_flow)
        Re_CO2[i,j] = (rho_CO2 * u * radius_flowchannel ) / mu_CO2
        Pe_m[i,j] = Re_CO2[i,j] * Sc
        Sh[i,j] = 0.5 *  (Pe_m[i,j]*radius_flowchannel/(dy*(j+0.00000000001)))**(1/3)
        K_CO2[i,j] = (D_eff_CO2_flow*Sh[i,j])/radius_flowchannel
        Shd= (D_eff_GDP_CO2*radius_flowchannel)/ (L_GDP*D_eff_CO2_flow)

        S = 1/ (1/Sh + 1/Shd).mean()
        Gz =  Re_CO2[i,j] * Sc *(radius_flowchannel/10**-2)
        Sh_m= Sh[1,1:-1].mean()


```

```
        Pe[i,j] = Re_CO2[i,j] * Pr_CO2

        Nu[i,j]  = 0.5 *  (Pe[i,j]*radius_flowchannel/(dy*(j+0.00000000001)))**(1/3)
        h[i,j] =  (Nu[i,j]*k_CO2 ) /radius_flowchannel


for j in range (0, int(n_channel)-1):
    for i in range (0, int(n_radius)-1 ):

        Concentratie_flow[i,j]= exp**-((S* D_eff_CO2_flow)*dy*j/ (u *radius_flowchannel**2))*
     C_CO2_ref


Concentratie_flow[0,-1]=Concentratie_flow[0,-2]

    ### calculation concentration electrochemical cell y-direction

for n in range(1,2000):


    for j in range (1, int(n_channel)-1):



        C_CO2_channel1[0,j] = ((Concentratie_flow[0,j] * dy*K_CO2[1,j])/D_eff_CO2_flow +
    C_CO2_channel[1,j] *dy/dx+ 0.5* C_CO2_channel[0,j-1] *dx/dy + 0.5* C_CO2_channel[0,j+1] *
    dx/dy)/ (K_CO2[1,j]/D_eff_CO2_flow*dy+ dx/dy +dy/dx)

        C_CO2_channel1[0,0]=  C_CO2_ref
        C_CO2_channel1[1,0]=  C_CO2_ref

    C_CO2_channel1[1,:]= C_CO2_channel1[0,:]

    C_CO2_channel1[0,-1]= C_CO2_channel1[0,-2]
    C_CO2_channel1[1,-1]= C_CO2_channel1[1,-2]
    C_CO2_channel= C_CO2_channel1

    ### calculation of parabolic velocity electrolyte

u_el= flow_rate/ (L_el*width*60)

velocity_left=np.zeros([int(npts), int(n_channel)])
velocity_right=np.zeros([int(npts), int(n_channel)])

parabolic_velocity= u_el/(L_el/2 )**2

for j in range (1,int(n_channel)-1):

    for l in range(0,int(n_GDP+n_CL+n_PEM+n_CL+n_GDP+1+2*n_el)-1 ):

        velocity_left[l,j]=   -parabolic_velocity*((dx*l-(L_GDP+L_CL+0.5*L_el)))**2 +u_el
        velocity_right[l,j]=   -parabolic_velocity*((dx*l-(L_GDP+L_CL+L_PEM+L_el+0.5*L_el)))
    **2 +u_el


for j in range (0, int(n_channel)):
    for i in range (int(n_GDP+n_CL+n_PEM+ 2*n_el) ,int(2*n_GDP+2*n_CL+n_PEM+ 2*n_el)+1):
        C_CO21[i,j]= C_CO2_channel1[0,j]
        C_CO2[i,j]= C_CO2_channel1[0,j]
```

Listing B.6: The pre-calculations done within the code can be found in this part.

After the calculations, the values are included in the created arrays. As different materials are used, this is done for each separate layer of the electrochemical cell.

```


### filling in local values arrays


for j in range (0,int(n_channel)):
```

```
7
8
9
10      for i in range(0,int(n_GDP)):
11          sigma_e[i,j] = sigma_eGDP
12          k[i,j]       = k_GDP
13          D_eff_O2[i,j]= D_eff_GDP_O2
14          D_eff_CO2[i,j]= D_eff_GDP_CO2
15
16      for i in range(int(n_GDP), int(n_GDP+n_CL)):
17          sigma_e[i,j] = sigma_eCL
18          sigma_m[i,j] = sigma_mKOH
19          k[i,j]       = k_CL
20          D_eff_O2[i,j]= D_eff_CL_O2
21          D_eff_CO2[i,j]= D_eff_CL_CO2
22
23      for i in range(int(n_GDP+n_CL),int(n_GDP+n_CL+n_el)):
24          sigma_m[i,j] = sigma_mKOH
25          k[i,j]       = k_mem
26          D_eff_CO2[i,j]=D_eff_CL_CO2
27          D_eff_O2[i,j]= D_eff_CL_O2
28
29
30      for i in range(int(n_GDP+n_CL+n_el),int(n_GDP+n_CL+n_PEM+n_el)):
31          k[i,j]       = k_mem
32          D_eff_O2[i,j]= D_eff_CL_O2
33          D_eff_CO2[i,j]= D_eff_CL_CO2
34          sigma_m[i,j] = sigma_mPEM
35
36      for i in range(int(n_GDP+n_CL+n_el+n_PEM),int(n_GDP+n_CL+n_PEM+2*n_el)):
37          sigma_m[i,j] = sigma_mKOH
38          k[i,j]      = k_mem
39          D_eff_CO2[i,j]= D_eff_CL_CO2
40          D_eff_O2[i,j]= D_eff_CL_O2
41
42      for i in range(int(n_GDP+n_CL+n_PEM+2*n_el),int(n_GDP+n_CL+n_PEM+n_CL+2*n_el) ):
43          sigma_e[i,j] = sigma_eCL
44          sigma_m[i,j] = sigma_mKOH
45          k[i,j]       = k_CL
46          D_eff_CO2[i,j]= D_eff_CL_CO2
47          D_eff_O2[i,j]= D_eff_CL_O2
48
49      for i in range(int(n_GDP+n_CL+n_PEM+n_CL+2*n_el),int(n_GDP+n_CL+n_PEM+n_CL+n_GDP+1+2*n_el
        ) ):
50          sigma_e[i,j] = sigma_eGDP
51          k[i,j]       = k_GDP
52          D_eff_O2[i,j]= D_eff_GDP_O2
53          D_eff_CO2[i,j]= D_eff_GDP_CO2
```

Listing B.7: Filling in the created arrays with the calculated values.

B.1.2. Concentration model

In the following part of the model, the concentration model is shown. This is the concentration model within the electrochemical cell, meaning in the x-direction. The conservation of species is solved within this model.

```
1
2   ### CONCENTRATION MODEL ###
3
4
5
6
7
8
9   while convergence_concentration[int(n_GDP+2*n_CL+n_PEM+2+2*n_el),2] > 0.0001:
10
11
12
13          for j in range (1, int(n_channel)-1):
```

```
14
15
16
17
18          # Gas diffusion plate left
19          for t in range(1,int(n_GDP)):
20
21              C_CO21[t,j] = 0
22
23
24
25          # Catalyst anode layer left
26
27          for t in range(int(n_GDP),       int(n_GDP+n_CL)):
28
29              C_CO21[t,j] = 0
30
31
32          C_CO21[int(n_GDP+n_CL),j] = C_CO21[int(n_GDP+n_CL)-1,j]
33
34
35
36              #electrolyte
37
38          for t in range(int(n_GDP+n_CL+1),int(n_GDP+n_CL+n_el)):
39
40              C_CO21[t,j] = np.nan
41
42
43
44              # PEM
45
46          for t in range(int(n_GDP+n_CL+n_el+1),int(n_GDP+n_CL+n_PEM+n_el)):
47
48              C_CO21[t,j] = np.nan
49
50
51
52              # electrolyte
53
54          for t in range(int(n_GDP+n_CL+n_el+n_PEM),int(n_GDP+n_CL+n_PEM+2*n_el)):
55
56              C_CO21[t,j] = np.nan
57
58
59          # Catalyst cathode layer right
60
61          for t in range(int(n_GDP+n_CL+2*n_el+n_PEM+1),int(n_GDP+n_CL+2*n_el+n_PEM+2)):
62
63              if 0.5*(D_eff_CO2[t,j]+D_eff_CO2[t+1,j])/(0.5*D_eff_CO2[t+1,j]+0.5*D_eff_CO2[
    t-1,j] + D_eff_CO2[t,j])*C_CO2[t+1,j] + 0.5*(D_eff_CO2[t,j]+D_eff_CO2[t-1,j])/(0.5*
    D_eff_CO2[t+1,j]+0.5*D_eff_CO2[t-1,j] + D_eff_CO2[t,j])*C_CO2[t-1,j] < (Ja[t,j]*dx**2)
    /((0.5*D_eff_CO2[t+1,j]+0.5*D_eff_CO2[t-1,j] +  D_eff_CO2[t,j])*2*F) :
64                  H=0
65              else:
66                  H=1
67
68
69          for t in range(int(n_GDP+n_CL+2*n_el+n_PEM+1),int(n_GDP+2*n_CL+n_PEM+2*n_el)):
70
71
72
73              C_CO21[t,j] = 0.5*(D_eff_CO2[t,j]+D_eff_CO2[t+1,j])/(0.5*D_eff_CO2[t+1,j
    ]+0.5*D_eff_CO2[t-1,j] + D_eff_CO2[t,j])*C_CO2[t+1,j] + 0.5*(D_eff_CO2[t,j]+D_eff_CO2[t
    -1,j])/(0.5*D_eff_CO2[t+1,j]+0.5*D_eff_CO2[t-1,j] + D_eff_CO2[t,j])*C_CO2[t-1,j] - H*(Jc[
    t,j]*dx**2)/((0.5*D_eff_CO2[t+1,j]+0.5*D_eff_CO2[t-1,j] +  D_eff_CO2[t,j])*2*F)
74
75
76          C_CO21[int(n_GDP+2*n_el+n_CL+n_PEM),j] =     0
77
78
```

```
            # Gas diffuston plate right
            for t in range(int(n_GDP+2*n_CL+n_PEM+2*n_el),int(2*n_GDP+n_PEM+2*n_CL+2*n_el) ):

                convergence_concentration[t,j]= C_CO21[t,j] -  (0.5*(D_eff_CO2[t,j]+D_eff_CO2[t+1,j])/(0.5*D_eff_CO2[t+1,j]+0.5*D_eff_CO2[t-1,j] + D_eff_CO2[t,j])*C_CO2[t+1,j] + 0.5*(D_eff_CO2[t,j]+D_eff_CO2[t-1,j])/(0.5*D_eff_CO2[t+1,j]+0.5*D_eff_CO2[t-1,j] + D_eff_CO2[t,j])*C_CO2[t-1,j] )

                C_CO21[t,j] = 0.5*(D_eff_CO2[t,j]+D_eff_CO2[t+1,j])/(0.5*D_eff_CO2[t+1,j]+0.5*D_eff_CO2[t-1,j] + D_eff_CO2[t,j])*C_CO2[t+1,j] + 0.5*(D_eff_CO2[t,j]+D_eff_CO2[t-1,j])/(0.5*D_eff_CO2[t+1,j]+0.5*D_eff_CO2[t-1,j] + D_eff_CO2[t,j])*C_CO2[t-1,j]



            C_CO21[0,j] = 0


            C_CO2 = C_CO21



C_CO2[:,-1]=C_CO2[:,-2]

C_OH[int(n_GDP)-1:int(n_GDP+n_CL)+1,:] = C_CO2[int(n_GDP+n_CL+n_PEM+2*n_el)-1:int(n_GDP+n_CL+n_PEM+2*n_el+n_CL)+1,:]
C_O21 = C_OH
C_O2 = C_OH
```

Listing B.8: The code describes the concentration model in Python.

B.1.3. Boundary Conditions

The boundary conditions are updated by the concentration model and are used for the electrochemical model. The boundary conditions are continously updated, as the boundary conditions are also temperature dependent.

```



### BOUNDARY CONDITIONS ELECTROCHEMICAL MODEL ###


phi_m  = phi_m0*np.ones((int(npts),int(n_channel)))           # [V]
phi_m1 = phi_m0*np.ones((int(npts),int(n_channel)))               # [V]

phi_e  = phi_e0*np.ones((int(npts),int(n_channel)))          # [V]
phi_e1 = phi_e0*np.ones((int(npts),int(n_channel)))             # [V]

eta_a = 0*np.ones((int(npts),int(n_channel)))                            # [V]
eta_c = 0*np.ones((int(npts),int(n_channel)))             # [V]

desiredcurrentdensityloc= 1*np.ones((int(npts),int(n_channel)))
Input_current= 1*np.ones((int(npts),int(n_channel)))

eta_c_pre2 = 1*np.ones((int(npts),int(n_channel)))
eta_a_pre2 = 1*np.ones((int(npts),int(n_channel)))

E_th_calc_cathode = 1*np.ones((int(npts),int(n_channel)))
E_th_calc_anode = 1*np.ones((int(npts),int(n_channel)))

E_tn_calc_cathode = 1*np.ones((int(npts),int(n_channel)))
E_tn_calc_anode = 1*np.ones((int(npts),int(n_channel)))




    ###initialize

for j in range (0,int(n_channel)):
```

```
35
36
37      E_th_calc_cathode[:,j] = -(5.77902321e-04*Tn1[int(n_GDP+n_CL+n_PEM),j] + 7.58585483e-01)
                # equilibrium potential [V]
38      E_th_calc_anode[:,j] =   -0.00103351*Tn1[int(n_GDP+n_CL),j] + 0.71061084
39
40      E_tn_calc_cathode[:,j] = -4.44672681e-04*Tn[int(n_GDP+n_CL+n_PEM),j] + 6.97817981e-01
41      E_tn_calc_anode[:,j] = 4.68910967e-04*Tn1[int(n_GDP+n_CL),j]+ 7.61678071e-01
42
43      for i in range (int(n_GDP+n_CL+n_el), int(n_el+ n_GDP + n_CL + n_PEM)):
44          sigma_m[i,j] =  0.12 * (Tn1[i,j]-273) + 4.05
45
46      for i in range(0,int(npts)):
47
48
49
50          desiredcurrentdensityloc[i,j]= 1/(((C_CO2[-1,:])/C_CO2_ref).mean())*(C_CO2[-1,j].mean
        ())/C_CO2_ref
51          Input_current[i,j] = Iin * desiredcurrentdensityloc[i,j]
52
53          eta_c_pre2[i,j] =  -(R*Tn1[i,j])/(F*alpha_c)* np.log( Input_current[i,j] /(L_CL*a_Ag*
        j0_c))
54          eta_a_pre2[i,j] =  (R*Tn1[i,j])/(F*alpha_a)* np.log( Input_current[i,j] /(L_CL*a_IrO2
        *j0_a))
55
56      phi_e[0:int(n_GDP+n_CL)+1,j] = E_th_calc_anode[i,j] +eta_a_pre2[0:int(n_GDP+n_CL)+1,j]
57
58
59      phi_e[int((n_GDP)+n_PEM+n_CL+2*n_el):int(1+(2*n_GDP)+(2*n_CL)+n_PEM+2*n_el),j]=
        E_th_calc_cathode[i,j]+eta_c_pre2[int((n_GDP)+n_PEM+n_CL+2*n_el):int(1+(2*n_GDP)+(2*n_CL)
        +n_PEM+2*n_el),j]
60
61  phi_e1=phi_e
```

Listing B.9: The boundary conditions for the electrochemical model.

B.1.4. Electrochemical model

In this part, the electrochemical model is shown, where the conservation of charged is solved. Hereafter, the boundary conditions of the electric and ionic potential are continously updated within the model.

```
1
2
3
4   while convergence_electrochemical  > 0.000001:
5
6       premax_current = j_elec.min()
7
8       for j in range (1, int(n_channel)-1):
9
10          plt.clf()
11
12
13          # Gas diffusion plate left
14          for i in range(1,int(n_GDP)):
15              phi_e1[i,j] = 0.5*(sigma_e[i,j]+sigma_e[i+1,j])/(0.5*sigma_e[i+1,j]+0.5*sigma_e[i
        -1,j] + sigma_e[i,j])*phi_e[i+1,j] + 0.5*(sigma_e[i,j]+sigma_e[i-1,j])/(0.5*sigma_e[i+1,j
        ]+0.5*sigma_e[i-1,j] + sigma_e[i,j])*phi_e[i-1,j]
16              phi_m1[i,j] = phi_m1[int(n_GDP),j]
17
18              j_elec[i,j] = (-phi_e1[i,j]+phi_e1[i+1,j])/(dx) * (0.5*sigma_e[i+1,j] + 0.5*
        sigma_e[i,j])
19
20
21
22          # Catalyst anode layer left
23
24          for i in range(int(n_GDP),       int(n_GDP+n_CL)):
25
```

```
            phi_e1[i,j] = 0.5*(sigma_e[i,j]+sigma_e[i+1,j])/(0.5*sigma_e[i+1,j]+0.5*sigma_e[i-1,j] + sigma_e[i,j])*phi_e[i+1,j] + 0.5*(sigma_e[i,j]+sigma_e[i-1,j])/(0.5*sigma_e[i+1,j]+0.5*sigma_e[i-1,j] + sigma_e[i,j])*phi_e[i-1,j] - Ja[i,j]*dx**2/(0.5*sigma_e[i+1,j]+0.5*sigma_e[i-1,j] + sigma_e[i,j])
            phi_m1[i,j] = 0.5*(sigma_m[i,j]+sigma_m[i+1,j])/(0.5*sigma_m[i+1,j]+0.5*sigma_m[i-1,j] + sigma_m[i,j])*phi_m[i+1,j] + 0.5*(sigma_m[i,j]+sigma_m[i-1,j])/(0.5*sigma_m[i+1,j]+0.5*sigma_m[i-1,j] + sigma_m[i,j])*phi_m[i-1,j] + Ja[i,j]*dx**2/(0.5*sigma_m[i+1,j]+0.5*sigma_m[i-1,j] + sigma_m[i,j])
            j_elec[i,j] = (-phi_e1[i,j]+phi_e1[i+1,j])/(dx) * (0.5*sigma_e[i+1,j]+ 0.5*sigma_e[i,j])

            j_prot[i,j]=  (phi_m1[i,j]-phi_m1[i+1,j])/(dx) *(0.5*sigma_m[i+1,j]+ 0.5* sigma_m[i,j])



        phi_e1[int(n_GDP+n_CL),j] = phi_e1[int(n_GDP+n_CL)-1,j]



        # Electrolyte left

        for i in range(int(n_GDP+n_CL),int(n_GDP+n_CL+n_el)):

            phi_m1[i,j] = 0.5*(sigma_m[i,j]+sigma_m[i+1,j])/(0.5*sigma_m[i+1,j]+0.5*sigma_m[i-1,j] + sigma_m[i,j])*phi_m[i+1,j] + 0.5*(sigma_m[i,j]+sigma_m[i-1,j])/(0.5*sigma_m[i+1,j]+0.5*sigma_m[i-1,j] + sigma_m[i,j])*phi_m[i-1,j]
            j_prot[i,j]=  (phi_m1[i,j]-phi_m1[i+1,j])/(dx) *(0.5*sigma_m[i+1,j]+ 0.5* sigma_m[i,j])



        for i in range(int(n_GDP+n_CL+1),int(n_GDP+n_CL+n_el-1)):
            phi_e1[i,j] = np.nan


        # PEM
        for i in range(int(n_GDP+n_CL+n_el),int(n_GDP+n_CL+n_PEM+n_el)):

            phi_m1[i,j] = 0.5*(sigma_m[i,j]+sigma_m[i+1,j])/(0.5*sigma_m[i+1,j]+0.5*sigma_m[i-1,j] + sigma_m[i,j])*phi_m[i+1,j] + 0.5*(sigma_m[i,j]+sigma_m[i-1,j])/(0.5*sigma_m[i+1,j]+0.5*sigma_m[i-1,j] + sigma_m[i,j])*phi_m[i-1,j]
            j_prot[i,j]=  (phi_m1[i,j]-phi_m1[i+1,j])/(dx) *(0.5*sigma_m[i+1,j]+ 0.5* sigma_m[i,j])


        for i in range(int(n_GDP+n_CL+n_el),int(n_GDP+n_CL+n_PEM+n_el)-1):
            phi_e1[i,j] = np.nan



        # Electrolyte right

        for i in range(int(n_GDP+n_CL+n_el+n_PEM),int(n_GDP+n_CL+n_PEM+2*n_el)):
            phi_m1[i,j] = 0.5*(sigma_m[i,j]+sigma_m[i+1,j])/(0.5*sigma_m[i+1,j]+0.5*sigma_m[i-1,j] + sigma_m[i,j])*phi_m[i+1,j] + 0.5*(sigma_m[i,j]+sigma_m[i-1,j])/(0.5*sigma_m[i+1,j]+0.5*sigma_m[i-1,j] + sigma_m[i,j])*phi_m[i-1,j]
            j_prot[i,j]=  (phi_m1[i,j]-phi_m1[i+1,j])/(dx) *(0.5*sigma_m[i+1,j]+ 0.5* sigma_m[i,j])


        for i in range(int(n_GDP+n_CL+n_el+n_PEM),int(n_GDP+n_CL+n_PEM+2*n_el)-1):
            phi_e1[i,j] = np.nan



        phi_e1[int(n_GDP+n_CL+n_PEM+2*n_el)-1,j] = phi_e1[int(n_GDP+n_CL+n_PEM+2*n_el),j]



        # Catalyst cathode layer right
```

```
        for i in range(int(n_GDP+n_CL+n_PEM+2*n_el),int(n_GDP+n_CL+n_PEM+n_CL+2*n_el) ):

            phi_e1[i,j] = 0.5*(sigma_e[i,j]+sigma_e[i+1,j])/(0.5*sigma_e[i+1,j]+0.5*sigma_e[i-1,j] + sigma_e[i,j])*phi_e[i+1,j] + 0.5*(sigma_e[i,j]+sigma_e[i-1,j])/(0.5*sigma_e[i+1,j]+0.5*sigma_e[i-1,j] + sigma_e[i,j])*phi_e[i-1,j] + Jc[i,j]*dx**2/(0.5*sigma_e[i+1,j]+0.5*sigma_e[i-1,j] + sigma_e[i,j])
            phi_m1[i,j] = 0.5*(sigma_m[i,j]+sigma_m[i+1,j])/(0.5*sigma_m[i+1,j]+0.5*sigma_m[i-1,j] + sigma_m[i,j])*phi_m[i+1,j] + 0.5*(sigma_m[i,j]+sigma_m[i-1,j])/(0.5*sigma_m[i+1,j]+0.5*sigma_m[i-1,j] + sigma_m[i,j])*phi_m[i-1,j] - Jc[i,j]*dx**2/(0.5*sigma_m[i+1,j]+0.5*sigma_m[i-1,j] + sigma_m[i,j])

            j_elec[i,j] = (-phi_e1[i,j]+phi_e1[i+1,j])/(dx)* (0.5*sigma_e[i+1,j]+ 0.5* sigma_e[i,j])
            j_prot[i,j]=  (phi_m1[i,j]-phi_m1[i+1,j])/(dx) *(0.5*sigma_m[i+1,j]+ 0.5* sigma_m[i,j])




        # Gas diffusion plate right
        for i in range(int(n_GDP+n_CL+n_PEM+n_CL+2*n_el),int(n_GDP+n_CL+n_PEM+n_CL+n_GDP+1+2*n_el)-1 ):
            phi_e1[i,j] = 0.5*(sigma_e[i,j]+sigma_e[i+1,j])/(0.5*sigma_e[i+1,j]+0.5*sigma_e[i-1,j] + sigma_e[i,j])*phi_e[i+1,j] + 0.5*(sigma_e[i,j]+sigma_e[i-1,j])/(0.5*sigma_e[i+1,j]+0.5*sigma_e[i-1,j] + sigma_e[i,j])*phi_e[i-1,j]
            phi_m1[i,j] = phi_m1[i-1,j]


            j_elec[i,j] = (-phi_e1[i,j]+phi_e1[i+1,j])/(dx)* (0.5*sigma_e[i+1,j]+ 0.5* sigma_e[i,j])




        for i in range(int(n_GDP+n_CL+n_el+n_PEM+n_el), int(2*n_GDP+(2*n_CL)+n_PEM+2*n_el)):

            eta_c[i,j] =  phi_e1[i,j] - phi_m1[i,j]-E_th_calc_cathode[i,j]


            Jc[i,j]= j0_c * a_Ag *exp ** ((-eta_c[i,j]*alpha_c*F)/(R*Tn1[i,j])) * (C_CO2[i,j] /C_CO2_ref)




        desiredcurrentdensityloc_cat= 1/(((C_CO2[-1,:])/C_CO2_ref).mean())*(C_CO2[-1,j].mean())/C_CO2_ref
        shift=  (Iin*desiredcurrentdensityloc_cat-Jc[int(n_GDP+n_CL+n_PEM+2*n_el):int(n_GDP+n_CL+n_PEM+n_CL+2*n_el),j].mean()*L_CL)*dx

        if shift>0:
            phi_m1[:,j] = phi_m1[:,j] + shift




        for i in range(0,       int(n_GDP+n_CL)):
            eta_a[i,j] = phi_e1[i,j] - phi_m1[i,j]   - E_th_calc_anode[i,j]
            Ja[i,j]= j0_a * a_IrO2 * exp ** ((eta_a[i,j]*alpha_a*F)/(R*Tn1[i,j]))* C_O2[i,j] /C_O2_ref #* (C_O2 /C_ref_O2)  #* exp**(-7900*((1/Tn1)-1/353.15))




        desiredcurrentdensityloc_an= 1/(((C_CO2[-1,:])/C_CO2_ref).mean())*(C_CO2[-1,j].mean())/C_CO2_ref
        delta_potential=  (Iin*desiredcurrentdensityloc_an-Ja[int(n_GDP):int(n_CL+n_GDP),j].mean()*L_CL)*dx

```

```
        if delta_potential>0:
            phi_e1[int(0):int((n_GDP)+(n_CL)+1),j] = phi_e1[int(0):int((n_GDP)+(n_CL)+1),j]+
    delta_potential


        for i in range(int(n_GDP+n_CL+n_PEM+2*n_el), int(2*n_GDP+(2*n_CL)+n_PEM+2*n_el)):
            eta_c[i,j] = phi_e1[i,j] - phi_m1[i,j]  - E_th_calc_cathode[i,j]

        for i in range(0,       int(n_GDP+n_CL)):

            eta_a[i,j] = phi_e1[i,j] - phi_m1[i,j] - E_th_calc_anode[i,j]


        for i in range(0,       int(n_GDP+n_CL)):

            Ja[i,j]= j0_a * a_IrO2 * exp ** ((eta_a[i,j]*alpha_a*F)/(R*Tn1[i,j])) * C_O2[i,j]
     /C_O2_ref

        for i in range(int(n_GDP+n_CL+n_el+n_PEM+n_el), int(2*n_GDP+(2*n_CL)+n_PEM+2*n_el)):

            Jc[i,j]= j0_c * a_Ag *exp ** ((-eta_c[i,j]*alpha_c*F)/(R*Tn1[i,j]))* (C_CO2[i,j]
    /C_CO2_ref)



        # full cell
        for i in range(1,int(npts)-1):

            j_protonic[i,j]=  (phi_m1[i,j]-phi_m1[i+1,j])/(dx) *(0.5*sigma_m[i+1,j]+ 0.5*
    sigma_m[i,j])


        phi_e = phi_e1
        phi_m = phi_m1




    for i in range(0,int((2*n_GDP)+(2*n_CL)+n_PEM+2*n_el)):
        phi_m1[i,-1] =phi_m1[i,-2]
        phi_m1[i,0]  =phi_m1[i,1]
        j_elec[i,0] = j_elec[i,1]
        j_prot[i,0] = j_prot[i,1]
        j_prot[i,-1] = j_prot[i,-2]

        j_elec[i,-1] = j_elec[i,-2]
        phi_e1[i,-1] =phi_e1[i,-2]
        phi_e1[i,0]  =phi_e1[i,1]
        eta_a[i,-1]  =eta_a[i,-2]
        eta_c[i,-1]  =eta_c[i,-2]
        eta_a[i,0]  =eta_a[i,1]
        eta_c[i,0]  =eta_c[i,1]
        Jc[i,-1]     =Jc[i,-2]
        Ja[i,-1]     =Ja[i,-2]
        Ja[i,0]  =Ja[i,1]
        Jc[i,0]  =Jc[i,1]



    for j in range (0,int(n_channel)):

        j_elec[0,j]= j_elec[1,j]
        j_elec[-1,j] =  j_elec[-2,j]
        j_prot[-1,j] =  j_prot[-2,j]

        #j_elec[int(n_GDP)-1,j] =  j_elec[int(n_GDP),j]
        phi_m1[-1,j] =phi_m1[-2,j]
        phi_m1[0,j]  =phi_m1[1,j]
        Jc[-1,j]     =Jc[-2,j]

    phi_e = phi_e1
```

```
    phi_m = phi_m1
    max_current = j_elec.min()
    convergence_electrochemical = premax_current - max_current

current= -j_elec+j_prot
old_temperature = Tn1
```

Listing B.10: The code describes the electrochemical model in Python.

B.1.5. Temperature model

To conclude, the thermal model is shown. Within the thermal model, the conservation of thermal energy is solved. This is done by first determining the source terms, that are effected by the electrochemical model.

```
## THERMAL MODEL ###


#while convergence_thermal.min() < -10**-6:

for n in range(1,8):


    phi_e_eta= np.nan_to_num(phi_e)

    for j in range (1,int(n_channel)-1):

        Tn1[0,j] = ((T_flow * dy*h[0,j])/k[0,j] + 0.5*Q_ohm_elec2[0,j]*dx*dy/k[0,j] +  Tn[1,j] *dy/dx+ 0.5* Tn[0,j-1] *dx/dy+ 0.5* Tn[0,j+1] *dx/dy)/ (h[0,j]/k[0,j]*dy+ dx/dy +dy/dx)


        # Gas diffusion plate left
        for l in range(1,int(n_GDP)):

            # source term
            Q_ohm_elec2[l,j]  =  ((-phi_e1[l,j]+phi_e1[l+1,j])/(dx))**2 * (0.5*sigma_e[l+1,j] + 0.5* sigma_e[l,j])
            Q_ohm_elec2[0,j]= Q_ohm_elec2[1,j]
            factor_thermalconductivity[l,j]= k[l,j] *dy/dx + k[l,j] *dx/dy + 0.5 *( k[l+1,j] + k[l-1,j]) *dy/dx + 0.5 *( k[l,j+1] + k[l,j-1]) *dx/dy


                    # energy conservation
            Tn1[l,j] = (Tn[l+1,j] * dy/dx * 0.5* (k[l+1,j] + k[l,j]) + Tn[l-1,j] * dy/dx * 0.5 *(k[l-1,j] + k[l,j]) + Tn[l,j+1] * dx/dy * 0.5 *(k[l,j+1] + k[l,j]) + Tn[l,j-1] * dx/dy * 0.5* (k[l,j-1] + k[l,j]) + (Q_ohm_elec2[l,j])*dx*dy)/factor_thermalconductivity[l,j]


        # Catalyst anode layer left
        for l in range(int(n_GDP),       int(n_GDP+n_CL)):


            # source terms
            Q_ohm_ion2[l,j]  = ((-phi_m1[l+1,j]+phi_m1[l,j])/(dx))**2 * (0.5*sigma_m[l,j] + 0.5* sigma_m[l+1,j])
            Q_ohm_elec2[l,j]  =  ((-phi_e1[l,j]+phi_e1[l+1,j])/(dx))**2 * (0.5*sigma_e[l+1,j] + 0.5* sigma_e[l,j])
            Q_anode_irr[l,j] = eta_a[l,j] * Ja[l,j]
            Q_anode_rev[l,j] = Ja[l,j] * (E_th_calc_anode[i,j] - (E_tn_calc_anode[i,j]))

            factor_thermalconductivity[l,j]= k[l,j] *dy/dx + k[l,j] *dx/dy + 0.5 *( k[l+1,j] + k[l-1,j]) *dy/dx + 0.5 *( k[l,j+1] + k[l,j-1]) *dx/dy


            # energy conservation
            Tn1[l,j] = (Tn[l+1,j] * dy/dx * 0.5* (k[l+1,j] + k[l,j]) + Tn[l-1,j] * dy/dx * 0.5 *(k[l-1,j] + k[l,j]) + Tn[l,j+1] * dx/dy * 0.5 *(k[l,j+1] + k[l,j]) + Tn[l,j-1] * dx/dy * 0.5* (k[l,j-1] + k[l,j]) + (Q_ohm_ion2[l,j]+Q_anode_rev[l,j]+Q_anode_irr[l,j]+Q_ohm_elec2[l,j])*dx*dy)/factor_thermalconductivity[l,j]
```

```
46
47
48
49          # Electrolyte left
50          for l in range(int(n_GDP+n_CL),int(n_GDP+n_CL+n_el)):
51
52               # source terms
53              Q_ohm_ion2[l,j]  = ((-phi_m1[l+1,j]+phi_m1[l,j])/(dx))**2 * (0.5*sigma_m[l,j] +
    0.5* sigma_m[l+1,j])
54
55              factor_thermalconductivity[l,j]= 2*rho_w*cp*dx*velocity_left[l,j]+k[l,j] *dy/dx +
     k[l,j] *dx/dy + 0.5 *( k[l+1,j] + k[l-1,j]) *dy/dx + 0.5 *( k[l,j+1] + k[l,j-1]) *dx/dy
56
57              factor_thermalconductivity[l,0]= 2*rho_w*cp*dx*velocity_left[l,j]+k[l,0] *dy/dx +
     k[l,0] *dx/dy + 0.5 *( k[l+1,0] + k[l-1,0]) *dy/dx + 0.5 *( k[l,1] + k[l,0]) *dx/dy
58
59              Tn[l,0]= (Tn[l+1,0] * dy/dx * 0.5* (k[l+1,0] + k[l,0]) + Tn[l-1,0] * dy/dx * 0.5
    *(k[l-1,j] + k[l,j]) + Tn[l,1] * dx/dy * 0.5 *(k[l,1] + k[l,0]) + T_flow * dx/dy * 0.5* (
    k[l,0] + k[l,0]) + (Q_ohm_ion2[l,0])*dx*dy+ T_flow*(rho_w*dx*cp*velocity_left[l,j])+ Tn[l
    ,1]*(rho_w*dx*cp*velocity_left[l,0])) /factor_thermalconductivity[l,0]
60
61
62              # energy conservation
63              Tn1[l,j] = (Tn[l+1,j] * dy/dx * 0.5* (k[l+1,j] + k[l,j]) + Tn[l-1,j] * dy/dx *
    0.5 *(k[l-1,j] + k[l,j]) + Tn[l,j+1] * dx/dy * 0.5 *(k[l,j+1] + k[l,j]) + Tn[l,j-1] * dx/
    dy * 0.5* (k[l,j-1] + k[l,j]) + (Q_ohm_ion2[l,j])*dx*dy+ Tn[l,j-1]*(rho_w*dx*cp*
    velocity_left[l,j]) +  Tn[l,j+1]*(rho_w*dx*cp*velocity_left[l,j]) )/
    factor_thermalconductivity[l,j]
64
65
66
67          # PEM
68          for l in range(int(n_GDP+n_CL+n_el),int(n_GDP+n_CL+n_PEM+n_el)):
69
70
71              # source terms
72              Q_ohm_ion2[l,j]  = ((-phi_m1[l+1,j]+phi_m1[l,j])/(dx))**2 * (0.5*sigma_m[l,j] +
    0.5* sigma_m[l+1,j])
73
74
75              factor_thermalconductivity[l,j]= k[l,j] *dy/dx + k[l,j] *dx/dy + 0.5 *( k[l+1,j]
    + k[l-1,j]) *dy/dx + 0.5 *( k[l,j+1] + k[l,j-1]) *dx/dy
76
77
78              # energy conservation
79              Tn1[l,j] = (Tn[l+1,j] * dy/dx * 0.5* (k[l+1,j] + k[l,j]) + Tn[l-1,j] * dy/dx *
    0.5 *(k[l-1,j] + k[l,j]) + Tn[l,j+1] * dx/dy * 0.5 *(k[l,j+1] + k[l,j]) + Tn[l,j-1] * dx/
    dy * 0.5* (k[l,j-1] + k[l,j]) + (Q_ohm_ion2[l,j])*dx*dy)/factor_thermalconductivity[l,j]
80
81
82
83
84
85          # Electrolyte right
86          for l in range(int(n_GDP+n_CL+n_el+n_PEM),int(n_GDP+n_CL+n_PEM+2*n_el)):
87
88
89              # source terms
90              Q_ohm_ion2[:,0]=Q_ohm_ion2[:,1]
91
92              Q_ohm_ion2[l,j]  = ((-phi_m1[l+1,j]+phi_m1[l,j])/(dx))**2 * (0.5*sigma_m[l,j] +
    0.5* sigma_m[l+1,j])
93
94
95              factor_thermalconductivity[l,j]= 2*rho_w*cp*dx*velocity_right[l,j]+k[l,j] *dy/dx
    + k[l,j] *dx/dy + 0.5 *( k[l+1,j] + k[l-1,j]) *dy/dx + 0.5 *( k[l,j+1] + k[l,j-1]) *dx/dy
96
97              factor_thermalconductivity[l,0]= 2*rho_w*cp*dx*velocity_right[l,j]+k[l,0] *dy/dx
    + k[l,0] *dx/dy + 0.5 *( k[l+1,0] + k[l-1,0]) *dy/dx + 0.5 *( k[l,1] + k[l,0]) *dx/dy
98
```

```
99          Tn[l,0]= (Tn[l+1,0] * dy/dx * 0.5* (k[l+1,0] + k[l,0]) + Tn[l-1,0] * dy/dx * 0.5
    *(k[l-1,j] + k[l,j]) + Tn[l,1] * dx/dy * 0.5 *(k[l,1] + k[l,0]) + T_flow * dx/dy * 0.5* (
    k[l,0] + k[l,0]) + (Q_ohm_ion2[l,0])*dx*dy+ T_flow*(rho_w*dx*cp*velocity_right[l,j])+ Tn[
    l,1]*(rho_w*dx*cp*velocity_right[l,0])) /factor_thermalconductivity[l,0]
100
101
102         # energy conservation
103         Tn1[l,j] = (Tn[l+1,j] * dy/dx * 0.5* (k[l+1,j] + k[l,j]) + Tn[l-1,j] * dy/dx *
    0.5 *(k[l-1,j] + k[l,j]) + Tn[l,j+1] * dx/dy * 0.5 *(k[l,j+1] + k[l,j]) + Tn[l,j-1] * dx/
    dy * 0.5* (k[l,j-1] + k[l,j]) + (Q_ohm_ion2[l,j])*dx*dy+ Tn[l,j-1]*(rho_w*dx*cp*
    velocity_right[l,j])+ Tn[l,j+1]*(rho_w*dx*cp*velocity_right[l,j])) /
    factor_thermalconductivity[l,j]
104
105
106     # Catalyst cathode layer right
107     for l in range(int(n_GDP+n_CL+n_PEM+2*n_el),int(n_GDP+n_CL+n_PEM+n_CL+2*n_el) ):
108
109
110         # source terms
111         Q_ohm_ion2[l,j]  = ((-phi_m1[l,j]+phi_m1[l+1,j])/(dx))**2 * (0.5*sigma_m[l+1,j] +
     0.5* sigma_m[l,j])
112         Q_ohm_elec2[l,j]  =  ((-phi_e1[l,j]+phi_e1[l+1,j])/(dx))**2 * (0.5*sigma_e[l+1,j]
     + 0.5* sigma_e[l,j])
113         Q_cathode_irr[l,j]   = -eta_c[l,j] * Jc[l,j]
114         Q_cathode_rev[l,j]   = -Jc[l,j] * (E_th_calc_cathode[i,j] - (-E_tn_calc_cathode[i
    ,j]))
115
116         factor_thermalconductivity[l,j]= k[l,j] *dy/dx + k[l,j] *dx/dy + 0.5 *( k[l+1,j]
    + k[l-1,j]) *dy/dx + 0.5 *( k[l,j+1] + k[l,j-1]) *dx/dy
117
118         convergence_thermal[l,j]= Tn1[l,j] - ((Tn[l+1,j] * dy/dx * 0.5* (k[l+1,j] + k[l,j
    ]) + Tn[l-1,j] * dy/dx * 0.5 *(k[l-1,j] + k[l,j]) + Tn[l,j+1] * dx/dy * 0.5 *(k[l,j+1] +
    k[l,j]) + Tn[l,j-1] * dx/dy * 0.5* (k[l,j-1] + k[l,j]) + (Q_cathode_rev[l,j]+Q_ohm_ion2[l
    ,j]+Q_cathode_irr[l,j]+Q_ohm_elec2[l,j])*dx*dy)/factor_thermalconductivity[l,j] )
119
120         # energy conservation
121         convergence_thermal[l,j]= Tn1[l,j] - ((Tn[l+1,j] * dy/dx * 0.5* (k[l+1,j] + k[l,j
    ]) + Tn[l-1,j] * dy/dx * 0.5 *(k[l-1,j] + k[l,j]) + Tn[l,j+1] * dx/dy * 0.5 *(k[l,j+1] +
    k[l,j]) + Tn[l,j-1] * dx/dy * 0.5* (k[l,j-1] + k[l,j]) + (Q_cathode_rev[l,j]+Q_ohm_ion2[l
    ,j]+Q_cathode_irr[l,j]+Q_ohm_elec2[l,j])*dx*dy)/factor_thermalconductivity[l,j] )
122         Tn1[l,j] = (Tn[l+1,j] * dy/dx * 0.5* (k[l+1,j] + k[l,j]) + Tn[l-1,j] * dy/dx *
    0.5 *(k[l-1,j] + k[l,j]) + Tn[l,j+1] * dx/dy * 0.5 *(k[l,j+1] + k[l,j]) + Tn[l,j-1] * dx/
    dy * 0.5* (k[l,j-1] + k[l,j]) + (Q_cathode_rev[l,j]+Q_ohm_ion2[l,j]+Q_cathode_irr[l,j]+
    Q_ohm_elec2[l,j])*dx*dy)/factor_thermalconductivity[l,j]
123
124
125
126     # Gas diffusion plate right
127     for l in range(int(n_GDP+n_CL+n_PEM+n_CL+2*n_el),int(n_GDP+n_CL+n_PEM+n_CL+n_GDP+1+2*
    n_el)-1 ):
128
129
130         # source terms
131         Q_ohm_elec2[l,j]  = ((-phi_e1[l,j]+phi_e1[l+1,j])/(dx))**2 * (0.5*sigma_e[l+1,j]
    + 0.5* sigma_e[l,j])
132         Q_ohm_elec2[-1,j]= Q_ohm_elec2[-2,j]
133
134         factor_thermalconductivity[l,j]= k[l,j] *dy/dx + k[l,j] *dx/dy + 0.5 *( k[l+1,j]
    + k[l-1,j]) *dy/dx + 0.5 *( k[l,j+1] + k[l,j-1]) *dx/dy
135
136
137         # energy conservation
138         Tn1[l,j] = (Tn[l+1,j] * dy/dx * 0.5* (k[l+1,j] + k[l,j]) + Tn[l-1,j] * dy/dx *
    0.5 *(k[l-1,j] + k[l,j]) + Tn[l,j+1] * dx/dy * 0.5 *(k[l,j+1] + k[l,j]) + Tn[l,j-1] * dx/
    dy * 0.5* (k[l,j-1] + k[l,j]) + (Q_ohm_elec2[l,j])*dx*dy)/factor_thermalconductivity[l,j]
139
140
141
142         Tn1[int(npts-1),j] = ((T_flow * dy *h[0,j])/k[int(npts-1),j] + 0.5*Q_ohm_elec2[
    int(npts-1),j]*dx*dy/k[int(npts-1),j] +  Tn[int(npts-2),j] *dy/dx+ 0.5* Tn[int(npts-1),j
    -1] *dx/dy+ 0.5* Tn[int(npts-1),j+1] *dx/dy)/ (h[0,j]/k[int(npts-1),j]*dy+ dx/dy +dy/dx)
```

```
143
144     print( convergence_thermal.min())
145
146     Q_ohm_ion2[:,0]=Q_ohm_ion2[:,1]
147     Tn1[:,-1] = Tn1[:,-2]
148     Tn1[:,0]= Tn1[:,1]
149
150     #for l in range(int(n_GDP+n_CL+n_el+n_PEM),int(n_GDP+n_CL+n_PEM+2*n_el)):
151         #factor_thermalconductivity[l,0]= k[l,0] *dy/dx + k[l,0] *dx/dy + 0.5 *( k[l+1,0] + k
    [l-1,0]) *dy/dx + 0.5 *( k[l,1] + k[l,0]) *dx/dy
152
153         #Tn1[l,0]= (Tn[l,0] * dy/dx * 0.5* (k[l+1,0] + k[l,0]) + Tn[l-1,0] * dy/dx * 0.5 *(k[
    l-1,j] + k[l,j]) + Tn[l,1] * dx/dy * 0.5 *(k[l,1] + k[l,0]) + T_flow * dx/dy * 0.5* (k[l
    ,0] + k[l,0]) + (Q_ohm_ion2[l,0])*dx*dy+ T_flow*(rho_w*dx*cp*velocity_right[l,j])+ Tn[l,j
    +1]*(rho_w*dx*cp*velocity_right[l,0])) /factor_thermalconductivity[l,0]
154
155     Tn = Tn1
156
157
158
159
160
161 Gen_heat = (Q_anode_irr + Q_cathode_irr + Q_ohm_elec2 + Q_ohm_ion2+ Q_cathode_rev+Q_anode_rev
        )
162
163 convergence_all = Tn1 - old_temperature
164 old_temperature = Tn1
```

Listing B.11: The code describes the thermal model in Python.

Bibliography

[1] (2020). *Encyclopedia of Sustainability Science and Technology*. Springer New York.

[2] Abdul Rasheed, R. K., Liao, Q., Caizhi, Z., and Chan, S. H. (2017). A review on modelling of high temperature proton exchange membrane fuel cells (HT-PEMFCs).

[3] Agbli, K. S., Péra, M. C., Hissel, D., Rallires, O., Turpin, C., and Doumbia, I. (2011). Multiphysics simulation of a PEM electrolyser: Energetic Macroscopic Representation approach. *International Journal of Hydrogen Energy*, 36(2):1382–1398.

[4] Ahadi, M., Tam, M., Saha, M. S., Stumper, J., and Bahrami, M. (2017). Thermal conductivity of catalyst layer of polymer electrolyte membrane fuel cells: Part 1–experimental study. *Journal of Power Sources*, 354:207–214.

[5] Al-Baghdadi, M. A. and Al-Janabi, H. A. (2007). Numerical analysis of a proton exchange membrane fuel cell. Part 1: Model development. *Proceedings of the Institution of Mechanical Engineers, Part A: Journal of Power and Energy*, 221(7):917–929.

[6] Allebrod, F., Chatzichristodoulou, C., Mollerup, P. L., and Mogensen, M. B. (2012). Electrical conductivity measurements of aqueous and immobilized potassium hydroxide. *International Journal of Hydrogen Energy*, 37(21):16505–16514.

[7] Aydin, Gokhan & Karakurt, I. . A. K. (2010). Evaluation of geologic storage options of CO_2: Applicability, cost, storage capacity and safety. *Elsevier*.

[8] Bard, A. J. and Faulkner, L. R. (1983). Electrochemical methods fundamentals and applications. *Surface Technology*, 20(1):91–92.

[9] Barrett, T. and House, G. M. (2014). Re: ICCT responses to “advanced fuels: call for evidence”.

[10] Bauer, F., Denneler, S., and Willert-Porada, M. (2005). Influence of temperature and humidity on the mechanical properties of nafion® 117 polymer electrolyte membrane. *Journal of Polymer Science Part B: Polymer Physics*, 43(7):786–795.

[11] Bespalko, S., Halychyi, O., Roha, M., Poliakov, S., Kaleinikov, G., and Naumenko, T. (2019). Experimental study of the thermal effect of the dissolution reaction for some alkalis and salts with natural mixing and forced stirring. In *E3S Web of Conferences*, volume 118, page 01026. EDP Sciences.

[12] Bhargava, S. S., Proietto, F., Azmoodeh, D., Cofell, E. R., Henckel, D. A., Verma, S., Brooks, C. J., Gewirth, A. A., and Kenis, P. J. (2020). System Design Rules for Intensifying the Electrochemical Reduction of CO2 to CO on Ag Nanoparticles. *ChemElectroChem*, 7(9):2001–2011.

[13] Bird, R. B. (2002). Transport phenomena. *Appl. Mech. Rev.*, 55(1):R1–R4.

[14] Bock, R., Karoliussen, H., Seland, F., Pollet, B. G., Thomassen, M. S., Holdcroft, S., and Burheim, O. S. (2020). Measuring the thermal conductivity of membrane and porous transport layer in proton and anion exchange membrane water electrolyzers for temperature distribution modeling. *international journal of hydrogen energy*, 45(2):1236–1254.

[15] Burheim, O. S., Su, H., Hauge, H. H., Pasupathi, S., and Pollet, B. G. (2014). Study of thermal conductivity of PEM fuel cell catalyst layers. *International Journal of Hydrogen Energy*, 39(17):9397–9408.

[16] Busquet, S., Hubert, C. E., Labbé, J., Mayer, D., and Metkemeijer, R. (2004). A new approach to empirical electrical modelling of a fuel cell, an electrolyser or a regenerative fuel cell. *Journal of Power Sources*, 134(1):41–48.

[17] Cetinbas, C. F. (2014). MODELING AND OPTIMIZATION OF THE PEM FUEL CELL CATALYST LAYER. Technical report.

[18] Cheddie, D. and Munroe, N. (2005). Review and comparison of approaches to proton exchange membrane fuel cell modeling. *Journal of Power Sources*, 147(1-2):72–84.

[19] Chen, C., Kotyk, J. F. K., and Sheehan, S. W. (2018). Progress toward commercial application of electrochemical carbon dioxide reduction. *Chem*, 4(11):2571–2586.

[20] Core Writing Team of IPCC (2015). Climate change 2014, synthesis report. *INTERGOVERNMENTAL PANEL ON climate change*.

[21] Cretti, D. A. (2020). 2D Numerical Modelling of the Heat Development in a CO_2 Electrolyser.

[22] Cumming, D. J. and Elder, R. H. (2015). Thermal imaging of solid oxide cells operating under electrolysis conditions. *Journal of Power Sources*, 280:387–392.

[23] Diéguez, P. M., Ursúa, A., Sanchis, P., Sopena, C., Guelbenzu, E., and Gandía, L. M. (2008). Thermal performance of a commercial alkaline water electrolyzer: Experimental study and mathematical modeling. *International Journal of Hydrogen Energy*, 33(24):7338–7354.

[24] Dincer, I. (2018). *Comprehensive energy systems*. Elsevier.

[25] Dioxide Materials (2021). Co2 electrolyzers. https://dioxidematerials.com/technology/co2-electrolysis.

[26] Durst, J., Rudnev, A., Dutta, A., Fu, Y., Herranz, J., Kaliginedi, V., Kuzume, A., Permyakova, A. A., Paratcha, Y., Broekmann, P., and Schmidt, T. J. (2015). Electrochemical CO2 reduction -A critical view on fundamentals, materials and applications. *Chimia*, 69(12):769–776.

[27] European Commission (2021). 2030 climate & energy framework. https://ec.europa.eu/clima/policies/strategies/2030_en.

[28] Falcão, D. S. and Pinto, A. M. (2020). A review on PEM electrolyzer modelling: Guidelines for beginners.

[29] Fan, L., Xia, C., Yang, F., Wang, J., Wang, H., and Lu, Y. (2020). Strategies in catalysts and electrolyzer design for electrochemical co2 reduction toward c2+ products. *Science advances*, 6(8):eaay3111.

[30] Feng, L., Sun, X., Yao, S., Liu, C., Xing, W., and Zhang, J. (2014). Electrocatalysts and catalyst layers for oxygen reduction reaction. In *Rotating electrode methods and oxygen reduction electrocatalysts*, pages 67–132. Elsevier.

[31] Fuller, T. F. and Harb, J. N. (2018). *Electrochemical engineering*. John Wiley & Sons.

[32] Gao, D., Wei, P., Li, H., Lin, L., Wang, G., and Bao, X. (2021). Designing electrolyzers for electrocatalytic co2 reduction. *ACTA PHYSICO-CHIMICA SINICA*, 37:2009021.

[33] García-Valverde, R., Espinosa, N., and Urbina, A. (2012). Simple PEM water electrolyser model and experimental validation. In *International Journal of Hydrogen Energy*, volume 37, pages 1927–1938.

[34] Garg, S., Li, M., Weber, A. Z., Ge, L., Li, L., Rudolph, V., Wang, G., and Rufford, T. E. (2020). Advances and challenges in electrochemical CO2 reduction processes: An engineering and design perspective looking beyond new catalyst materials.

[35] Ghassemi, M., Kamvar, M., and Steinberger-Wilckens, R. (2020). Fundamental of heat transfer. In *Fundamentals of Heat and Fluid Flow in High Temperature Fuel Cells*, pages 101–124. Elsevier.

[36] Gilliam, R., Graydon, J., Kirk, D., and Thorpe, S. (2007). A review of specific conductivities of potassium hydroxide solutions for various concentrations and temperatures. *International Journal of Hydrogen Energy*, 32(3):359–364.

[37] Goodridge, F. and Scott, K. (2013). *Electrochemical process engineering: a guide to the design of electrolytic plant*. Springer Science & Business Media.

[38] Hammoudi, M., Henao, C., Agbossou, K., Dubé, Y., and Doumbia, M. L. (2012). New multi-physics approach for modelling and design of alkaline electrolyzers. *International Journal of Hydrogen Energy*, 37(19):13895–13913.

[39] Han, B., Steen, S. M., Mo, J., and Zhang, F. Y. (2015). Electrochemical performance modeling of a proton exchange membrane electrolyzer cell for hydrogen energy. *International Journal of Hydrogen Energy*, 40(22):7006–7016.

[40] Haverkort, W. and Kortlever, R. (2021). Lecture notes in electrical energy storage 2.

[41] Herrington, T. M., Pethybridge, A. D., and Roffey, M. G. (1986). Densities of aqueous lithium, sodium and potassium hydroxides from 25 to 75. degree. c at 1 atm. *Journal of Chemical and Engineering Data*, 31(1):31–34.

[42] Hołyst, R. and Poniewierski, A. (2012). *Thermodynamics for chemists, physicists and engineers*. Springer Science & Business Media.

[43] Hori, Y., Ito, H., Okano, K., Nagasu, K., and Sato, S. (2003). Silver-coated ion exchange membrane electrode applied to electrochemical reduction of carbon dioxide. *Electrochimica Acta*, 48(18):2651–2657.

[44] Kaczur, J. J., Yang, H., Liu, Z., Sajjad, S. D., and Masel, R. I. (2018). Carbon dioxide and water electrolysis using new alkaline stable anion membranes. *Frontiers in Chemistry*, 6(JUL).

[45] Kahan, A. (2019). Eia projects nearly 50by growth in asia. https://www.eia.gov/todayinenergy/detail.php?id=41433.

[46] Kas, R., Yang, K., Bohra, D., Kortlever, R., Burdyny, T., and Smith, W. A. (2020). Electrochemical co2 reduction on nanostructured metal electrodes: Fact or defect? *Chemical Science*, 11(7):1738–1749.

[47] Kauppi P, Sedjo RJ, A. M. C. C. F. T. (2001). Technical and economic potential of options to enhance, maintain and manage biological carbon reservoirs and geoengineering. *Mitigation 2001: the IPCC third assessment report*.

[48] Khalid, F., Dincer, I., and Rosen, M. A. (2018). Model development and analysis of a novel high-temperature electrolyser for gas phase electrolysis of hydrogen chloride for hydrogen production. *International Journal of Hydrogen Energy*, 43(19):9112–9118.

[49] Kibria, M. G., Edwards, J. P., Gabardo, C. M., Dinh, C. T., Seifitokaldani, A., Sinton, D., and Sargent, E. H. (2019). Electrochemical CO2 Reduction into Chemical Feedstocks: From Mechanistic Electrocatalysis Models to System Design.

[50] Kim, H., Park, M., and Lee, K. S. (2013). One-dimensional dynamic modeling of a high-pressure water electrolysis system for hydrogen production. *International Journal of Hydrogen Energy*, 38(6):2596–2609.

[51] Kortlever, R. (2021). Lecture 5, electrocatalysis. University Lecture of Electrochemical Energy Storage 1: Fundamentals.

[52] Kuhl, K. P., Cave, E. R., Abram, D. N., and Jaramillo, T. F. (2012). New insights into the electrochemical reduction of carbon dioxide on metallic copper surfaces. *Energy & Environmental Science*, 5(5):7050–7059.

[53] Küngas, R. (2020). Review—Electrochemical CO 2 Reduction for CO Production: Comparison of Low- and High-Temperature Electrolysis Technologies . *Journal of The Electrochemical Society*, 167(4):044508.

[54] Kutz, R. B., Chen, Q., Yang, H., Sajjad, S. D., Liu, Z., and Masel, I. R. (2017). Sustainion Imidazolium-Functionalized Polymers for Carbon Dioxide Electrolysis. *Energy Technology*, 5(6):929–936.

[55] Lebbal, M. E. and Lecœuche, S. (2009). Identification and monitoring of a PEM electrolyser based on dynamical modelling. *International Journal of Hydrogen Energy*, 34(14):5992–5999.

[56] Lee, J., Lim, J., Roh, C. W., Whang, H. S., and Lee, H. (2019). Electrochemical CO2 reduction using alkaline membrane electrode assembly on various metal electrodes. *Journal of CO2 Utilization*, 31:244–250.

[57] Liam J. France1, Peter P. Edwards1, V. L. K. H. A. (2014). *Carbon Dioxide Utilisation: Closing the Carbon Cycle*, volume Chapter 10. Elsevier.

[58] Linstrom, P. J. and Mallard, W. G. (2001). The nist chemistry webbook: A chemical data resource on the internet. *Journal of Chemical & Engineering Data*, 46(5):1059–1063.

[59] Liu, Z., Yang, H., Kutz, R., and Masel, R. I. (2018). CO 2 Electrolysis to CO and O 2 at High Selectivity, Stability and Efficiency Using Sustainion Membranes . *Journal of The Electrochemical Society*, 165(15):J3371–J3377.

[60] Löwe, A., Rieg, C., Hierlemann, T., Salas, N., Kopljar, D., Wagner, N., and Klemm, E. (2019). Influence of Temperature on the Performance of Gas Diffusion Electrodes in the CO2 Reduction Reaction. *ChemElectroChem*, 6(17):4497–4506.

[61] Marangio, F., Santarelli, M., and Calì, M. (2009). Theoretical model and experimental analysis of a high pressure PEM water electrolyser for hydrogen production. *International Journal of Hydrogen Energy*, 34(3):1143–1158.

[62] McCrory, C. C., Jung, S., Peters, J. C., and Jaramillo, T. F. (2013). Benchmarking heterogeneous electrocatalysts for the oxygen evolution reaction. *Journal of the American Chemical Society*, 135(45):16977–16987.

[63] Meng, H. and Wang, C. Y. (2005). Multidimensional modelling of polymer electrolyte fuel cells under a current density boundary condition. *Fuel Cells*, 5(4):455–462.

[64] Mills, A. F. (2014). *Basic heat and mass transfer*. Pearson Education Limited.

[65] Nandjou, F., Poirot-Crouvezier, J.-P., Chandesris, M., Blachot, J.-F., Bonnaud, C., and Bultel, Y. (2015). Correlation between local temperature and degradations in polymer electrolyte membrane fuel cells. *ECS Transactions*, 66(25):1.

[66] Ni, M. (2010). Modeling of a solid oxide electrolysis cell for carbon dioxide electrolysis. *Chemical Engineering Journal*, 164(1):246–254.

[67] Ni, M. (2012). 2D thermal modeling of a solid oxide electrolyzer cell (SOEC) for syngas production by H2O/CO2 co-electrolysis. *International Journal of Hydrogen Energy*, 37(8):6389–6399.

[68] Ni, M., Leung, M. K., and Leung, D. Y. (2006). A modeling study on concentration overpotentials of a reversible solid oxide fuel cell. *Journal of Power Sources*, 163(1 SPEC. ISS.):460–466.

[69] Niklas V. von der Assen, Ana Maria Lorente Lafuente, M. P. A. □. B. (2014). *Carbon Dioxide Utilisation: Closing the Carbon Cycle*, volume Chapter 4. Elsevier.

[70] North, M. (2014). *Carbon Dioxide Utilisation: Closing the Carbon Cycle*. Elsevier.

[71] Olesen, A. C., Frensch, S. H., and Kær, S. K. (2019). Towards uniformly distributed heat, mass and charge: A flow field design study for high pressure and high current density operation of PEM electrolysis cells. *Electrochimica Acta*, 293:476–495.

[72] Olivier, P., Bourasseau, C., and Bouamama, P. B. (2017). Low-temperature electrolysis system modelling: A review.

[73] Onda, K., Murakami, T., Hikosaka, T., Kobayashi, M., Notu, R., and Ito, K. (2002). Performance Analysis of Polymer-Electrolyte Water Electrolysis Cell at a Small-Unit Test Cell and Performance Prediction of Large Stacked Cell. *Journal of The Electrochemical Society*, 149(8):A1069.

[74] Peeters, J. (2020). Lecture notes in advanced heat transfer.

[75] Peter J. Hall, I.A. Grant Wilson, A. R. (2014). *Carbon Dioxide Utilisation: Closing the Carbon Cycle*, volume Chapter 3. Elsevier.

[76] Pierre Oliviera, Cyril Bourasseaua, P. B. B. (2017). Low-temperature electrolysis system modelling: A review. *Renewable and Sustainable Energy Reviews*, 78.

[77] Price, A. (2015). *Electrochemical Energy Storage for Renewable Sources and Grid Balancing*, volume Chapter 1: The Exploitation of Renewable Sources of Energy for Power Generation. Elsevier.

[78] Qiao, J., Liu, Y., and Zhang, J. (2016). *Electrochemical reduction of carbon dioxide: fundamentals and technologies*. CRC Press.

[79] Scheepers, F., Stähler, M., Stähler, A., Rauls, E., Müller, M., Carmo, M., and Lehnert, W. (2020). Temperature optimization for improving polymer electrolyte membrane-water electrolysis system efficiency. *Applied Energy*.

[80] Secanell, M., Putz, A., Wardlaw, P., Zingan, V., Bhaiya, M., Moore, M., Zhou, J., Balen, C., and Domican, K. (2014). OpenFCST: An Open-Source Mathematical Modelling Software for Polymer Electrolyte Fuel Cells. *ECS Transactions*, 64(3):655–680.

[81] Siegel, C. (2008). Review of computational heat and mass transfer modeling in polymer-electrolyte-membrane (PEM) fuel cells.

[82] Suter, S. and Haussener, S. (2019). Optimizing mesostructured silver catalysts for selective carbon dioxide conversion into fuels. *Energy & Environmental Science*, 12(5):1668–1678.

[83] Tomazic, G. and Skyllas-Kazacos, M. (2015). *Electrochemical Energy Storage for Renewable Sources and Grid Balancing*, volume Chapter 17: Redox Flow Batteries. Elsevier.

[84] United Nations (2019). Population. https://www.un.org/en/sections/issues-depth/population/.

[85] Vennekoetter, J. B., Sengpiel, R., and Wessling, M. (2019). Beyond the catalyst: How electrode and reactor design determine the product spectrum during electrochemical CO2 reduction. *Chemical Engineering Journal*, 364:89–101.

[86] Verma, S., Lu, X., Ma, S., Masel, R. I., and Kenis, P. J. (2016). The effect of electrolyte composition on the electroreduction of CO2 to CO on Ag based gas diffusion electrodes. *Physical Chemistry Chemical Physics*, 18(10):7075–7084.

[87] Wang, C. Y. (2004). Fundamental models for fuel cell engineering. *Chemical Reviews*, 104(10):4727–4765.

[88] Wang, G., Mukherjee, P. P., and Wang, C. Y. (2006). Direct numerical simulation (DNS) modeling of PEFC electrodes: Part II. Random microstructure. *Electrochimica Acta*, 51(15):3151–3160.

[89] Wang, P. and Anderko, A. (2008). Modeling thermal conductivity of concentrated and mixed-solvent electrolyte systems. *Industrial & engineering chemistry research*, 47(15):5698–5709.

[90] Wang, Q., Tang, F., Li, B., Dai, H., Zheng, J. P., Zhang, C., and Ming, P. (2021). Numerical analysis of static and dynamic heat transfer behaviors inside proton exchange membrane fuel cell. *Journal of Power Sources*, 488:229419.

[91] Wang, W., Wei, X., Choi, D., Lu, X., Yang, G., and Sun, C. (2015). Electrochemical cells for medium-and large-scale energy storage: Fundamentals. In *Advances in Batteries for Medium and Large-Scale Energy Storage: Types and Applications*, pages 3–28. Elsevier.

[92] Weng, L. C., Bell, A. T., and Weber, A. Z. (2019). Towards membrane-electrode assembly systems for CO2 reduction: A modeling study. *Energy and Environmental Science*, 12(6):1950–1968.

[93] Wu, H. W. (2016). A review of recent development: Transport and performance modeling of PEM fuel cells.

[94] Xie, J., Huang, Y., Wu, M., and Wang, Y. (2019). Electrochemical Carbon Dioxide Splitting.

[95] Xu, H., Chen, B., Irvine, J., and Ni, M. (2016). Modeling of CH4-assisted SOEC for H2O/CO2 co-electrolysis. *International Journal of Hydrogen Energy*, 41(47):21839–21849.

[96] Zhang, X., Song, Y., Wang, G., and Bao, X. (2017). Co-electrolysis of CO2 and H2O in high-temperature solid oxide electrolysis cells: Recent advance in cathodes.

[97] Zhang, Z. and Xing, X. (2020). Simulation and experiment of heat and mass transfer in a proton exchange membrane electrolysis cell. *International Journal of Hydrogen Energy*, 45(39):20184–20193.

[98] Zhao, D., He, Q., Yu, J., Jiang, J., Li, X., and Ni, M. (2020). Dynamic behaviour and control strategy of high temperature proton exchange membrane electrolyzer cells (HT-PEMECs) for hydrogen production. *International Journal of Hydrogen Energy*, 45(51):26613–26622.